2012

Plasmonic devices for manipulating light at the nanoscale: slow-light waveguides and compact couplers

Yin Huang
Louisiana State University and Agricultural and Mechanical College

PLASMONIC DEVICES FOR MANIPULATING LIGHT AT THE NANOSCALE: SLOW-LIGHT WAVEGUIDES AND COMPACT COUPLERS

A Dissertation

Submitted to the Graduate Faculty of the
Louisiana State University and
Agricultural and Mechanical College
in partial fulfillment of the
requirements for the degree of
Doctor of Philosophy

in

The Division of Electrical and Computer Engineering

by
Yin Huang
B.S., North China University of Technology, 2007
M.S., Beijing Jiaotong University, 2009
December 2012

Dedicated to my parents

Acknowledgments

The completion of this dissertation would not have been possible without the help of many people. I would like to thank my advisor Dr. Georgios Veronis, first for giving me the opportunity to come to LSU. I also deeply appreciate his respect and trust in me as well as his guidance, patience, and understanding that made this research possible. I appreciate his dedication and encouragement towards completion of this work.

I would also like to thank Dr. Changjun Min who helped me decisively during my first two years at LSU. I really appreciate the fact that he was always available to discuss my research and provide invaluable suggestions and comments.

I would like to thank Professors Elizabeth Dan-Cohen, Theda Daniels-Race, Jonathan P. Dowling, Hwang Lee, and Kenneth A. Rose for being members of my general and final examination committees.

I am grateful to other members of our research group for their friendship and help: Christopher Granier, Pouya Dastmalchi, and Ali Haddadpour. I would also like to thank Beth Cochran for her valuable everyday help with administrative work.

This dissertation is dedicated to my parents. Without their marvelous support and unconditional love, none of my achievements would have been possible.

Table of Contents

Abstract

In this dissertation, I explore new plasmonic structures and devices for manipulating light at the nanoscale: slow-light waveguides and compact couplers. I first introduce a plasmonic waveguide system, based on a plasmonic analogue of electromagnetically induced transparency (EIT), which supports a subwavelength slow-light mode, and exhibits a small group velocity dispersion. The system consists of a periodic array of two metal-dielectric-metal (MDM) stub resonators side-coupled to a MDM waveguide. Decreasing the frequency spacing between the two resonances increases the slowdown factor and decreases the bandwidth of the slow-light band. I also show that there is a trade-off between the slowdown factor and the propagation length of the slow-light mode.

I next consider Mach-Zehnder interferometer (MZI) sensors in which the sensing arm consists of a slow-light waveguide based on a plasmonic analogue of EIT. I show that a MZI sensor using such a waveguide leads to approximately an order of magnitude enhancement in the refractive index sensitivity, and therefore in the minimum detectable refractive index change, compared to a MZI sensor using a conventional MDM waveguide.

I also introduce compact wavelength-scale slit-based structures for coupling free space light into MDM subwavelength plasmonic waveguides. I first show that for a single slit structure the coupling efficiency is limited by a trade-off between the light power coupled into the slit, and the transmission of the slit-MDM waveguide junction. I next consider a two-section slit structure, and show that for such a structure the upper slit section enhances the coupling of the incident light into the lower slit section. The optimized two-section slit structure results in ~ 2.3 times enhancement of the coupling into the MDM plasmonic waveguide compared to the

optimized single-slit structure. I finally consider a symmetric double-slit structure, and show that for such a structure the surface plasmons excited at the metal-air interfaces are partially coupled into the slits. Thus, the coupling of the incident light into the slits is greatly enhanced, and the optimized double-slit structure results in ~ 3.3 times coupling enhancement compared to the optimized single-slit structure. In all cases the coupler response is broadband.

Chapter 1
Introduction

1.1 Introduction to Plasmonics

As modern information technology develops, the ever increasing demand for faster information processing is inevitable. Since the breakthrough invention of the first transistor at Bell laboratories, the new era of silicon electronics technology emerged, and our data-hungry society continuously drives electronic devices to become smaller, faster, and more efficient. However, further increases in electronic processing speed are at present limited by delays related to electronic interconnections [1, 2]. Because of this, the integration of modern electronic devices for information processing is rapidly approaching a fundamental speed limitation.

On the other hand, it is well-known that the velocity of a photon is much faster than that of an electron in a dielectric. One of the potential research directions to address the limitations of electronic interconnects is therefore to explore using photonic devices instead of their electronic counterparts. However, conventional photonic devices cannot be integrated as densely as their electronic counterparts. In fact, this limitation of conventional dielectric optics is a consequence of the diffraction limit of light in dielectric media, which does not allow light to be confined in a region smaller than the wavelength of light. As an example, a dielectric waveguide supports electromagnetic modes. More specifically, I consider an air-silicon-air dielectric slab waveguide (Fig. 1.1). Such a waveguiding structure always supports a fundamental optical mode for any silicon core thickness. When the size of the silicon core w is $\sim 0.68\lambda_0/n$, the fundamental mode can be effectively guided in such a waveguide. In other words, the modal field is highly confined in the silicon

core. Here, λ_0 is the free-space wavelength, and n is the refractive index of silicon. As the size w decreases, the fundamental guided mode further extends into the surrounding air cladding region (Fig. 1.1). Thus, simply decreasing the size of the waveguide core does not lead to subwavelength guiding of the optical mode.

Fig. 1.1 clearly demonstrates the limitations associated with the diffraction limit of light in conventional dielectric waveguides, and reveals the daunting problem that one faces when attempting to achieve chip-scale integration of optical devices. As a result, conventional dielectric optical waveguides cannot provide fast and highly-compact interconnects. In addition, the large size mismatch between electronic and optical devices indicates that there is also no way to integrate these two technologies in the same chip. In short, the speed of electronics is limited by delays in the interconnections, whereas the dense integration of conventional dielectric optics is limited by the diffraction limit.

It therefore appears that further progress in information processing will require the development of a promising new chip-scale device technology that can combine the size of nanoscsale electronics and the speed of photonics, and thus bridge the gap between nanoscale electronics and mircoscale photonics. The most feasible way to circumvent the diffraction limit and squeeze light into nanoscale regions much smaller than the wavelength of light is to use materials with negative dielectric permittivity, such as metals. More specifically, the interface between a metal and a dielectric supports the so-called surface plasmon-polariton (SPP) modes of electromagnetic waves coupled to the collective oscillations of the electron plasma in the metal [3]. When the operating frequency approaches the surface plasmon frequency, the field profile of these modes is highly confined in a deep subwavelength region at the metal-dielectric interface. Therefore, the emerging area of plasmonics enables light at the nanosacle, and could potentially address the technological

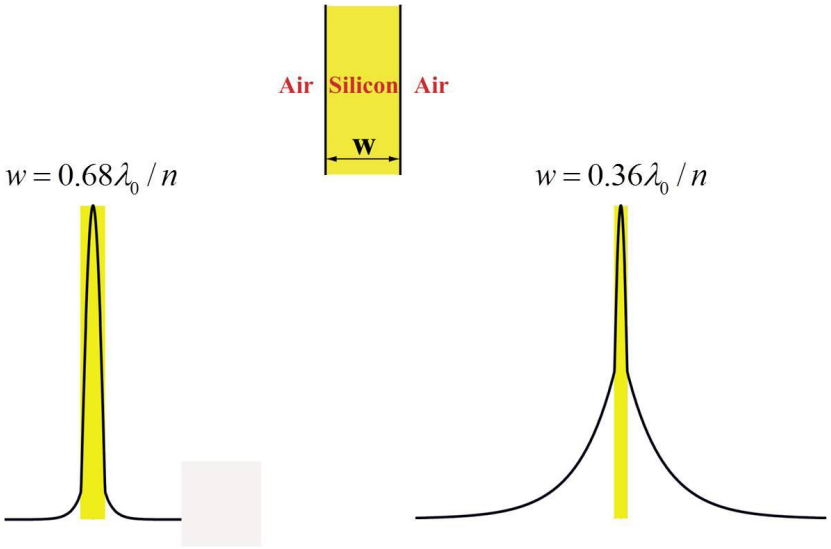

FIGURE 1.1. Schematic of an air-silicon-air dielectric slab waveguide. The field profile of the fundamental waveguide mode supported by such a structure is shown for different thicknesses of the silicon core w.

challenges described in the previous paragraph. Plasmonics could lead to ultra-fast and ultra-dense optical interconnections.

A variety of plasmonics applications has emerged in the past decade. One of the first practical applications of plasmonics is near-field scanning optical microscopy (NSOM). Subwavelength aperture structures, such as C-shape apertures, in metal-coated optical probes enable localization of light in a nanoscale spot size and are therefore useful in near-field optical microscopy [4]. An alternative method is the apertureless technique, in which a sharp metal tip is used to localize light in an intense near-field spot. The deep-subwavelength spatial resolution of such an apertureless NSOM can be as small as $\sim \lambda/3000$ at terahertz and infrared frequencies [5]. The so-called tip-on-aperture (TOA) which combines the above two techniques has attracted a lot of interest recently. The aperture's enhanced field, and the tip limited resolution of the metal structure make the TOA useful for NSOM technologies (Fig. 1.2) [6].

FIGURE 1.2. An aperture-based probe consisting of a metal protrusion deposited adjacent to an NSOM aperture.

Applications of plasmonics also include the development of metallic nanostructures for guiding SPP modes, such as nanogaps between metallic media [7], metallic nanoparticle arrays [8, 9], V-shaped grooves [10, 11], metal wedges [11, 12], and metal-dielectric-metal (MDM) waveguides [13]. Among these, MDM plasmonic waveguides are of particular interest because they support modes with deep subwavelength scale over a very wide range of frequencies extending from DC to visible [7].

As mentioned above, plasmonics offers a great opportunity to integrate electronic devices and their optical counterparts on the same chip. One of the particularly promising related applications is the plasmon-enhanced photodetector, which combines high-speed detection and low-power consumption (Fig. 1.3(a)) [14]. In addition to plasmon-enhanced photodetectors, chip-scale, high-speed, and power-efficient optical modulators enhanced by surface plasmons were also recently

realized. More specifically, the device shown in Fig. 1.3(b) enables electrical signals to be encoded into optical signals by changing the optical properties of a nonlinear optical material sandwiched between the metal plates of a MDM plasmonic waveguide [15].

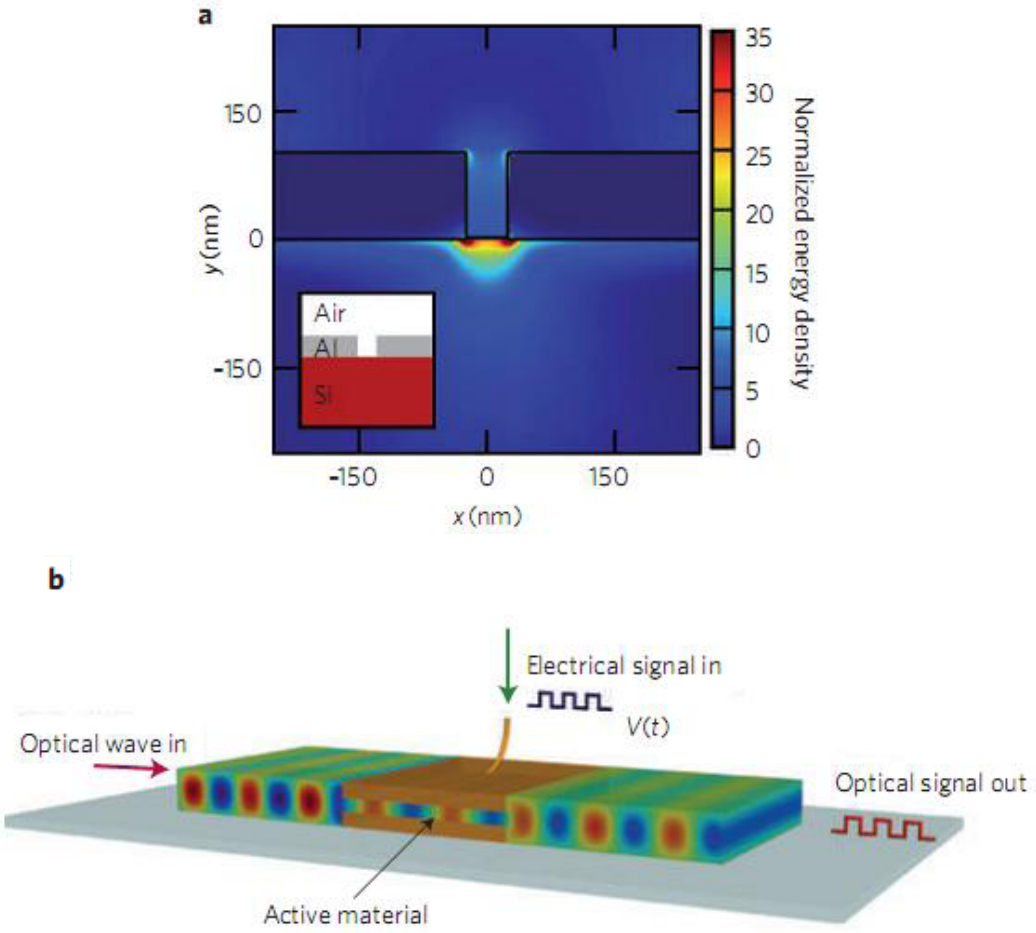

FIGURE 1.3. (a) Normalized field-energy density for a plasmon-based detector. (b) Schematic of a plasmonic modulator which enables electrical signals to be encoded into optical signals.

Plasmonics techniques can also find applications in the field of photovoltaics. Metallic nanostructures can enhance the efficiency of solar cells in converting sunlight into electrical power [16, 17]. More recently, light-induced heating using plasmonics has led to many novel applications, such as growth of semiconductor nanostructures [18], thermal cancer treatment [19], and local control over phase

transitions [20]. Since plasmonics can squeeze light into nanoscale volumes, it is natural to consider its application in nonlinear optics and biosensors. Patterned metal films can increase second-harmonic generation by more than an order of magnitude [21], while Mach-Zehnder interferometers (MZI) with SPP waveguides demonstrated high detection resolution and sensitivity [22]. In addition, plasmonics lays the foundation for further novel material science and device technologies, from metamaterials [23] to quantum plasmonics [24]. The field of plasmonics has grown dramatically over the past decade, and it will be exciting to see what plasmonics will bring for our society in the next decade.

1.2 Motivation

As described in the previous Section, the unique properties of surface plasmons, which are light waves that propagate along metal surfaces, enable a wide range of practical applications, including light guiding and manipulation at the nanoscale [25, 26, 27, 28]. This could lead to miniaturized photonic circuits with length scales that are much smaller than those currently achieved [26, 27]. The newfound ability to use metallic nanostructures to manipulate light at nanometric length scales has opened a myriad of exciting opportunities. Plasmonics is being explored for its potential in subwavelength optics, data storage, light generation, microscopy and biophotonics [25, 26, 28]. However, exploration of functional nanoplasmonic structures and devices, including active plasmonic devices, is still in a very early stage. The realization of such devices would enable for the first time controlling light and enhancing light-matter interactions at the nanoscale - beyond the diffraction limit - something which is fundamentally impossible to achieve with dielectric-based device components. This in turn would have profound implications for computing,

communications, and energy applications. The development of these nanoscale devices and their integration will be challenging. It is therefore important to theoretically and computationally explore this area and to identify the most promising structures for specific device applications such as sensing and switching.

Electromagnetically induced transparency (EIT) is a coherent process observed in three-level atomic media, which allows a narrow transparency window in the spectrum of an otherwise opaque medium, and can slow down light pulses by several orders of magnitude [29]. Since the EIT spectrum results from the interference of resonant pathways [29, 30], it has been recognized that similar interference effects can also occur in classical systems, such as optical waveguides coupled to resonators and metamaterials [29, 31, 32, 33]. In addition, it has been demonstrated that periodic optical waveguides, resulting from cascading structures with EIT-like response, can slow down and even stop light [30, 34, 35]. Inspired by these recent experimental and theoretical developments, I will investigate in detail the properties of periodic plasmonic waveguides which represent an all-optical plasmonic analogue of EIT. I will also investigate nanoscale plasmonic sensors enhanced by slow-light effects. While dielectric waveguides lead to wavelength-scale sensors, plasmonic waveguides could enable miniaturized sensors with subwavelength length scales, due to the ability of such waveguides to confine and manipulate light at the nanoscale.

In addition, for applications involving MDM plasmonic waveguides, it is essential to develop compact structures to couple light efficiently into such waveguides [36]. Several different couplers between MDM and dielectric waveguides have been investigated both theoretically and experimentally [36, 37, 38, 39, 40, 41]. In addition, structures for coupling free space radiation into MDM waveguides have also been investigated. In particular, Preiner *et al.* [42] investigated subwavelength diffraction

gratings as coupling structures into MDM waveguide modes. However, in diffraction grating structures several grating periods are required for efficient waveguide mode excitation, so that such structures need to be several microns long when designed to operate at frequencies around the optical communication wavelength (λ_0 =1.55 μm). In addition, in several experimental investigations of MDM waveguides and devices, a single slit was used to couple light from free space into MDM plasmonic waveguides [15, 43, 44, 45, 46]. While single slit coupling structures are more compact, slit-based coupler designs have not been investigated in detail. In this dissertation, I will investigate compact wavelength-scale slit-based structures for coupling free space light into MDM plasmonic waveguides.

1.3 Outline of the Dissertation

The remainder of this dissertation is organized as follows. In Chapter 2, I discuss the finite-difference frequency-domain technique, and its application in the simulation of plasmonic devices. In Chapter 3, I discuss several issues associated specifically with the simulation of plasmonic waveguide devices. In Chapter 4, I introduce novel subwavelength slow-light plasmonic waveguides based on a plasmonic analogue of EIT. In Chapter 5, I investigate MZI sensors in which the sensing arm consists of slow-light waveguides introduced in Chapter 4. In Chapter 6, I introduce compact wavelength-scale slit-based structures for coupling free space light into MDM subwavelength plasmonic waveguides. Finally, in Chapter 7, I summarize my conclusions, and provide suggestions for future work.

Chapter 2
Finite-Difference Frequency-Domain Technique

2.1 Introduction to the Simulation of Plasmonic Devices

The Finite-Difference Frequency-Domain (FDFD) technique is a general-purpose numerical technique for the solution of Maxwell's equations of electromagnetism in the frequency domain. It can be applied to structures of any length scale and for sources of electromagnetic radiation of any frequency. Here, however, the focus is on the use of this technique in nanooptics, and in particular plasmonics.

As described in Chapter 1, plasmonics is a rapidly evolving field of science and technology based on surface plasmons, which are electromagnetic waves that propagate along the interface of a metal and a dielectric. In surface plasmons, light interacts with the free electrons of the metal, which oscillate collectively in response to the applied field. Recently, nanometer scale metallic devices have shown the potential to manipulate light at the subwavelength scale using surface plasmons [47]. This could lead to photonic circuits of nanoscale dimensions.

Surface plasmons can be described by macroscopic electromagnetic theory, i.e., Maxwell's equations, if the electron mean free path in the metal is much shorter than the plasmon wavelength [48]. This condition is usually fulfilled at optical frequencies [48]. In macroscopic electromagnetic theory, bulk material properties, such as dielectric constant, are used to describe objects irrespective of their size. Here, all materials are assumed to be nonmagnetic ($\mu = \mu_0$) and are characterized by their bulk dielectric constant $\epsilon(\mathbf{r}, \omega)$, where $\mathbf{r}=(x, y, z)=x\hat{x} + y\hat{y} + z\hat{z}$, and ω is the angular frequency. However, for particles of nanometer dimensions a more

fundamental description of their optical and electronic properties may be required [49].

Analytical methods, such as Mie theory [50], can only be applied to planar geometries or to objects of specific shapes (spheres, cylinders) and have therefore limited importance in the analysis of plasmonic devices and structures. Numerical simulation techniques are therefore very important for the analysis and design of plasmonic devices. Numerical modeling of plasmonic devices involves several challenges which need to be addressed. First, as mentioned above, plasmonic devices can have arbitrary geometries. Several techniques are specific for one type of geometrical configuration and are therefore not appropriate for modeling of arbitrary plasmonic devices.

Second, the dielectric constant of metals at optical wavelengths is complex, i.e., $\epsilon_r(\omega) = \epsilon_{Re}(\omega) + \epsilon_{Im}(\omega)$ and is a complicated function of frequency [51]. Thus, several simulation techniques which are limited to lossless, nondispersive materials are not applicable to plasmonic devices. In addition, in time-domain methods the dispersion properties of metals have to be approximated by suitable analytical expressions [52]. In most cases, the Drude model is invoked to characterize the frequency dependence of the metallic dielectric function [53]

$$\epsilon_{r,\mathrm{Drude}}(\omega) = 1 - \frac{\omega_p^2}{\omega(\omega + i\gamma)}, \tag{2.1}$$

where ω_p and γ are frequency-independent parameters. However, the Drude model approximation is valid over a limited wavelength range [53]. The range of validity of the Drude model can be extended by adding Lorentzian terms to Eq. (2.1) to obtain the Lorentz-Drude model [53]

$$\epsilon_{r,\mathrm{LD}}(\omega) = \epsilon_{r,\mathrm{Drude}}(\omega) + \sum_{j=1}^{k} \frac{f_j \omega_j^2}{(\omega_j^2 - \omega^2) - i\omega\gamma_j}, \tag{2.2}$$

where ω_j and γ_j stand for the oscillator resonant frequencies and bandwidths, respectively, and f_j are weighting factors. Physically, the Drude and Lorentzian terms are related to intraband (free-electron) and interband (bound-electron) transitions, respectively [53]. Even though the Lorentz-Drude model extends the range of validity of analytical approximations to metallic dielectric constants, it is not suitable for description of sharp absorption edges observed in some metals, unless a very large number of terms are used [53]. In particular, the Lorentz-Drude model cannot approximate well the onset of interband absorption in noble metals (Ag, Au, and Cu), even if five Lorentzian terms are used [53]. In Fig. 2.1, the Drude and Lorentz-Drude models are compared with experimental data for silver. It is observed that even a five-term Lorentz-Drude model with optimal parameters results in a factor of two error at certain frequencies.

Third, in surface plasmons propagating along the interface of a metal and a dielectric, the field is concentrated at the interface, and decays exponentially away from the interface in both the metal and dielectric regions [25]. Thus, for numerical methods based on discretization of the fields on a numerical grid, a very fine grid resolution is required at the metal-dielectric interface to adequately resolve the local fields. In addition, several plasmonic devices are based on components of subwavelength dimensions [25]. In fact, most of the potential applications of surface plasmons are related to subwavelength optics. The nanoscale feature sizes of plasmonic devices pose an extra challenge to numerical simulation techniques.

The challenges involved in modeling plasmonic devices will be illustrated here using a simple example: an infinite periodic array of silver cylinders illuminated by a plane wave at normal incidence (inset of Fig. 2.2(a)). The FDFD method, which is described in detail below, is used to calculate the transmission of the periodic array. This method allows one to directly use experimental data for the

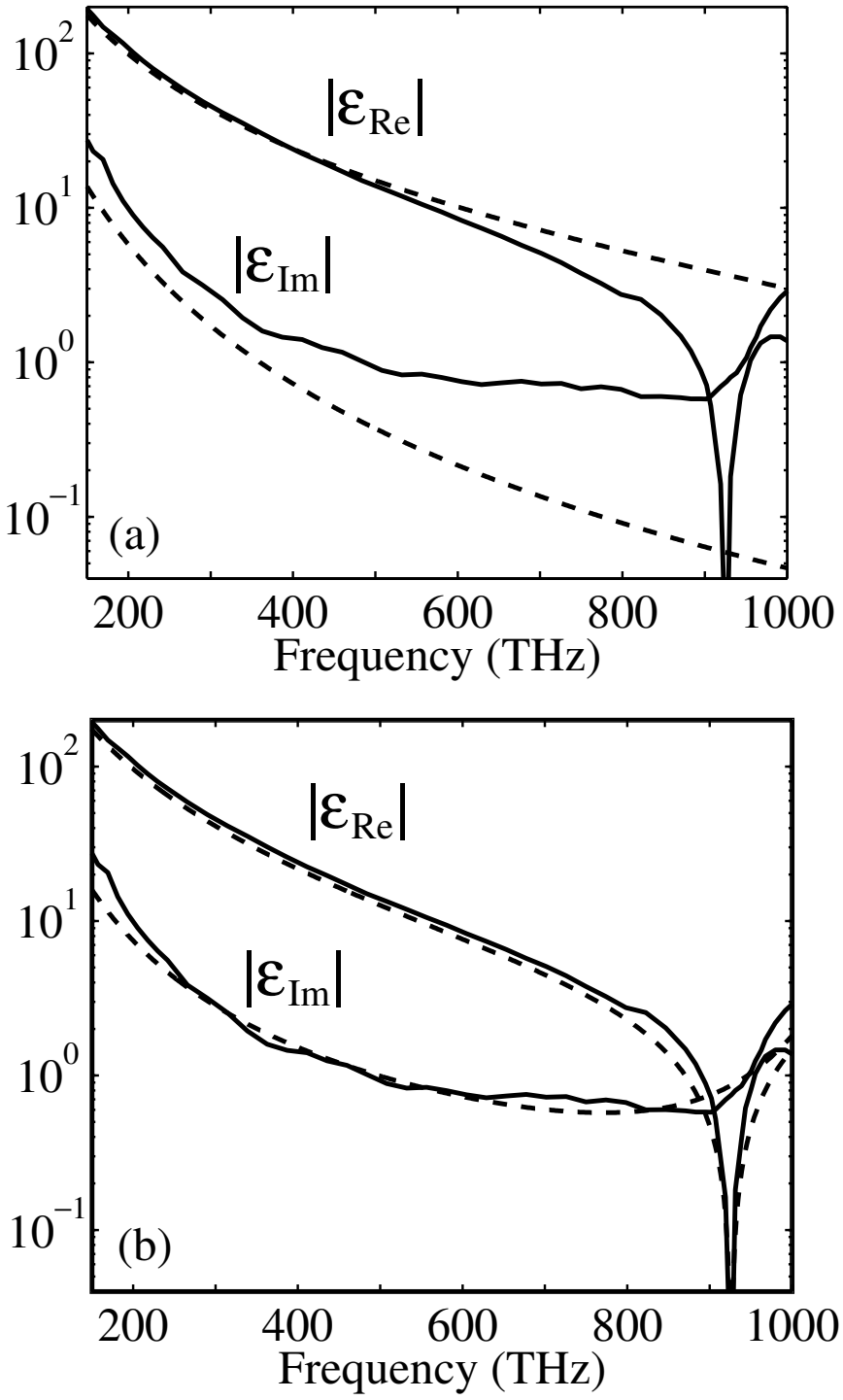

FIGURE 2.1. Real and imaginary part of the dielectric constant of silver at optical frequencies. The solid lines show experimental data [51]. The dashed lines show values calculated using (a) the Drude model and (b) the Lorentz-Drude model with five Lorentzian terms. The parameters of the models are optimal and obtained through an optimization procedure [53].

frequency-dependent dielectric constant of metals, including both the real and imaginary parts, with no approximation. The fields are discretized on a uniform two-dimensional (2-D) grid with grid size $\Delta x = \Delta y = \Delta l$. The calculated transmission as a function of frequency is shown in Fig. 2.2(a). Also shown is the transmission of the structure calculated with the Drude model of equation (2.1). It is observed that the use of the Drude model results in substantial error. In general, the Drude model parameters are chosen to minimize the error in the dielectric function in a given frequency range [54]. However, this approach gives accurate results in a limited wavelength range, as illustrated in this example. In general, the complicated dispersion properties of metals at optical frequencies pose a challenge in modeling of plasmonic devices not encountered in modeling of low- or high-index contrast dielectric devices.

The calculated transmission at a specific wavelength as a function of the spatial grid size Δl is shown in Fig. 2.2(b). It is observed that a grid size of $\Delta l \approx$1nm is required in this case to yield reasonably accurate results. The required grid resolution is directly related to the decay length of the fields at the metal-dielectric interface. In general, modeling of plasmonic devices requires much finer gird resolution than modeling of low- or high-index-contrast dielectric devices, due to the high localization of the field at metal-dielectric interfaces of plasmonic devices. The required grid size depends on the shape and feature size of the modeled plasmonic device, the metallic material used, and the operating frequency.

In the following sections, the FDFD technique is introduced, and it is also examined how FDFD addresses the challenges mentioned above.

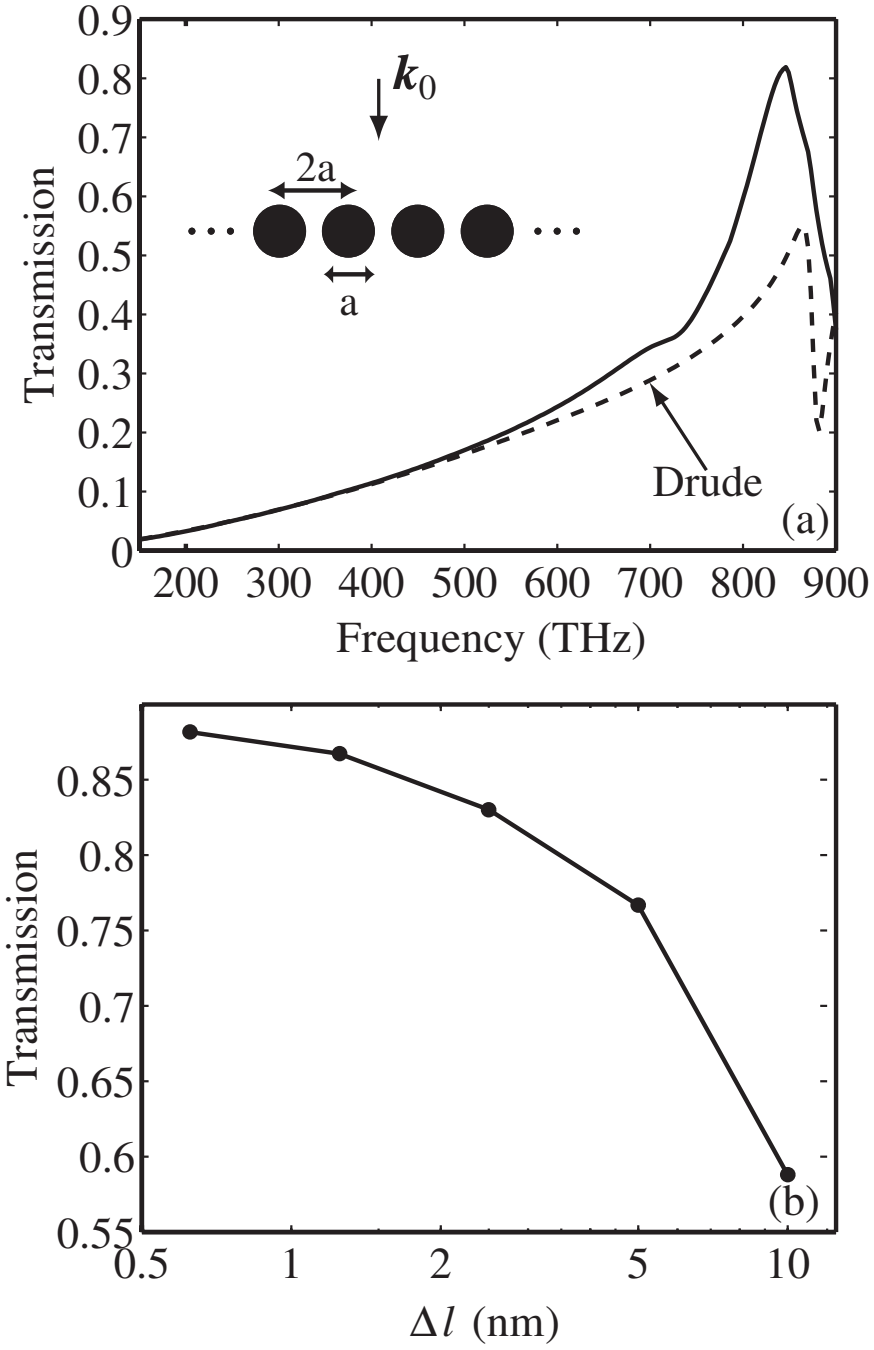

FIGURE 2.2. (a) Calculated transmission spectrum of an infinite array of silver cylinders (shown in the inset) for normal incidence and transverse magnetic (TM) polarization (involving only the E_x, E_y and H_z vector field components). Results are shown for a diameter $a = 100$ nm. The dashed line shows the transmission spectrum calculated using the Drude model equation (2.1) with parameters $\omega_p = 1.37{\times}10^{16}\mathrm{s}^{-1}$ and $\gamma = 7.29{\times}10^{13}\mathrm{s}^{-1}$. (b) Calculated transmission at 855 THz as a function of the spatial grid size Δl.

2.2 Introduction to Finite-Difference Methods

FDFD is based on approximating the derivatives in Maxwell's equations by finite differences. A brief overview of the main features of finite-difference methods is therefore first provided here. In finite-difference methods, derivatives in differential equations are approximated by finite differences. To approximate the derivative $df/dx|_{x_0}$ Taylor series expansions of $f(x)$ about the point x_0 at the points $x_0 + \Delta x$ and $x_0 - \Delta x$ are used to obtain [52]

$$\left.\frac{df}{dx}\right|_{x_0} = \frac{f(x_0 + \Delta x) - f(x_0 - \Delta x)}{2\Delta x} + O[(\Delta x)^2]. \tag{2.3}$$

Here, the notation $O[(\Delta x)^2]$ (to be read as "order $(\Delta x)^2$") denotes the remainder term and indicates its dependence on Δx, i.e., that it approaches zero as the second power of Δx. Thus, Eq. (2.3) shows that a central-difference approximation of the first derivative is second-order accurate, meaning that the remainder term in Eq. (2.3) approaches zero as the square of Δx.

In finite-difference methods a continuous problem is approximated by a discrete one. Field quantities are defined on a discrete grid of nodes. The rectangular grid with node coordinates $\mathbf{r}_{ijk} = (x_i, y_j, z_k)$ is the simplest and most commonly-used. A field quantity at nodal location $\mathbf{r}_{ijk}$ is denoted for convenience as $f_{ijk} = f(\mathbf{r}_{ijk})$. Based on Eq. (2.3), the first derivative can be approximated by the following central-difference formula

$$\left.\frac{df}{dx}\right|_i \simeq \frac{f_{i+1} - f_{i-1}}{2\Delta x}, \tag{2.4}$$

which is second-order accurate, based on the discussion above, if the rectangular grid is uniform, i.e. $x_i = i\Delta x$. For example, if the numerical resolution in the x direction is increased by a factor of 10 ($\Delta x' = \Delta x/10$), then the error introduced by the finite-difference formula in Eq. (2.4) reduces roughly by a factor of $10^2 = 100$.

Similarly, the second derivative can be approximated by the formula

$$\left.\frac{d^2 f}{dx^2}\right|_i \simeq \frac{f_{i+1} - 2f_i + f_{i-1}}{(\Delta x)^2}, \tag{2.5}$$

which is also second-order accurate on a uniform grid [52].

By replacing derivatives in differential equations with their finite-difference approximations, we obtain algebraic equations which relate the value of the field at a specific node to the values at neighboring nodes. By applying the finite-difference approximation to all nodes of the grid, a system of linear equations of the form $\mathbf{Ax} = \mathbf{b}$ is obtained. Since the equation for the field at each point involves only the fields at the four (six in three dimensions, two in one dimension) adjacent points, the resulting system matrix is extremely sparse. Such problems can be solved efficiently if direct or iterative sparse matrix techniques are used.

2.3 The FDFD Method in One Dimension

The FDFD equations will now be derived by approximating the spatial derivatives in Maxwell's equations with finite differences. Assuming an $\exp(i\omega t)$ harmonic time dependence for all field quantities, Maxwell's curl equations in the frequency domain take the form

$$\nabla \times \mathbf{E}(\mathbf{r}) = -i\omega\mu_0 \mathbf{H}(\mathbf{r}), \tag{2.6}$$

$$\nabla \times \mathbf{H}(\mathbf{r}) = \mathbf{J}(\mathbf{r}) + i\omega\epsilon \mathbf{E}(\mathbf{r}). \tag{2.7}$$

It should be noted that the field vectors $\mathbf{E}(\mathbf{r}, t)$, $\mathbf{H}(\mathbf{r}, t)$ are real (measurable) quantities that can vary with time, whereas the vectors $\mathbf{E}(\mathbf{r}, \omega)$, $\mathbf{H}(\mathbf{r}, \omega)$ are complex phasors that do not vary with time. The former can be obtained from the latter by multiplying by $\exp(i\omega t)$ and taking the real part. For example,

$$\mathbf{E}(\mathbf{r}, \mathbf{t}) = Re\{\mathbf{E}(\mathbf{r}) e^{i\omega t}\}. \tag{2.8}$$

It should also be noted that in most cases for simplicity the frequency dependence of the complex phasors is not explicitly shown, e.g., $\mathbf{E}(\mathbf{r})$ is used instead of $\mathbf{E}(\mathbf{r},\omega)$. Maxwell's equations can be simplified by considering electromagnetic fields and systems with no variations in two dimensions, namely, both y and z. By dropping all the y and z derivatives in Eqs. (2.6) and (2.7), and assuming a current source polarized in the z direction ($\mathbf{J} = J_z\hat{z}$), Maxwell's equations simplify to

$$\frac{\partial E_z}{\partial x} = i\omega\mu_0 H_y, \tag{2.9}$$

$$\frac{\partial H_y}{\partial x} = J_z + i\omega\varepsilon E_z. \tag{2.10}$$

In the Finite-Difference Time-Domain (FDTD) technique a staggered spatial grid, known as the Yee grid [52], is used for interleaved placement of the electric and magnetic fields. The Yee grid enables the approximation of the continuous derivatives in space by second-order-accurate two-point centered finite differences. Since the spatial derivatives involved in Maxwell's equations in the frequency domain are exactly the same as those in the time domain, the Yee grid can also be used in FDFD. The placement of the electric and magnetic fields on a one-dimensional (1-D) Yee grid for FDFD is identical to the one for FDTD, and is shown in Fig. 2.3.

For simplicity a uniform rectangular grid with $x_i = i\Delta x$ is considered, and the derivatives in Eqs. (2.9) and (2.10) are replaced with their finite-difference approximations to obtain

$$\frac{E_z\Big|_{i+1} - E_z\Big|_i}{\Delta x} = i\omega\mu_0 H_y\Big|_{i+1/2}, \tag{2.11}$$

$$\frac{H_y\Big|_{i+1/2} - H_y\Big|_{i-1/2}}{\Delta x} = J_z\Big|_i + i\omega\varepsilon\Big|_i E_z\Big|_i. \tag{2.12}$$

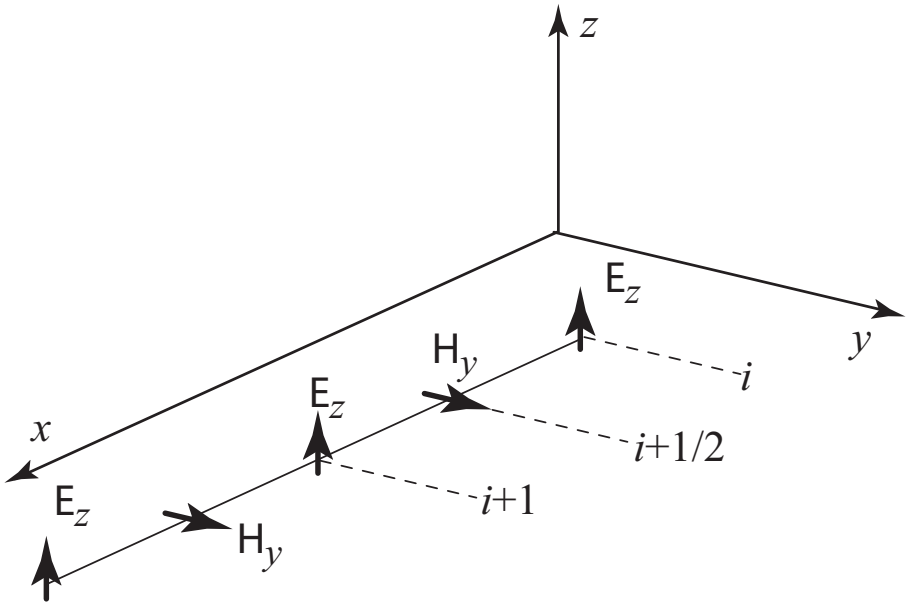

FIGURE 2.3. The placement of electric and magnetic field vectors in FDFD for Maxwell's equations in one dimension.

As mentioned above, by applying Eqs. (2.11) and (2.12) at all points in the Yee grid, a system of linear equations is obtained, which can be solved to find the electromagnetic fields. If the system obtained from Eqs. (2.11) and (2.12) was directly solved, all electric fields ($E_z\Big|_1$, $E_z\Big|_2$, ..., $E_z\Big|_{N_x+1}$), and all magnetic fields ($H_y\Big|_{1+1/2}$, $H_y\Big|_{2+1/2}$, ..., $H_y\Big|_{N_x+1/2}$) would have to be included in the vector of unknown fields. (A 1-D Yee grid terminated at electric field positions was assumed here). Thus, the system of linear equations would have a total of $2N_x+1$ unknowns. However, in the system of equations obtained from the FDFD algorithm, it is straightforward to eliminate either all the electric or all the magnetic fields. To see this, Eq. (2.11) is applied at two adjacent grid points:

$$\frac{1}{i\omega\mu_0}\frac{E_z\Big|_i - E_z\Big|_{i-1}}{\Delta x} = H_y\Big|_{i-1/2}, \tag{2.13}$$

$$\frac{1}{i\omega\mu_0}\frac{E_z\Big|_{i+1} - E_z\Big|_i}{\Delta x} = H_y\Big|_{i+1/2}. \tag{2.14}$$

Equations (2.13) and (2.14) are now substituted into Eq. (2.12) to obtain

$$\frac{1}{\Delta x}\left[\frac{1}{i\omega\mu_0}\frac{E_z\Big|_{i+1}-E_z\Big|_i}{\Delta x}-\frac{1}{i\omega\mu_0}\frac{E_z\Big|_i-E_z\Big|_{i-1}}{\Delta x}\right]=J_z\Big|_i+i\omega\varepsilon\Big|_i E_z\Big|_i, \tag{2.15}$$

which can also be written as

$$\frac{1}{\mu_0}\frac{E_z\Big|_{i+1}-E_z\Big|_i}{(\Delta x)^2}-\frac{1}{\mu_0}\frac{E_z\Big|_i-E_z\Big|_{i-1}}{(\Delta x)^2}+\omega^2\varepsilon\Big|_i E_z\Big|_i=i\omega J_z\Big|_i. \tag{2.16}$$

Thus, application of finite-difference approximations at the node location x_i results in a linear algebraic equation which relates the field $E_z\Big|_i$ to the fields at the two adjacent nodes $E_z\Big|_{i-1}$ and $E_z\Big|_{i+1}$. By applying the finite-difference approximation to all internal nodes of the grid, a system of linear equations of the form $\mathbf{Ax}=\mathbf{b}$ is obtained, where $\mathbf{b}$ is determined by the source current $\mathbf{J}$:

$$\begin{aligned} a_{i\,i-1} &= a_{i\,i+1}=\frac{1}{(\Delta x)^2},\\ a_{i\,i} &= -\frac{2}{(\Delta x)^2}+\omega^2\varepsilon\Big|_i\mu_0,\\ b_i &= i\omega\mu_0 J_z\Big|_i,\\ x_i &= E_z\Big|_i. \end{aligned} \tag{2.17}$$

The FDFD equations for the boundary nodes depend on the boundary conditions at the boundary of the simulation domain. Typically, they involve only the two outermost nodes, e.g., $a_{11}x_1+a_{12}x_2=0$. Thus, in the 1-D case the linear system matrix $\mathbf{A}$ is tridiagonal, and it is straightforward to eliminate the magnetic fields, and obtain a system of equations which only involves the electric fields ($E_z\Big|_1$, $E_z\Big|_2$, ..., $E_z\Big|_{N_x+1}$) and has a total of N_x+1 unknowns.

Finally, if Eqs. (2.9) and (2.10) are combined, the Helmholtz equation in 1-D is obtained:

$$\frac{\partial^2 E_z}{\partial x^2}+\omega^2\varepsilon\mu_0 E_z=i\omega\mu_0 J_z. \tag{2.18}$$

When the spatial derivatives in this equation are approximated by centered finite differences, Eq. (2.16) above is obtained. In other words, the FDFD equations can be directly obtained by discretizing the Helmholtz equation for the electric field.

2.4 The FDFD Method in Two and Three Dimensions

For the 2-D case, it is assumed that there are no variations of either the fields or the excitation in one of the directions, say the z direction. Thus, all derivatives with respect to z drop out from the two curl equations (2.6) and (2.7). A current source polarized in the z direction ($\mathbf{J} = J_z\hat{z}$) is also assumed, so that only the transverse electric (TE) polarization (involving only the H_x, H_y and E_z vector field components) is excited [52] and Maxwell's equations simplify to

$$\begin{aligned} \frac{\partial E_z}{\partial y} &= -i\omega\mu_0 H_x, \\ \frac{\partial E_z}{\partial x} &= i\omega\mu_0 H_y, \\ \frac{\partial H_y}{\partial x} - \frac{\partial H_x}{\partial y} &= J_z + i\omega\epsilon E_z. \end{aligned} \tag{2.19}$$

If the above equations are combined, the 2-D Helmholtz equation is obtained

$$\frac{\partial^2 E_z}{\partial x^2} + \frac{\partial^2 E_z}{\partial y^2} + \omega^2\varepsilon\mu_0 E_z = i\omega\mu_0 J_z. \tag{2.20}$$

As mentioned in the previous section, the exact same FDTD Yee grid can be used in FDFD. A portion of the Yee grid for the TE case is depicted in Fig. 2.4.

The FDFD equations can be obtained by discretizing Eq. (2.19). It is then straightforward to eliminate H_x and H_y to obtain the FDFD equations which only involve the E_z field. Here, however, the 2-D Helmholtz equation (2.20) is discretized to directly obtain the FDFD equations which only involve the E_z field. Once E_z is calculated by solving the FDFD equations, the H_x and H_y fields can be calculated by using the discretized versions of Eq. (2.19).

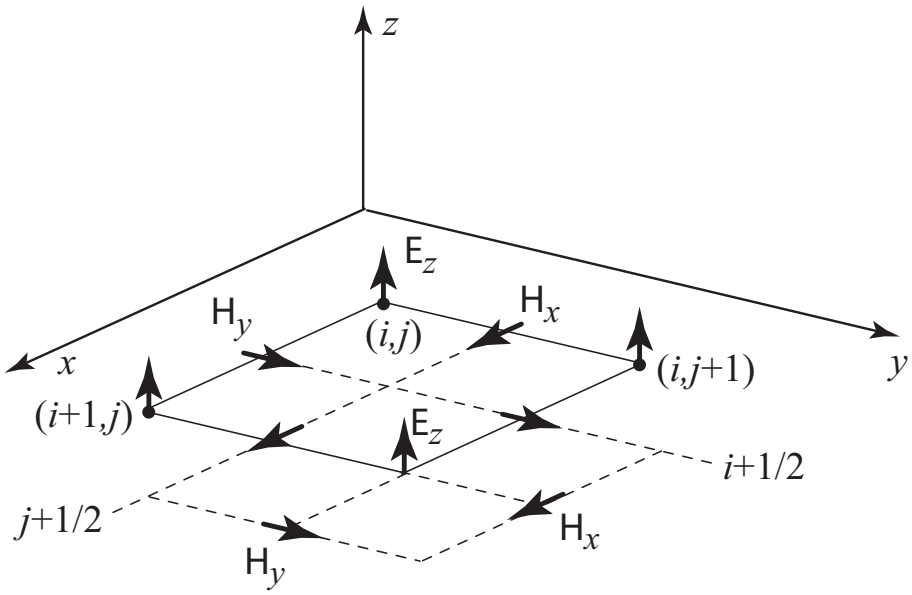

FIGURE 2.4. An FDFD unit cell for transverse electric (TE) waves. The small vectors with thick arrows are placed at the point in the grid at which they are defined. For example, E_z is defined at grid points (i, j), while H_y is defined at grid points (i + 1/2, j).

For simplicity a uniform rectangular grid with $x_i = i\Delta x$ and $y_j = j\Delta y$ is considered, and the derivatives in Eq. (2.20) are replaced with their finite-difference approximations to obtain

$$\frac{E_z\Big|_{i+1,j} - 2E_z\Big|_{i,j} + E_z\Big|_{i-1,j}}{(\Delta x)^2} + \frac{E_z\Big|_{i,j+1} - 2E_z\Big|_{i,j} + E_z\Big|_{i,j-1}}{(\Delta y)^2} + \omega^2\varepsilon\Big|_{i,j}\mu_0 E_z\Big|_{i,j} = i\omega\mu_0 J_z\Big|_{i,j}. \tag{2.21}$$

Thus, application of finite-difference approximations at the node location $\mathbf{r}_{ij} = (x_i, y_j)$ results in a linear algebraic equation which relates the field $E_z\Big|_{i,j}$ to the fields at the four adjacent nodes $E_z\Big|_{i-1,j}, E_z\Big|_{i+1,j}, E_z\Big|_{i,j-1}, E_z\Big|_{i,j+1}$. In the end, the finite-difference approximation is applied to all nodes of the grid to obtain one FDFD equation at each grid point (i, j). These equations form a system of linear equations $\mathbf{Ax} = \mathbf{b}$ with $(N_x + 1) \times (N_y + 1)$ equations and unknowns. The vector of unknown fields $\mathbf{x}$ will include the electric fields at all mesh points (i, j), where $i = 1, 2, ..., N_x + 1$, and $j = 1, 2, ..., N_y + 1$. Note that $\mathbf{x}$ is a one-dimensional vector.

We should therefore construct a one-to-one mapping between the two-dimensional electric field $E_z\Big|_{i,j},\ i = 1, 2, ..., N_x + 1,\ j = 1, 2, ..., N_y + 1$ and the one-dimensional vector of unknown fields $x_m,\ m = 1, 2, ..., (N_x + 1) \times (N_y + 1)$. Choosing the right mapping is in general important and can affect the convergence of the system of linear equations. One simple mapping function in the two-dimensional case is:

$$m(i, j) = (i - 1)(N_y + 1) + j. \tag{2.22}$$

Using this one-to-one mapping function, the following system of linear equations is obtained:

$$\begin{aligned}
a_{m(i,j)m(i-1,j)} &= a_{m(i,j)m(i+1,j)} = \frac{1}{(\Delta x)^2}, \\
a_{m(i,j)m(i,j-1)} &= a_{m(i,j)m(i,j+1)} = \frac{1}{(\Delta y)^2}, \\
a_{m(i,j)m(i,j)} &= -\frac{2}{(\Delta x)^2} - \frac{2}{(\Delta y)^2} + \omega^2 \varepsilon\Big|_{i,j} \mu_0, \\
b_{m(i,j)} &= i\omega\mu_0 J_z\Big|_{i,j}, \\
x_{m(i,j)} &= E_z\Big|_{i,j}.
\end{aligned} \tag{2.23}$$

The same approach can be applied to obtain the FDFD equations for the 2-D TM case as well as for the 3-D case.

2.5 Numerical Dispersion of the FDFD Algorithm

A single plane wave propagating in a uniform medium has a simple dispersion relation connecting the angular frequency ω and the wave number $k : \omega = ck$ [55], where c is the speed of light in the medium. Numerical techniques such as the FDFD technique introduce numerical dispersion. To derive the dispersion properties of the FDFD algorithm, a single wave or Fourier mode in space is considered. The dispersive properties of FDFD are assessed by obtaining the dispersion relation of

the scheme, relating the frequency of a Fourier mode on the grid to a particular wavelength λ (or wave number k):

$$\omega = f_{\mathrm{FDFD}}(k, \Delta x). \tag{2.24}$$

In the 1-D case, a plane wave propagating in a uniform medium is considered

$$E(x) = e^{\sqrt{-1}kx}, \tag{2.25}$$

and its discretized version is

$$E\Big|_i = e^{\sqrt{-1}ki\Delta x}. \tag{2.26}$$

In the above equations, $\sqrt{-1}$ was used to avoid confusing it with the grid index i. In a uniform medium with no sources the FDFD equation (2.16) becomes

$$\frac{E_z\Big|_{i+1} - 2E_z\Big|_i + E_z\Big|_{i-1}}{(\Delta x)^2} + \omega^2 \varepsilon \mu_0 E_z\Big|_i = 0. \tag{2.27}$$

Equation (2.26) is substituted into Eq. (2.27) to find

$$\frac{e^{\sqrt{-1}ki\Delta x}(e^{\sqrt{-1}k\Delta x} - 2 + e^{-\sqrt{-1}k\Delta x})}{(\Delta x)^2} + \omega^2 \varepsilon \mu_0 e^{\sqrt{-1}ki\Delta x} = 0, \tag{2.28}$$

from which one obtains

$$\omega = ck \left(\frac{\sin(\frac{k\Delta x}{2})}{\frac{k\Delta x}{2}} \right). \tag{2.29}$$

Equation (2.29) is the dispersion relation of 1-D FDFD. It is observed that, in the limit $\Delta x \to 0$, Eq. (2.29) reduces to the exact dispersion relation $\omega = ck$. Using Eq. (2.29), the numerical phase velocity $\bar{v}_p \equiv \frac{\omega}{k}$ and group velocity $\bar{v}_g \equiv \frac{\partial \omega}{\partial k}$ of the FDFD scheme can be derived. The numerical phase velocity of 1-D FDFD as a function of the numerical resolution $\Delta x/\lambda$ is shown in Fig. 2.5. It is observed, for example, that for a spatial resolution of 20 grid points per wavelength ($\Delta x/\lambda$=0.05) the numerical error in the phase velocity is less than 1%.

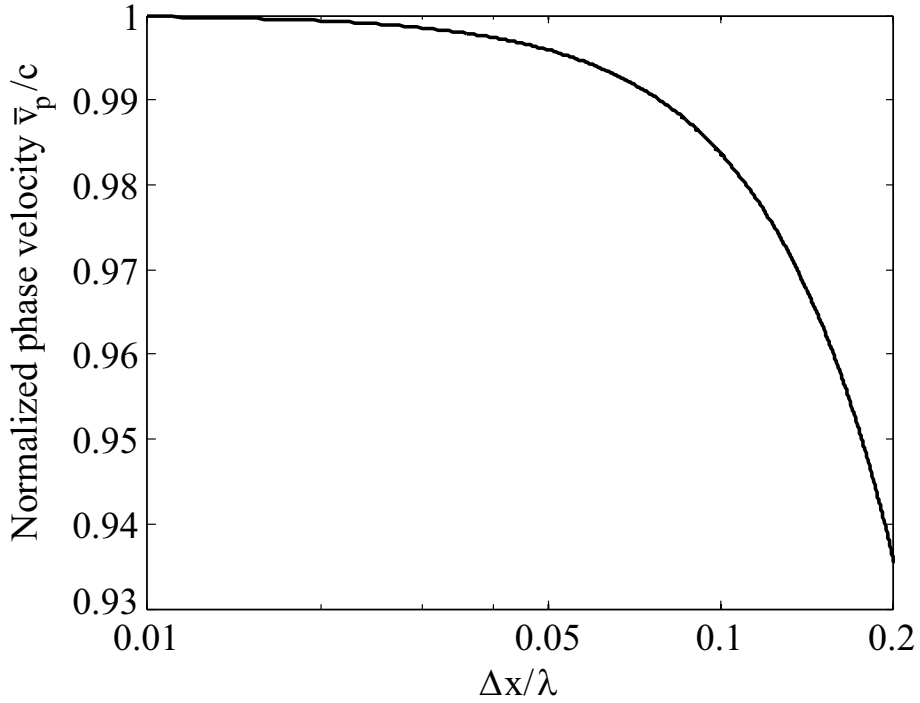

FIGURE 2.5. Dispersion of 1-D FDFD. Variation of numerical phase velocity with numerical resolution $\Delta x/\lambda$ in 1-D FDFD.

In the 2-D case, wave-like modes propagating in both x and y directions are considered

$$E(x,y) = e^{\sqrt{-1}(k_x x + k_y y)}, \tag{2.30}$$

and their discretized version is

$$E\Big|_{i,j} = e^{\sqrt{-1}(k_x i\Delta x + k_y j\Delta y)}, \tag{2.31}$$

where k_x and k_y are the wave numbers in the x and y directions, respectively.

In a uniform medium with no sources, the 2-D FDFD equation (2.21) becomes

$$\frac{E_z\Big|_{i+1,j} - 2E_z\Big|_{i,j} + E_z\Big|_{i-1,j}}{(\Delta x)^2} + \frac{E_z\Big|_{i,j+1} - 2E_z\Big|_{i,j} + E_z\Big|_{i,j-1}}{(\Delta y)^2} + \omega^2\varepsilon\mu_0 E\Big|_{i,j} = 0. \tag{2.32}$$

Equation (2.31) is substituted into Eq. (2.32) to find after some manipulation:

$$\omega^2 = c^2\left[k_x^2\left(\frac{\sin(\frac{k_x\Delta x}{2})}{\frac{k_x\Delta x}{2}}\right)^2 + k_y^2\left(\frac{\sin(\frac{k_y\Delta y}{2})}{\frac{k_y\Delta y}{2}}\right)^2\right]. \tag{2.33}$$

It is observed again that, in the limit $\Delta x \to 0$, $\Delta y \to 0$, Eq. (2.33) reduces to the exact dispersion relation $\omega^2 = c^2(k_x^2 + k_y^2)$.

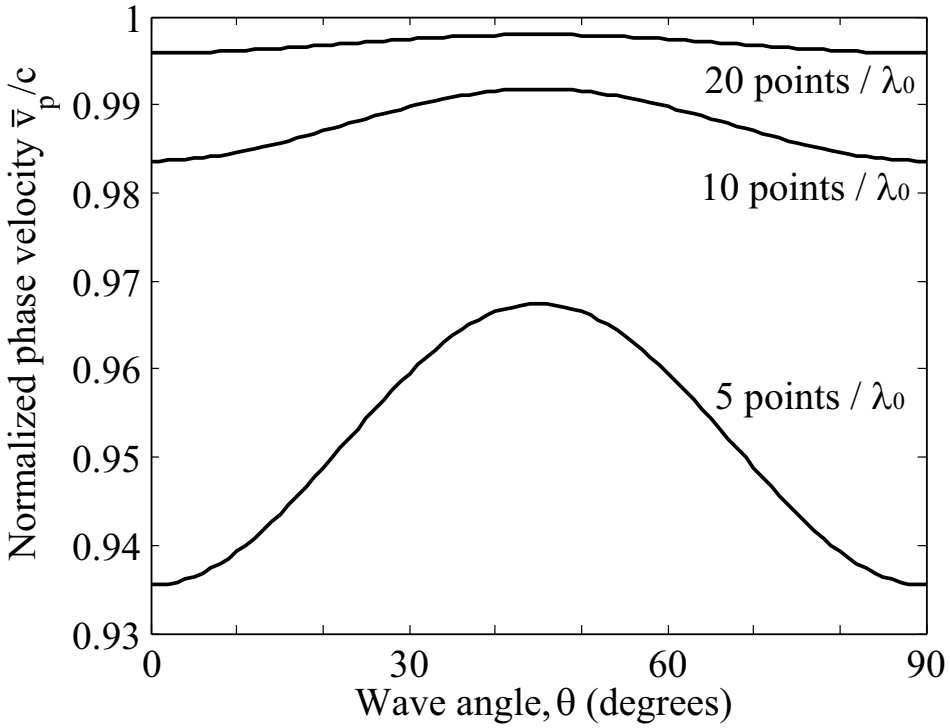

FIGURE 2.6. Dispersion of 2-D FDFD. Variation of numerical phase velocity with wave-propagation angle in a 2-D FDFD grid for three different cases of numerical resolution.

It can be seen from Eq. (2.33) that the numerical phase velocity $\bar{v}_p$ for the 2-D case is a function of angle of propagation through the FDFD grid. To see this, wave propagation at an angle θ with respect to the positive x axis is assumed, in which case $k_x = k\cos\theta$ and $k_y = k\sin\theta$, where $k = \sqrt{k_x^2 + k_y^2}$ is the wave number. Figure 2.6 shows a plot of normalized numerical phase velocity as a function of propagation angle θ. The dependence is, in general, relatively small (compared to dispersion errors due to the discretized grid), with $\bar{v}_p/c$ varying by only a few percent between $\theta = 45°$ and $\theta = 0°$, even for very coarse (e.g., $\Delta x = \Delta y = \lambda_0/5$) spatial grids. The dependence of $\bar{v}_p/c$ on propagation angle θ is known as grid anisotropy and is a source of additional numerical dispersion effects.

Finally, it is noted that, unlike FDTD, in FDFD only the spatial derivatives are approximated by finite differences. In fact, for time-harmonic sources and fields the FDTD equations reduce to the FDFD equations in the limit of $\Delta t \to 0$.

2.6 Comparison to Other Numerical Techniques

FDFD is a frequency-domain technique, and can thus treat arbitrary material dispersion. Nonuniform and/or nonorthogonal grids are required in FDFD for efficient treatment of curved surfaces and rapid field variations at material interfaces. In FDFD, as in all other methods which are based on discretization of the differential form of Maxwell's equations in a finite volume, absorbing boundary conditions (ABCs) are required, so that waves are not artificially reflected at the boundaries of the computational domain. Very efficient and accurate ABCs, such as the perfectly matched layer (PML) [52, 56], have been demonstrated for FDFD. As mentioned above, FDFD results in extremely sparse systems of linear equations. Such problems can be solved efficiently if direct or iterative sparse matrix techniques are used.

FDTD is also a finite-difference method, so its performance in modeling plasmonic devices is similar to the performance of FDFD. There are many similarities between the two techniques. Both can be used to model structures with arbitrary geometries. In addition, many of the methods used in combination with FDTD (total field/scattered field method, etc.) can also be used with FDFD. However, there are some major differences. First, as mentioned above, in time-domain methods the dispersion properties of metals have to be approximated by suitable analytical expressions which introduce substantial error in broadband calculations. In addition, the implementation of methods for dispersive materials in FDTD requires

additional computational cost and extra memory storage [52, 57]. On the other hand, in FDTD it is possible to obtain the entire frequency response with a single simulation by exciting a broadband pulse and calculating the Fourier transform of both the excitation and the response [52].

The Finite-Element Frequency-Domain (FEFD) method is a more powerful technique than FDFD, especially for problems with complex geometries. However, FDFD is conceptually simpler and easier to program. The main advantage of FEFD is that complex geometric structures can be discretized using a variety of elements of different shapes, while in FDFD a rectangular grid is typically used leading to staircase approximations of particle shapes [56, 58]. In addition, in FEFD fields within elements are approximated by shape functions, typically polynomials, while in FDFD a simpler piecewise constant approximation is used [58]. In short, FEFD is more complicated than FDFD but achieves better accuracy for a given computational cost [58].

Chapter 3

Numerical Simulations of Plasmonic Waveguide Devices

3.1 Calculation of Transmission, Reflection and Absorption Spectra

Using the FDFD method described on the previous chapter, I can calculate the field patterns when light propagates in a plasmonic waveguide device. In addition to the field patterns, I am also interested in calculating how much power is transmitted through the device, how much power is reflected, and how much power is absorbed in the device.

Using the fields calculated with the FDFD method, I can calculate the power flux P through a given surface A as

$$P = \int_A \mathbf{S} \cdot d\mathbf{A} = \int_A \frac{1}{2} Re\{\mathbf{E} \times \mathbf{H}^*\} \cdot d\mathbf{A}, \tag{3.1}$$

where $\mathbf{S} = \frac{1}{2} Re\{\mathbf{E} \times \mathbf{H}^*\}$ is the time-averaged Poynting vector representing the electromagnetic power flux density in units of $\frac{W}{m^2}$. In the two-dimensional case, I calculate the power flux per unit length.

To calculate the transmission T of a plasmonic waveguide device I perform two simulations. I first excite the waveguide mode before the device, and measure the power flux of the transmitted optical mode P_1 after the device. I perform a similar simulation in a straight waveguide and measure the power flux P_0. By comparing the two cases, I extract the power transmission of the plasmonic waveguide device as

$$T = \frac{P_1}{P_0}. \tag{3.2}$$

To obtain the transmission spectra $T(\omega)$, I perform these simulations over a range of frequencies. As an example, in Figs. 3.1(a) and 3.1(b) I show the simulations

I need to perform to calculate the transmission T of a structure consisting of a plasmonic MDM waveguide side-coupled to two MDM stub resonators [59]. I am interested in the regime where the waveguide width w is much smaller than the wavelength ($w \ll \lambda$), so that only the fundamental TM mode is propagating. Thus, for such a structure I can simply use a dipole point source to excite the optical mode (Fig 3.1).

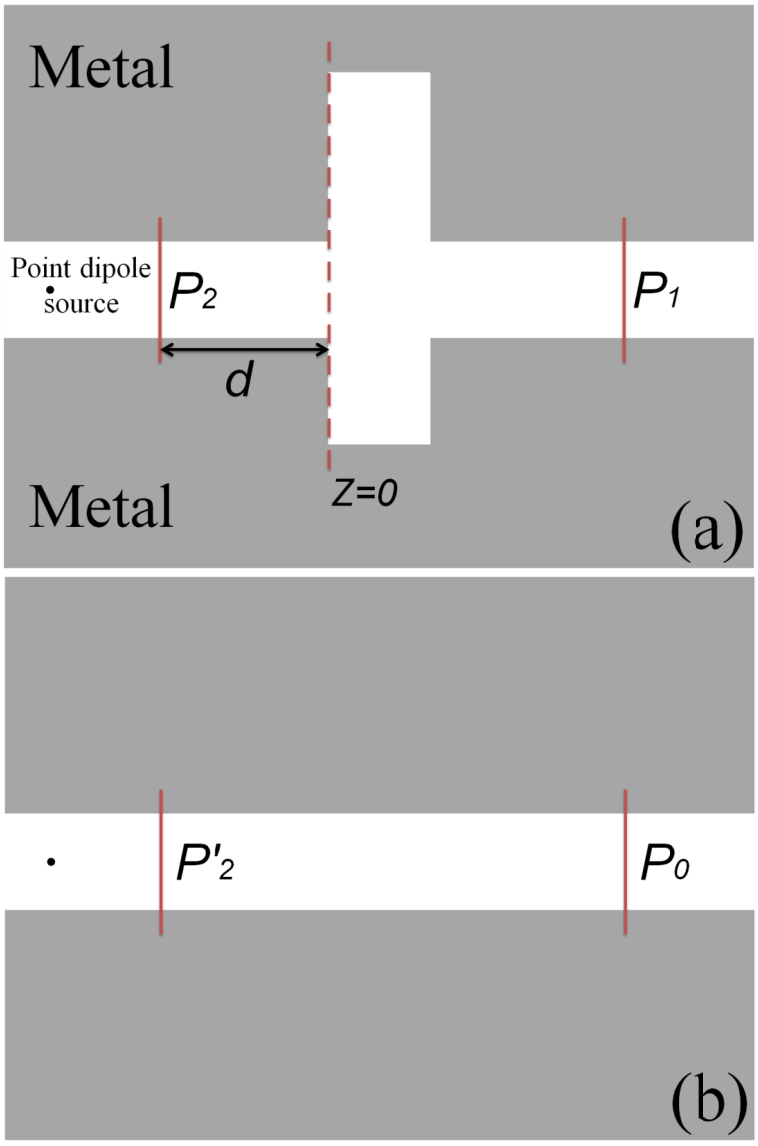

FIGURE 3.1. (a) Schematic of a simulation of a plasmonic waveguide device consisting of two MDM stub resonators side-coupled to a MDM waveguide. (b) Schematic of the simulation of a straight MDM waveguide which is used for normalization.

To calculate the power reflection spectra, I need to calculate the power of the incident and reflected mode in the input waveguide. At a given frequency, the power reflection of the plasmonic waveguide device is

$$R = \frac{P_r\big|_{z=0}}{P_{inc}\big|_{z=0}}, \tag{3.3}$$

where $P_r\big|_{z=0}$ and $P_{inc}\big|_{z=0}$ represent the incident and reflected power flux at $z = 0$, respectively. However, to eliminate the effect of near fields, I numerically calculate the power flux at a distance d away from $z = 0$, i.e. P_2 in Fig. 3.1(a), instead of $P\big|_{z=0}$.

At $z = -d$ I have

$$P_2 \equiv P\big|_{z=-d} = P_{inc}\big|_{z=-d} - P_r\big|_{z=-d}. \tag{3.4}$$

Here $P_{inc}\big|_{z=-d}$ can be obtained by performing a simulation in a straight waveguide so that $P_2^{'} = P_{inc}\big|_{z=-d}$ (Fig. 3.1(b)). I therefore have

$$P_r\big|_{z=-d} = P_2^{'} - P_2. \tag{3.5}$$

Since the power is proportional to the square of the field amplitude, I have

$$P_r\big|_{z=0} = e^{2\gamma_{\mathrm{MDM}}d} P_r\big|_{z=-d} = e^{2\gamma_{\mathrm{MDM}}d}(P_2^{'} - P_2), \tag{3.6}$$

and

$$P_{inc}\big|_{z=0} = e^{-2\gamma_{\mathrm{MDM}}d} P_{inc}\big|_{z=-d} = e^{-2\gamma_{\mathrm{MDM}}d} P_2^{'}, \tag{3.7}$$

where γ_{MDM} is the complex wave vector of the fundamental propagating TM mode in such a MDM waveguide. Substituting the above two equations into equation (3.4), the power reflection can be calculated at a given frequency as

$$R = \frac{e^{2\gamma_{\mathrm{MDM}}d}(P_2^{'} - P_2)}{e^{-2\gamma_{\mathrm{MDM}}d} P_2^{'}} = \frac{e^{4\gamma_{\mathrm{MDM}}d}(P_2^{'} - P_2)}{P_2^{'}}. \tag{3.8}$$

By performing these calculations over a range of frequencies, I can obtain the power reflection spectra. Finally, using $A = 1 - T - R$, which is obtained by applying the conservation of energy, I can also calculate the absorption spectra of the structure.

3.2 Calculation of Dispersion Relation

The dispersion relation describes the interrelation between two wave properties, the frequency ω and wavevector β, i.e. $\omega(\beta)$. Here I describe a method to calculate

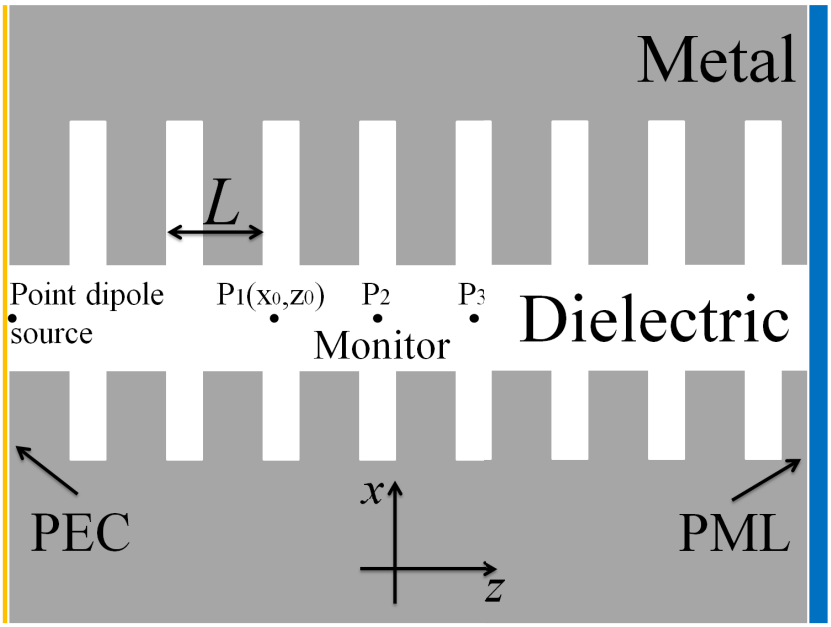

FIGURE 3.2. Schematic of a plasmonic waveguide system consisting of a periodic array of two MDM stub resonators side-coupled to a MDM waveguide. I use three field monitors to extract the wavevector of such system.

the dispersion relation of a periodic waveguide system using the FDFD method. As an example, I calculate the dispersion of a plasmonic waveguide system consisting of a periodic array of two MDM stub resonators side-coupled to a MDM waveguide (Fig. 3.2). I use a dipole point source to excite the optical mode of the system (Fig. 3.2). I also use a perfect electric conductor (PEC) boundary condition to reduce the simulation domain size by a factor of 2 (Fig. 3.2). In the regime of interest,

the periodic waveguide structure supports a single propagating Bloch mode. In addition, when using a single dipole point source to excite the right propagating mode, the left propagating mode is also excited due numerical reflections from the PML layer. Thus, I have

$$H_y(x,z) = A_1 u(x,z) e^{-\gamma z} + A_2 u(x,z) e^{\gamma z}, \tag{3.9}$$

where A_1, A_2 are the complex amplitudes of the right and left propagating modes, respectively, $\gamma = \alpha + j\beta$ is the complex Bloch wave vector of the entire system, and the function u is periodic in z, i.e. $u(x, z+L) = u(x,z)$.

In the field expression in equation (3.9), I have three unknowns, A_1, A_2, and γ, so I need three equations to extract them. I measure the field at three locations (P_1, P_2, P_3) with distance of L between them, where L is the period. I then have

$$\begin{aligned} A_1^{'} + A_2^{'} &= B_1, \\ A_1^{'} t + A_2^{'} \frac{1}{t} &= B_2, \\ A_1^{'} t^2 + A_2^{'} \frac{1}{t^2} &= B_3, \end{aligned} \tag{3.10}$$

where $t = e^{-\gamma L}, A_1^{'} = A_1 u(x_0, z_0) e^{-\gamma z_0}, A_2^{'} = A_2 u(x_0, z_0) e^{\gamma z_0}$, and $B_i = H_y[x_0, z_0 + (i-1)L], i = 1, 2, 3$. By solving this system, the parameter t can be found. Finally, I obtain the Bloch wave vector using

$$\gamma = -\frac{\ln t}{L}. \tag{3.11}$$

The real part of $\gamma, \alpha \equiv Re(\gamma)$ is associated with the material loss in the metal. The propagating mode is attenuated with an attenuation length $\frac{1}{\alpha}$, which is usually referred to as the propagation length of the mode L_p. The imaginary part of γ, $\beta \equiv Im(\gamma)$ is related to the dispersion relation $\omega = \omega(\beta)$. I perform these simulations over a range of frequencies to obtain the dispersion relation $\omega = \omega(\beta)$.

3.3 Total Field/Scattered Field Formulation

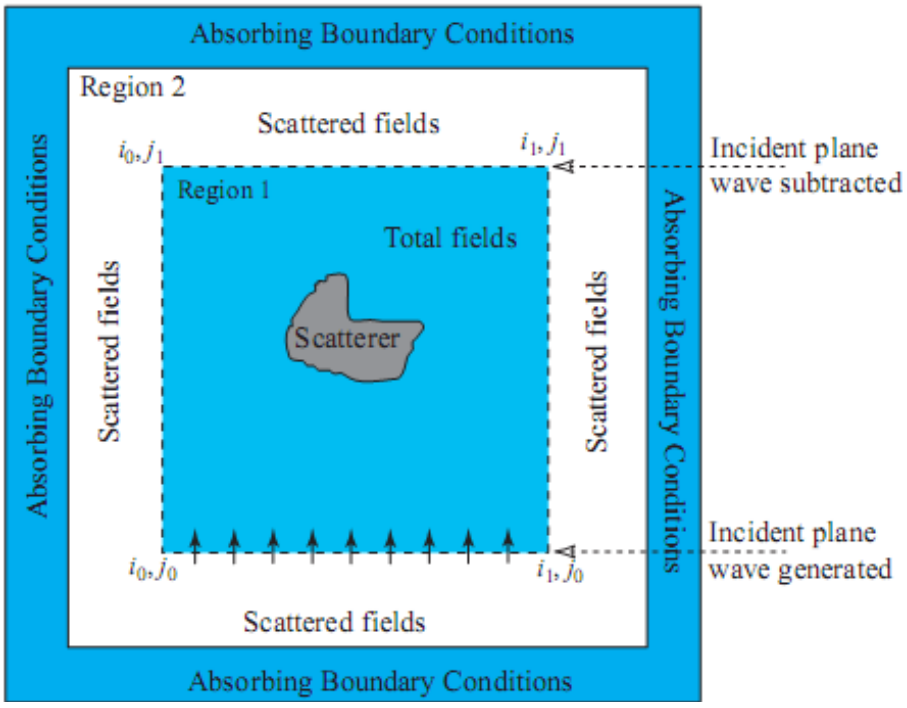

FIGURE 3.3. Schematic of a total-field/scattered-field simulation domain with several regions identified [60].

Many electromagnetic problems involve the interaction of objects with an incident plane wave. I define the incident field as the field which is present in a free space region in the absence of any objects or scatterers. On the other hand, the scattered field is the field which results from the presence of the scatterers. Finally, the total field is the superposition of the incident and scattered fields. I use a total-field/scattered-field formulation to simulate an incident plane wave. The total-field/scattered-field formulation is based on applying Maxwell's equations to the total field in region 1, and to the scattered field in region 2, with appropriate connecting conditions on the adjoining interfaces (Fig. 3.3). The incident fields are used in the connecting conditions, and only need to be calculated at the interface between these two regions.

For a 2-D TE simulation, Maxwell's equations simplify to

$$\begin{aligned} \frac{\partial E_z}{\partial y} &= -i\omega\mu_0 H_x, \\ \frac{\partial E_z}{\partial x} &= i\omega\mu_0 H_y, \\ \frac{\partial H_y}{\partial x} - \frac{\partial H_x}{\partial y} &= i\omega\epsilon E_z. \end{aligned} \tag{3.12}$$

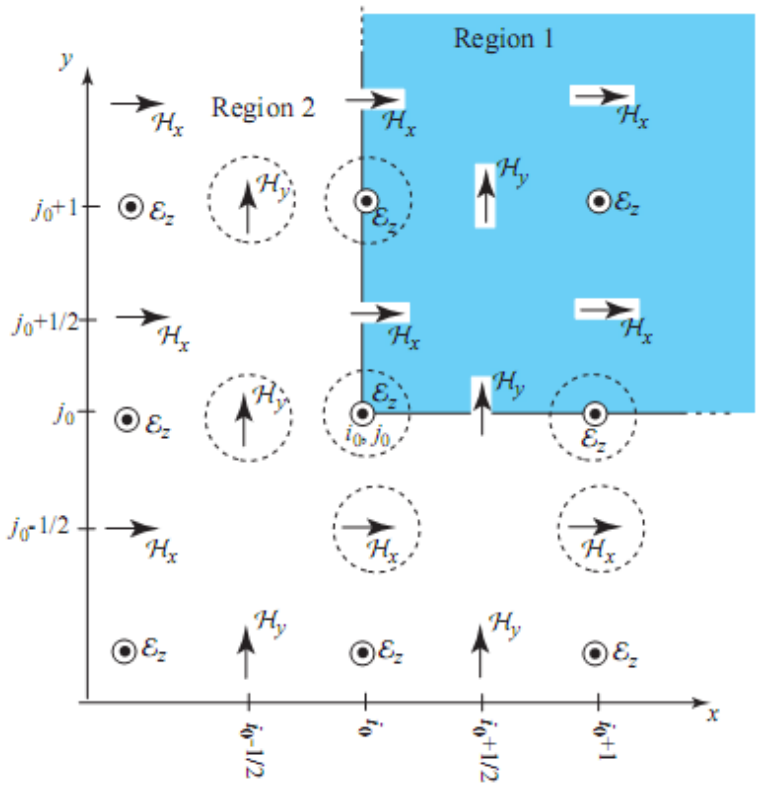

FIGURE 3.4. The lower left corner of the boundary between the total fields and scattered fields regions showing the locations where field components are defined for a 2-D TE simulation using the total field/scattered field method.

Now consider the lower left corner of the boundary between the total fields and scattered fields regions (Fig. 3.4). At grid point ($i = i_0, j = j_0$), I have (Section 2.5)

$$\frac{H_y^{tot}\Big|_{i_0+\frac{1}{2},j_0} - H_y^{sca}\Big|_{i_0-\frac{1}{2},j_0}}{\Delta x} - \frac{H_x^{tot}\Big|_{i_0,j_0+\frac{1}{2}} - H_x^{sca}\Big|_{i_0,j_0-\frac{1}{2}}}{\Delta y} = i\omega\epsilon E_z^{tot}\Big|_{i_0,j_0}. \tag{3.13}$$

Note that E_z at $i = i_0, j = j_0$ is a total field. Equation (3.14) as written above is not correct, since the spatial derivatives are expressed by a mix of total and scattered field components. To fix this inconsistency, I use the linearity of Maxwell's equations

$$H_y^{tot}\Big|_{i_0-\frac{1}{2},j_0} = H_y^{inc}\Big|_{i_0-\frac{1}{2},j_0} + H_y^{sca}\Big|_{i_0-\frac{1}{2},j_0}, \tag{3.14}$$

$$H_x^{tot}\Big|_{i_0,j_0-\frac{1}{2}} = H_x^{inc}\Big|_{i_0,j_0-\frac{1}{2}} + H_x^{sca}\Big|_{i_0,j_0-\frac{1}{2}}. \tag{3.15}$$

Thus, the correct form of the above equation is

$$\begin{aligned} i\omega\epsilon E_z^{tot}\Big|_{i_0,j_0} = & \frac{H_y^{tot}\Big|_{i_0+\frac{1}{2},j_0} - H_y^{sca}\Big|_{i_0-\frac{1}{2},j_0}}{\Delta x} - \frac{H_x^{tot}\Big|_{i_0,j_0+\frac{1}{2}} - H_x^{sca}\Big|_{i_0,j_0-\frac{1}{2}}}{\Delta y} \\ & - \frac{H_y^{inc}\Big|_{i_0-\frac{1}{2},j_0}}{\Delta x} + \frac{H_x^{inc}\Big|_{i_0,j_0-\frac{1}{2}}}{\Delta y}. \end{aligned} \tag{3.16}$$

In analogy to equations (3.13) through (3.16), the scattered magnetic field components $H_y^{sca}\Big|_{i_0-\frac{1}{2},j_0}$, $H_x^{sca}\Big|_{i_0,j_0-\frac{1}{2}}$ adjacent to the corner of the boundary are determined by

$$i\omega\mu_0 H_y^{sca}\Big|_{i_0-\frac{1}{2},j_0} = \frac{E_z^{tot}\Big|_{i_0,j_0} - E_z^{sca}\Big|_{i_0-1,j_0}}{\Delta x} - \frac{E_z^{inc}\Big|_{i_0,j_0}}{\Delta x}, \tag{3.17}$$

$$i\omega\mu_0 H_x^{sca}\Big|_{i_0,j_0-\frac{1}{2}} = -\frac{E_z^{tot}\Big|_{i_0,j_0} - E_z^{sca}\Big|_{i_0,j_0-1}}{\Delta y} + \frac{E_z^{inc}\Big|_{i_0,j_0}}{\Delta y}. \tag{3.18}$$

The other two magnetic field components $H_y^{tot}\Big|_{i_0+\frac{1}{2},j_0}$, and $H_x^{tot}\Big|_{i_0,j_0+\frac{1}{2}}$ adjacent to the corner of the boundary do not require special handling and are given by

$$i\omega\mu_0 H_y^{tot}\Big|_{i_0+\frac{1}{2},j_0} = \frac{E_z^{tot}\Big|_{i_0+1,j_0} - E_z^{tot}\Big|_{i_0,j_0}}{\Delta x}, \tag{3.19}$$

$$i\omega\mu_0 H_x^{tot}\Big|_{i_0,j_0+\frac{1}{2}} = -\frac{E_z^{tot}\Big|_{i_0,j_0+1} - E_z^{tot}\Big|_{i_0,j_0}}{\Delta y}. \tag{3.20}$$

Substituting equations (3.17)-(3.20) into Eq. (3.16), I obtain the final equation for $E_z\Big|_{i_0,j_0}$ in the 2-D FDFD total field-scattered field formulation

$$\frac{E_z^{tot}\Big|_{i_0+1,j_0} - 2E_z^{tot}\Big|_{i_0,j_0} + E_z^{sca}\Big|_{i_0-1,j_0}}{(\Delta x)^2} + \frac{E_z^{tot}\Big|_{i_0,j_0+1} - 2E_z^{tot}\Big|_{i_0,j_0} + E_z^{sca}\Big|_{i_0,j_0-1}}{(\Delta y)^2}$$
$$+ \omega^2\epsilon\mu_0 E_z^{tot}\Big|_{i_0,j_0} = -[\frac{1}{(\Delta x)^2} + \frac{1}{(\Delta y)^2}]E_z^{inc}\Big|_{i_0,j_0} - i\omega\mu_0\frac{H_x^{inc}\Big|_{i_0,j_0-\frac{1}{2}}}{\Delta y}$$
$$+ i\omega\mu_0\frac{H_y^{inc}\Big|_{i_0-\frac{1}{2},j_0}}{\Delta x}. \tag{3.21}$$

By comparing equations (3.21) and (2.21), I observe that the incident fields result in an equivalent current source J_z such that

$$i\omega\mu_0 J_z\big|_{i_0,j_0} = -[\frac{1}{(\Delta x)^2} + \frac{1}{(\Delta y)^2}]E_z^{inc}\Big|_{i_0,j_0} - i\omega\mu_0\frac{H_x^{inc}\Big|_{i_0,j_0-\frac{1}{2}}}{\Delta y}$$
$$+ i\omega\mu_0\frac{H_y^{inc}\Big|_{i_0-\frac{1}{2},j_0}}{\Delta x}. \tag{3.22}$$

Chapter 4

Subwavelength Slow-Light Plasmonic Waveguides Based on a Plasmonic Analogue of Electromagnetically Induced Transparency[1]

4.1 Introduction to Slow Light

Slow wave propagation was observed and widely used in the microwave range as early as the 1940s [61, 62]. The first experimental observation of slow light in the nonlinear regime was made in 1967 by McCall and Hahn [63], and soon afterwards Grischkowsky and others observed slow light in the linear regime [64]. The discovery of EIT gave slow light science a strong impetus [65, 66, 67, 68]. In addition, slow group velocities occur quite commonly in waveguide structures which enable engineering of their dispersion properties such as in photonic crystals [69].

Slow-light methods have direct applicability to the fields of optical telecommunications for applications such as buffering, regeneration, and optical data processing [70, 71]. Slow light can enable delaying and temporarily storing light in all-optical memories. The target application of slow light for optical memory is an all-optical router that temporarily stores data, while identifying the address of a data packet. Electronic buffers typically store megabits of data. The main argument in favor of optical schemes is that the required optical-electronic-optical conversion consumes a lot of power and limits the bandwidth of information. Due to current technology limitations, all-optical buffers are not expected to outperform electronic buffers in

[1]Reprinted with permission from Y. Huang, C. Min, and G. Veronis, "Subwavelength Slow-Light Plasmonic Waveguides Based on a Plasmonic Analogue of Electromagnetically Induced Transparency," *Applied Physics Letters*, 99, 143117 (2011). Copyright 2011, American Institute of Physics.

the near future. However, tunable optical delay lines for synchronizing and time-interleaving streams of data are a more feasible application in the near future, since only modest delays of the order of only a few bits are required.

In addition, nonlinear effects can be enhanced in systems with slow group velocity as a result of the compression of the local energy density [70]. When an optical pulse travels in a slow-light waveguide, it is compressed and its energy density is thereby increased [70]. As nonlinear effects depend on energy density, this means that the strength of the nonlinear interaction effectively scales with the slowdown factor of the waveguide. Slow light can bring spectacular advances to the field of nonlinear optics, enabling sizeable effects to be realized with much lower power levels and with much smaller and cheaper lasers.

Slowing down light in optical waveguides leads to enhanced light-matter interaction, and can, therefore, also enhance the performance of optical devices, such as switches and sensors [70]. This is due to the fact that the sensitivity of the phase of the light signal to the induced change in the index of refraction can be drastically enhanced if one operates in the regime of slow group velocity [69].

Slow-light methods also find applications in quantum optics [70]. In quantum information processing, one of the key issues is to store the quantum state of light for a sufficiently long time to enable quantum operations. Slowing and stopping light are ways to achieve this long storage time [72]. Quantum operations can also be performed in the same system by slowing down two pulses of light simultaneously. The two pulses, when propagating with slow but equal group velocities, interact very efficiently for a long time. This process creates strongly correlated states of interacting photons (entangled photons), which form the basic building blocks of a quantum processor [73].

4.2 Slow-Light Waveguides Based on a Plasmonic Analogue of EIT

As discussed in Chapter 1, plasmonic waveguides have shown the potential to guide and manipulate light at deep subwavelength scales [25]. Slowing down light in plasmonic waveguides leads to enhanced light-matter interaction, and could therefore enhance the performance of nanoscale plasmonic devices such as switches and sensors [74, 75, 76, 77, 78, 79, 80]. Among the different plasmonic waveguiding structures, MDM plasmonic waveguides are of particular interest because they support modes with deep subwavelength scale over a very wide range of frequencies extending from DC to visible [7]. Recently, a MDM plasmonic waveguide system, based on a plasmonic analogue of periodically loaded transmission lines, which supports a guided subwavelength slow-light mode was introduced [80].

In this chapter, I introduce an alternative MDM plasmonic waveguide system, based on a plasmonic analogue of EIT, which also supports a guided subwavelength slow-light mode. EIT is a coherent process observed in three-level atomic media, which allows a narrow transparency window in the spectrum of an otherwise opaque medium, and can slow down light pulses by several orders of magnitude [29]. Since the EIT spectrum results from the interference of resonant pathways [29, 30], it has been recognized that similar interference effects can also occur in classical systems, such as optical waveguides coupled to resonators and metamaterials [29, 31, 32, 33]. In addition, it has been demonstrated that periodic optical waveguides, resulting from cascading structures with EIT-like response, can slow down and even stop light [30, 34, 35].

The proposed structure consists of a periodic array of two MDM stub resonators side-coupled to a MDM waveguide. Side-coupled-cavity structures have been previously proposed as compact filters, reflectors, switches, and impedance matching

elements for plasmonic waveguides [81, 82, 83, 84]. Here I show that the proposed structure supports a band diagram similar to that of EIT systems, with three photonic bands in the vicinity of the two stub resonances. The middle band corresponds to a mode with slow group velocity and zero group velocity dispersion near the middle of this band. I find that decreasing the frequency spacing between

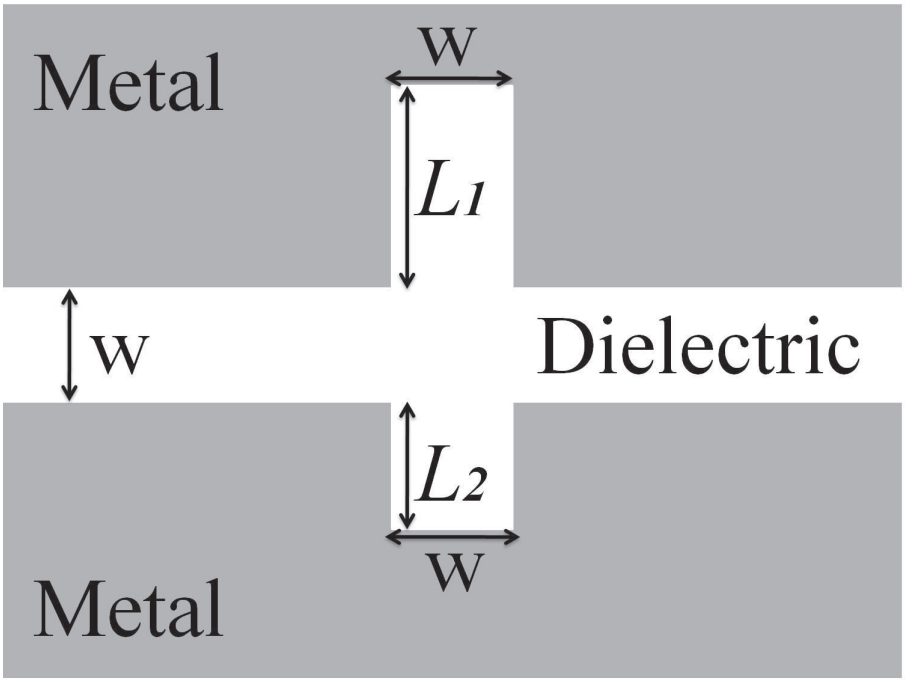

FIGURE 4.1. Schematic of a MDM plasmonic waveguide side-coupled to two MDM stub resonators.

the resonances, increases the slowdown factor, and decreases the bandwidth of the middle band. I also show that there is a trade-off between the slowdown factor and the propagation length of the supported optical mode in such slow-light plasmonic waveguide systems. I use the FDFD method to investigate the properties of the structure [80]. As discussed in Chapter 2, this method allows us to directly use experimental data for the frequency-dependent dielectric constant of metals such as silver [51], including both the real and imaginary parts, with no approximation. PML absorbing boundary conditions are used at all boundaries of the simulation

domain. When simulating the periodic waveguiding structure, I place several periods of the structure within the PML layer to drastically reduce spurious reflections at PML interfaces [80].

4.3 MDM Waveguide Side-Coupled to Two MDM Stub Resonators

I first consider a plasmonic MDM waveguide side-coupled to two MDM stub resonators (Fig. 4.1). The resonant frequencies of the cavities can be tuned by adjusting the cavity lengths L_1 and L_2. This system is a plasmonic analogue of EIT [85, 86]. The MDM waveguide and MDM stub resonators have deep subwavelength widths ($w \ll \lambda$), so that only the fundamental TM mode is propagating. Thus, I can use single-mode scattering matrix theory to account for the behavior of the system [87]. The complex magnetic field reflection coefficient r_1, and transmission coefficients $t_1, t_2 = t_3$ for the fundamental propagating TM mode at a MDM waveguide crossing (Fig. 4.2(a)), as well as the reflection coefficient r_2 at the boundary of a short-circuited MDM waveguide (Fig. 4.2(b)) are numerically extracted using FDFD [87]. The power transmission spectra $T(\omega)$ of the two-cavity system (Fig. 4.1) can then be calculated using scattering matrix theory as

$$T = |t_1 - C|^2 , \tag{4.1}$$

which is in excellent agreement with the exact results obtained using FDFD (Fig. 4.3). Here $C = \frac{t_2^2(2t_1 - 2r_1 + s_1 + s_2)}{t_1^2 - (r_1 - s_1)(r_1 - s_2)}$, $s_i = r_2^{-1} \exp(2\gamma_{\mathrm{MDM}} L_i)$, $i = 1, 2$, and $\gamma_{\mathrm{MDM}} = \alpha_{\mathrm{MDM}} + i\beta_{\mathrm{MDM}}$ is the complex wave vector of the fundamental propagating TM mode in a MDM waveguide of width w. [Equation (4.1) is proved in Appendix A]. The transmission spectra $T(\omega)$ feature two dips (Fig. 4.3). I found that the frequencies ω_1, ω_2 where these dips occur are approximately equal to the first resonant frequencies of the two cavities, i.e. $\phi_{r_1}(\omega_i) + \phi_{r_2}(\omega_i) - 2\beta_{\mathrm{MDM}}(\omega_i) L_i \simeq -2\pi$,

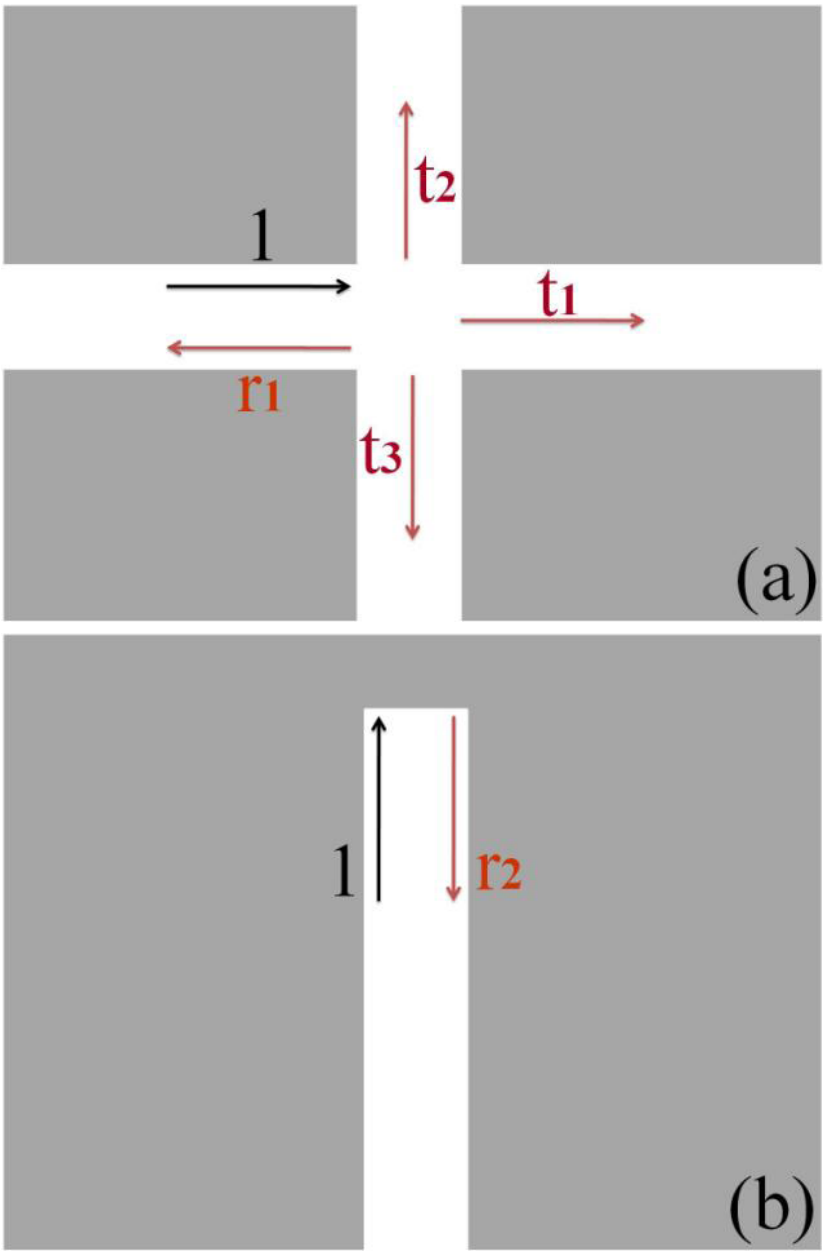

FIGURE 4.2. (a) Schematic defining the reflection coefficient r_1, and transmission coefficients t_1, t_2, t_3 when the fundamental TM mode of the MDM waveguide is incident at a waveguide crossing. Note that $t_2 = t_3$ due to symmetry. (b) Schematic defining the reflection coefficient r_2 of the fundamental TM mode of the MDM waveguide at the boundary of a short-circuited MDM waveguide.

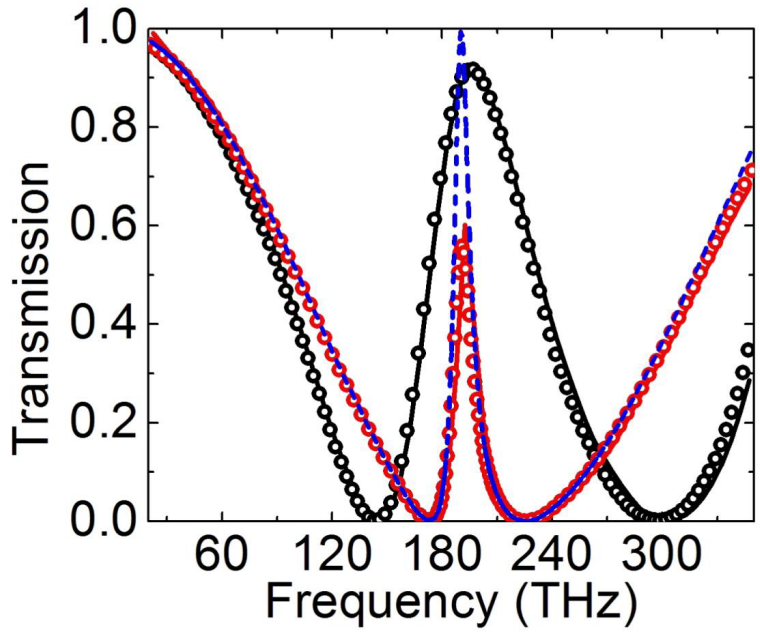

FIGURE 4.3. Transmission spectra for the structure of Fig. 4.1 calculated using FDFD (circles) and scattering matrix theory (solid line) for a silver-air structure with $w = 50$nm. Results are shown for $L_1 = 360$nm, $L_2 = 160$nm (black line and circles), and $L_1 = 295$nm, $L_2 = 220$nm (red line and circles). Also shown are the transmission spectra calculated using FDFD for $L_1 = 295$nm, $L_2 = 220$nm and lossless metal (blue dashed line).

$i = 1, 2$, where $\phi_{r_i} = \arg(r_i)$, $i = 1, 2$. When either one of the cavities is resonant, the field intensity in that cavity is high, while the field intensity in the other cavity is almost zero, since it is far from resonance (Figs. 4.4(a), 4.4(b)). In addition, the transmission is almost zero, since the incoming wave interferes destructively with the decaying amplitude into the forward direction of the resonant cavity field. The transmission spectra $T(\omega)$ also feature a transparency peak centered at frequency ω_0. I found that ω_0 is approximately equal to the first resonant frequency of the composite cavity of length $L_1 + L_2 + w$ formed by the two cavities, i.e. $2\phi_{r_2}(\omega_0) - 2\beta_{\mathrm{MDM}}(\omega_0)(L_1 + L_2 + w) \simeq -2\pi$.

Thus, the transmission peak frequency ω_0 is tunable through the cavity lengths L_1, L_2. When $\omega = \omega_0$, the field intensity is high in the entire composite cavity (Fig. 4.4(c)), and the transmission spectra exhibit a peak due to resonant tunneling of the incoming wave through the composite cavity. The width of the peak is highly

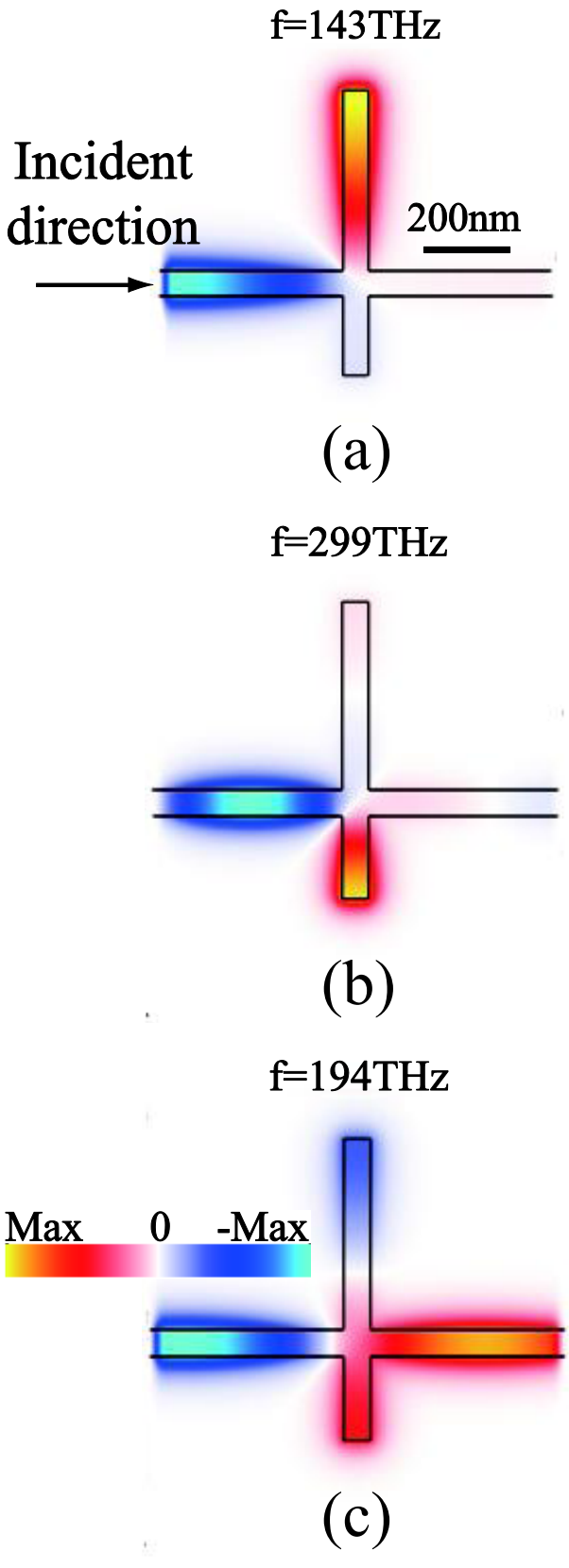

FIGURE 4.4. (a)-(c) Magnetic field profiles for the structure of Fig. 4.1 for $L_1 = 360$nm, $L_2 = 160$nm, $w = 50$nm at $f = 143, 299, 194$THz, when the fundamental TM mode of the MDM waveguide is incident from the left.

sensitive to the frequency spacing between the resonances $\delta\omega = \omega_2 - \omega_1$, which can be tuned by adjusting the stub lengths difference $\delta L = L_1 - L_2$. As $\delta\omega$ decreases, the width of the peak decreases (Fig. 4.3). In the lossless metal case, the center peak can be tuned to be arbitrarily narrow with unity peak transmission (Fig. 4.3). In the presence of loss, the peak transmission decreases, as the frequency spacing $\delta\omega$ decreases (Fig. 4.3).

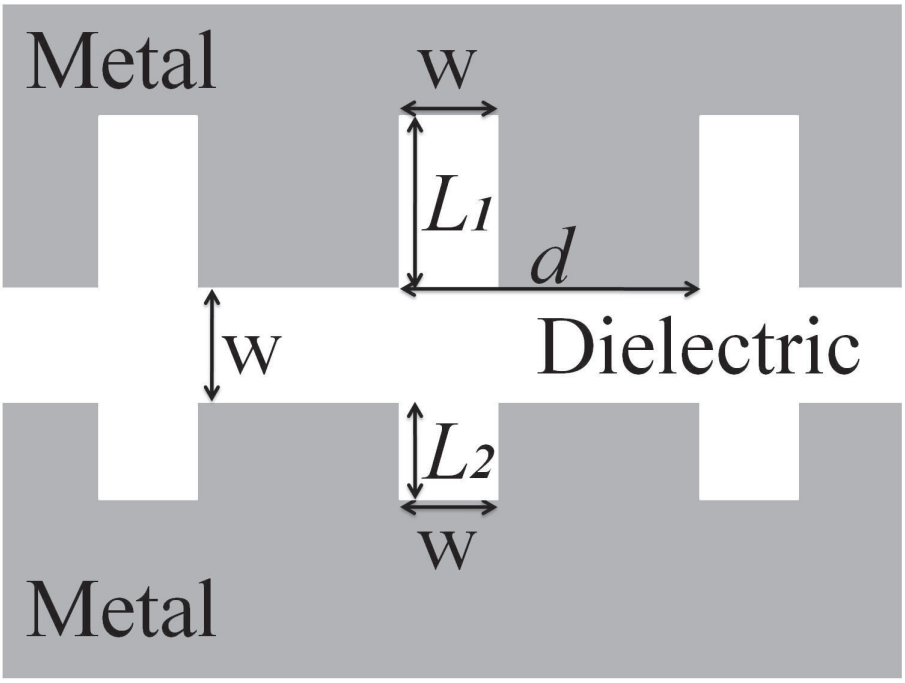

FIGURE 4.5. Schematic of a plasmonic waveguide system consisting of a periodic array of two MDM stub resonators side-coupled to a MDM waveguide.

4.4 Periodic Plasmonic Waveguide System

I next consider the plasmonic waveguide system (Fig. 4.5) obtained by periodically cascading the side-coupled-cavity structure of Fig. 4.1. The periodicity d is subwavelength ($d \ll \lambda$), so that the operating wavelength is far from the Bragg wavelength of the waveguide [80] ($\lambda \gg \lambda_{\text{Bragg}}$). In addition, the distance between adjacent side-coupled cavities $d - w$ is chosen large enough so that direct coupling

between the cavities has a negligible effect on the dispersion relation of the system [80]. Using single-mode scattering matrix theory [87], the dispersion relation between the frequency ω and the Bloch wave vector $\gamma = \alpha + i\beta$ of the entire system is found to be

$$\cosh(\gamma d) = \frac{A}{2}\exp[-\gamma_{\mathrm{MDM}}(d-w)] + \frac{B}{2}\exp[\gamma_{\mathrm{MDM}}(d-w)], \tag{4.2}$$

which is in excellent agreement with the exact results obtained using FDFD (Fig. 4.7). Here $A = (t_1 - r_1)\frac{t_1+r_1-2C}{t_1-C}$, and $B = (t_1 - C)^{-1}$. [Equation (4.2) is proved in Appendix B]. In Fig. 4.6, I show the dispersion relation for the plasmonic waveg-

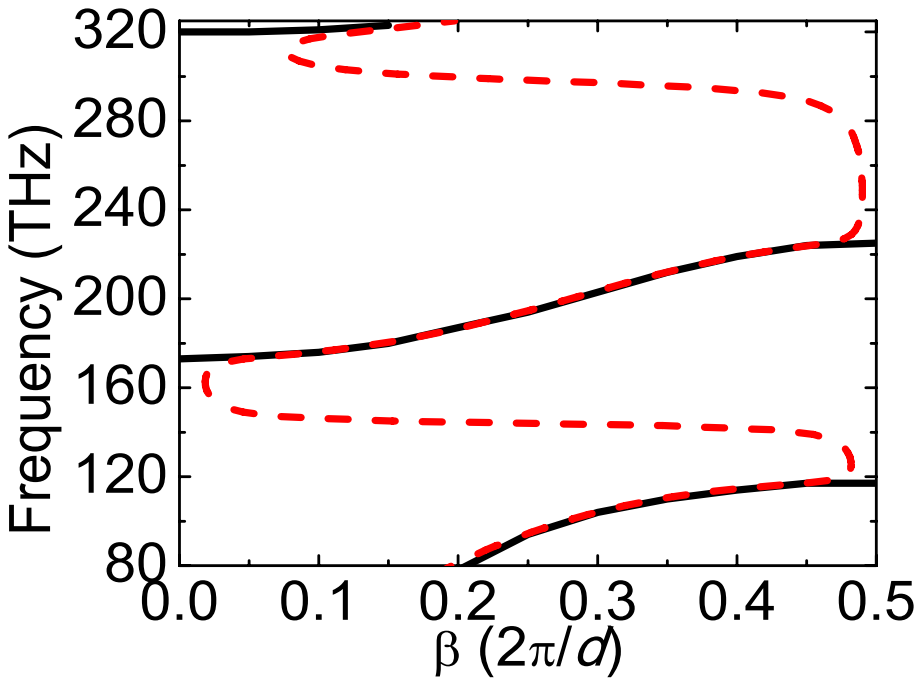

FIGURE 4.6. Dispersion relation of the plasmonic waveguide system of Fig. 4.5 calculated using FDFD (red dashed line). Results are shown for a silver-air structure with $d = 300$nm, $L_1 = 360$nm, $L_2 = 160$nm, and $w = 50$nm. Also shown is the dispersion relation for lossless metal (black solid line).

uiding structure of Fig. 4.5. In the lossless metal case, the system supports three photonic bands in the vicinity of the cavity resonances. The middle band corresponds to a mode with slow group velocity $v_g \equiv \frac{\partial\omega}{\partial\beta}$ and zero group velocity dispersion $\beta_2 \equiv \frac{\partial^2\beta}{\partial\omega^2}$ near the middle of this band (Fig. 4.6). In the two band gaps

between the three bands the system supports non-propagating modes with $\beta = 0$. Such a band diagram is similar to that of EIT systems [34]. When losses in the metal are included, the band structure is unaffected in the frequency range of the three bands except at the band edges (Fig. 4.6). In addition, in the frequency range of the two band gaps the Bloch wave vector γ has an imaginary component ($\beta \neq 0$), and the dispersion relation experiences back-bending [80] with negative group velocity. In addition, the width of the middle band and the slowdown factor c/v_g

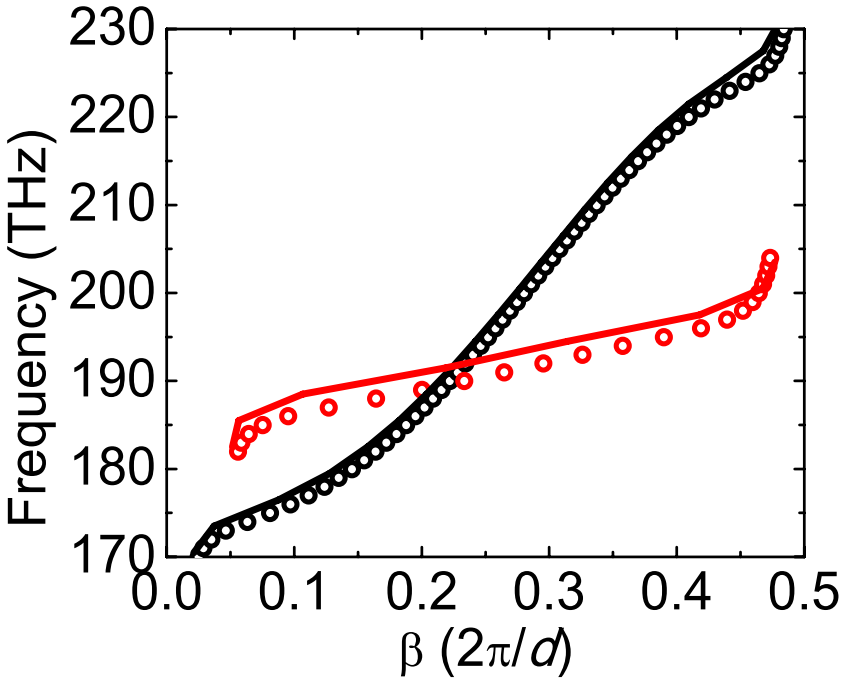

FIGURE 4.7. Dispersion relation of the plasmonic waveguide system of Fig. 4.5 calculated using FDFD (circles) and scattering matrix theory (solid line). Results are shown for $L_1 = 360$nm, $L_2 = 160$nm (black line and circles), and $L_1 = 295$nm, $L_2 = 220$nm (red line and circles). All other parameters are as in Fig. 4.6. In both cases only a portion of the band structure is shown, corresponding to the frequency range of the middle band.

strongly depend on the frequency spacing between the resonances $\delta\omega = \omega_2 - \omega_1$. By decreasing the stub lengths difference δL, $\delta\omega$ decreases, and this leads to decreased bandwidth of the middle band (Fig. 4.7). In Figs. 4.8(a) and 4.8(b) I show the slowdown factor c/v_g, and propagation length L_p for the plasmonic waveguide system of Fig. 4.5 as a function of frequency for two different values of δL. In

both cases I show the frequency range corresponding to the middle band of the system. For a given δL, the propagation length L_{p} of the supported optical mode

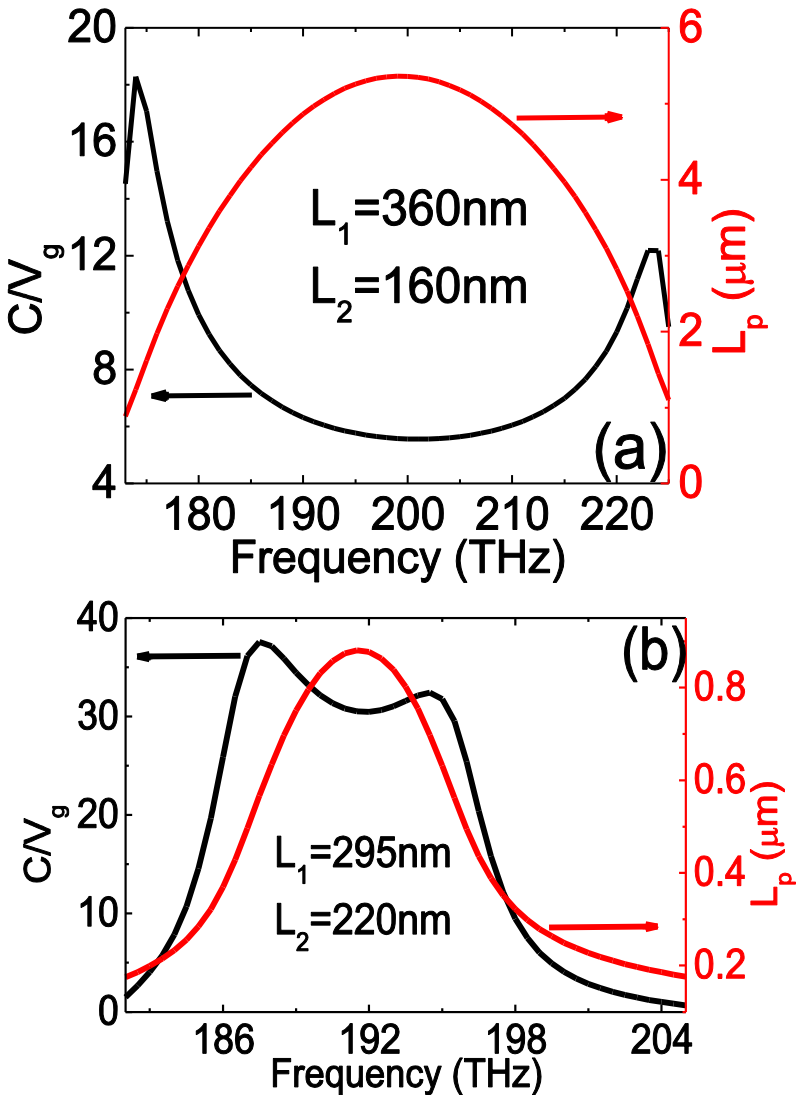

FIGURE 4.8. (a)-(b) Reciprocal of the group velocity v_{g}, and propagation length L_{p} for the plasmonic waveguide system of Fig. 4.5 as a function of frequency calculated using FDFD. Results are shown for $L_1 = 360$nm, $L_2 = 160$nm, and $L_1 = 295$nm, $L_2 = 220$nm. All other parameters are as in Fig. 4.6.

is maximized at a frequency very close to the frequency where the group velocity dispersion is zero. As δL and therefore $\delta\omega$ decrease, the slowdown factor c/v_{g} increases, while the propagation length L_{p} decreases at the frequency of zero group velocity dispersion. Thus, there is a trade-off between the slowdown factor c/v_{g}

and the propagation length L_p of the supported optical mode in such slow-light plasmonic waveguide systems [80]. For $\delta L = 200$nm ($\delta L = 75$nm) I have $c/v_g \simeq 6$ ($c/v_g \simeq 30$) at the frequency where the group velocity dispersion is zero (Figs. 4.8(a) and 4.8(b)).I found that even larger slowdown factors can be obtained by further decreasing δL at the cost of reduced propagation length. I also note that the propagation length of the system for a given slowdown factor can be increased by incorporating gain media in the structure [47].

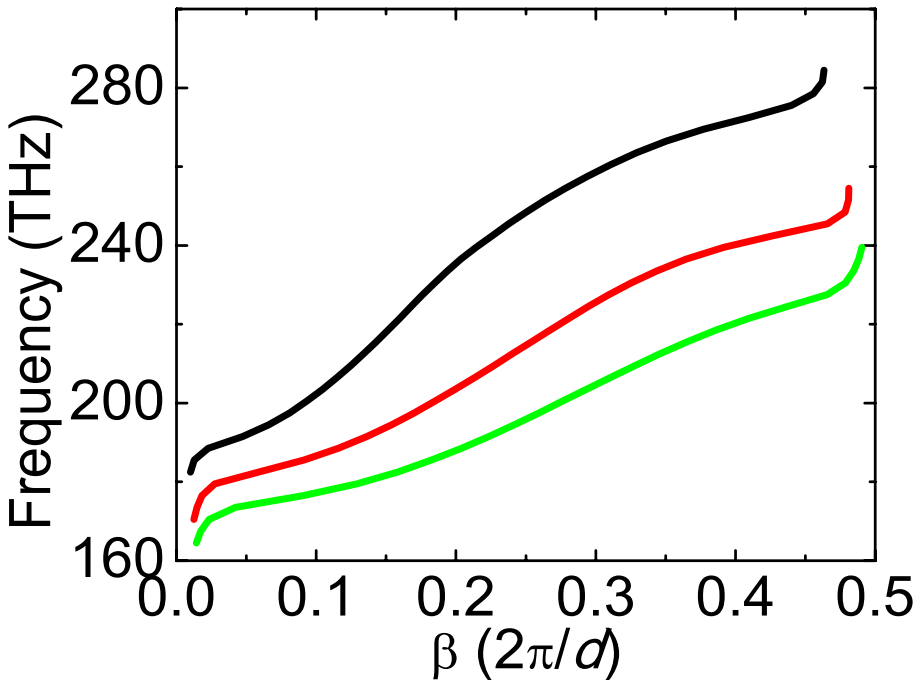

FIGURE 4.9. Dispersion relation of the plasmonic waveguide system of Fig. 4.5 calculated using FDFD. Results are shown for $d = 100$nm (black line), $d = 200$nm (red line), and $d = 300$nm (green line). All other parameters are as in Fig. 4.6. In all cases only a portion of the band structure is shown, corresponding to the frequency range of the middle band.

I also consider the effect of the periodicity d (Fig. 4.5) on the dispersion relation of the system (Fig. 4.9). For large d the distance $d - w$ between adjacent two-cavity structures in the periodic waveguide is large, so that their coupling through the MDM waveguide is weak. In this regime, the frequency range of the middle band of the periodic waveguide system of Fig. 4.5 approximately corresponds to

the frequency range of the transparency peak of the two-cavity structure of Fig. 4.1. As d decreases, the coupling between adjacent two-cavity structures increases. As a result, the slow-light middle band shifts to higher frequencies, while its width slightly broadens (Fig. 4.9). Thus, the periodicity provides us an additional degree of freedom to tune the dispersion relation of the periodic waveguide system.

4.5 Conclusions

In conclusion, I introduced subwavelength slow-light waveguides for enhanced light-matter interaction, based on a plasmonic analogue of EIT. Unlike previously proposed structures [80], such waveguides exhibit a small group velocity dispersion and a large slowdown factor over a broad wavelength range, features which are highly desirable for practical applications of slow-light devices [61]. In addition, if these waveguides are combined with gain and tunable refractive index materials, they could enable stopping and storing light in a subwavelength volume [30].

Chapter 5

Design of Slow-Light Enhanced Ultra-Compact Plasmonic Waveguide Sensors

5.1 Introduction to Optical Sensors

Optical sensors are passive devices which convert variations of certain physical quantities into detectable variations in the intensity, phase, or spectrum of optical signals. By measuring the variations of the optical signal, we try to analyze the desired physical property, and optimize the sensitivity through the light-matter interaction process involved. Compared with their electrical or mechanical counterparts, there are several advantages exhibited by optical sensors. For example, optical devices in general enable high-speed signal processing. Nowadays, optical sensors already play a significant role in a large range of technical applications from traditional integrated optical sensors such as a Mach-Zehnder interferometer, to novel optical biosensors which can be applied to healthcare, drug discovery, and environmental protection [88].

The refractive index (RI) is the fundamental optical property of materials. RI optical sensors, which convert RI variations to optical signals, are the most widely used optical sensors. RI optical sensors which are implemented with a surface plasmon system, are known as surface plasmon resonance (SPR) sensors. As we saw in Chapter 1, surface plasmon polaritons are electromagnetic resonance excitations that are bound to propagate along a metal-dielectric interface. A change in the RI of the dielectric layer will lead to a change of the surface plasmon characteristic wavevector. Since the SPP mode can be confined in a deep subwavelength scale [89, 90], such sensors can be used in nanoscale photonics systems. In addition, most

of the surface wave energy is confined in the dielectric. Therefore, the sensitivity can be drastically enhanced even if there is a small change in the RI of the dielectric.

In a ring resonator, light is guided by total internal reflection between the high RI core layer and the low RI cladding. Since the resonance wavelength of the guided mode can be tuned by the RI of the cladding material, ring resonators can be used as sensors. Ring resonators have been implemented in several structures such as microspheres, microtoroids, microrings, liquid core optical ring resonators, and have demonstrated high detection resolution and sensitivity capability [91, 92, 93, 94, 95]. In addition, on-chip ring resonators have potential for mass production, and are compatible with other photonic devices for on-chip integration [96].

Interferometer-based sensors associate the phase variation of the propagating optical mode with the RI variation. The phase variation is a result of the variation of the effective index of the optical mode in the sensing waveguide. Interferometer-based sensors can be implemented with surface plasmon interferometers [97]. As mentioned above, the SPPs are tightly bound to the surface between the metal and the dielectric. In addition to apertures in metal films and metal nanoparticles, MZI with SPP waveguides have also demonstrated their great potential in biochemical sensing applications both theoretically and experimentally [97, 98].

Photonic crystal (PhC) sensors are a promising direction for on-chip sensing of the RI. Photonic crystals are composed of periodic refractive indices that alter the motion of photons in the same way that a semiconductor crystal affects the electron motion. Photonic crystals therefore support photonic band structures which are very similar to the electronic energy bands in semiconductors. In sensing applications, the characteristics of the photonic crystal band gap are shifted as a result of RI variations. In addition, the photonic crystal fiber is a convenient and low cost tool which enables remote sensing. On the other hand, the localized mode of

a photonic crystal microcavity exhibits an extremely small active sensing volume, which may be a great optical alternative to implement small volume detection in future chip-scale photonics [99].

5.2 Slow-Light Enhanced Plasmonic Waveguide Sensors

Integrated optical devices for biochemical sensing could provide high sensitivity, small size, and dense integration. In particular, planar guided-wave sensors, based on Mach-Zehnder interferometers, directional couplers, and microring resonators, are able to measure small refractive index changes of analyte, and are becoming popular as label-free biomolecule sensors [97, 100, 101]. While dielectric waveguides lead to wavelength-scale sensors, plasmonic waveguides could enable miniaturized sensors with subwavelength length scales, due to the ability of such waveguides to confine and manipulate light at the nanoscale. In this chapter, I investigate nanoscale plasmonic sensors enhanced by slow-light effects.

I consider a Mach-Zehnder interferometer, implemented with plasmonic waveguiding structures, which is used as a refractive index sensor (Fig. 5.1(a)). Fluidic channels overlap with the sensing and reference arms of the MZI. The fluid to be sensed flows over the sensing arm, while a reference fluid flows over the reference arm. The sensing fluidic channel and the plasmonic waveguide structure in the sensing arm overlap in the sensing region. The length and width of the sensing region are L_S and W_S, respectively.

The modes of the plasmonic waveguides in the sensing and reference arms are excited by an optical source such as a laser (Fig. 5.1(a)). The output power, which is the only measurable quantity in such a MZI structure, is collected by a photodetector, and is given by

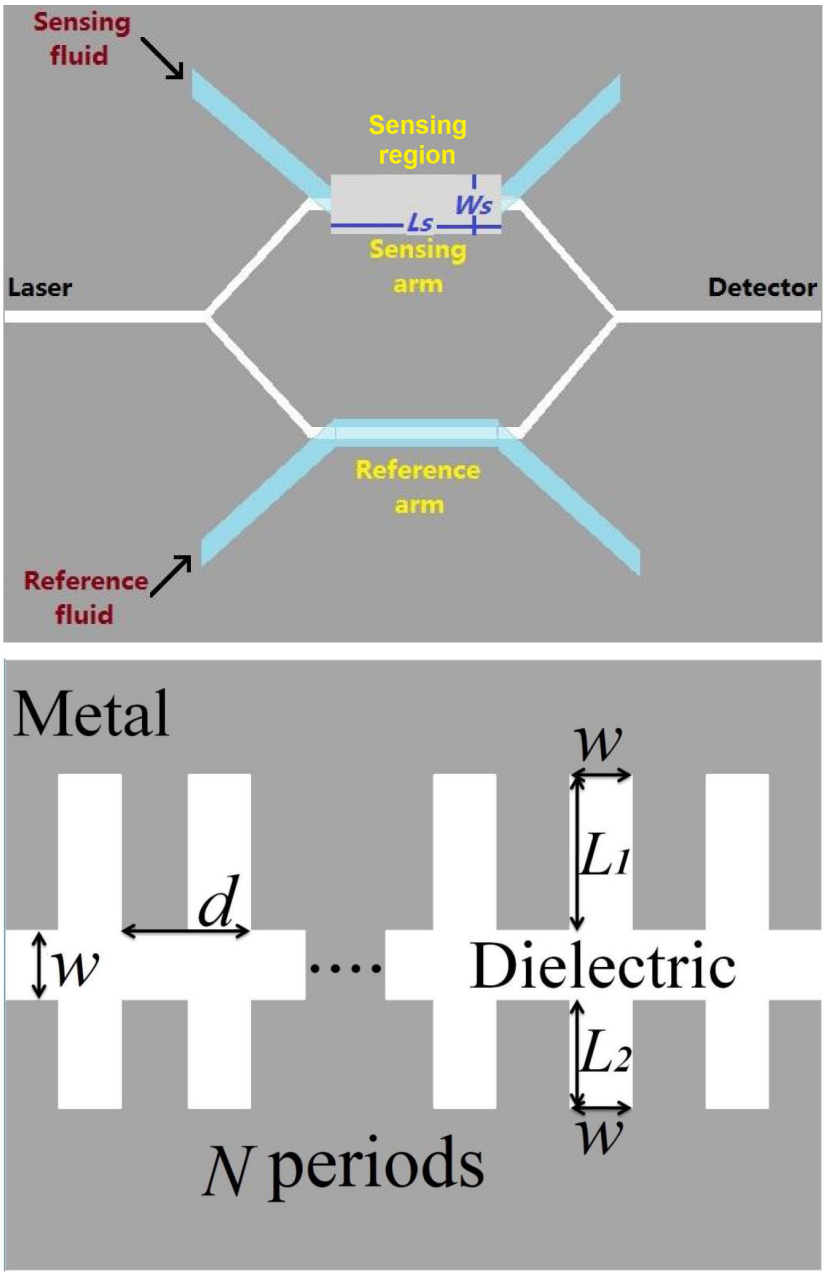

FIGURE 5.1. (a) Schematic of a Mach-Zehnder interferometer (MZI) used as a refractive index sensor. Fluidic channels overlap with the sensing and reference arms of the MZI. The fluid to be sensed flows over the sensing arm, while a reference fluid flows over the reference arm. The sensing fluidic channel and the plasmonic waveguide structure in the sensing arm overlap in the sensing region. The length and width of the sensing region are L_S and W_S, respectively. (b) Schematic of the plasmonic waveguide system used in the sensing region of the MZI sensor. It consists of a periodic array of two MDM stub resonators side-coupled to a MDM waveguide. N periods of the structure are included in the sensing region of the sensor.

$$P_{out}(n) = P_{in}\Big|\frac{1}{2}e^{-[A(n)+jB(n)]} + \frac{1}{2}e^{-(A_0+jB_0)}\Big|^2, \tag{5.1}$$

where n is the refractive index of the biological or chemical analyte in the sensing arm, $e^{-A(n)}$ and e^{-A_0} is the attenuation of the optical mode field in the sensing and reference arms, respectively, while $B(n)$ and B_0 is the insertion phase of the sensing and reference arms, respectively. If I define

$$F(n) \equiv \frac{1}{2}e^{-[A(n)+jB(n)]} + \frac{1}{2}e^{-(A_0+jB_0)}, \tag{5.2}$$

equation (5.1) simplifies to

$$P_{out}(n) = P_{in}\big|F(n)\big|^2. \tag{5.3}$$

The MZI refractive index sensitivity is then given by

$$\frac{\partial P_{out}(n)}{\partial n} = P_{in}\frac{\partial[F(n)F^*(n)]}{\partial n} = P_{in}\{\frac{\partial F(n)}{\partial n}F^*(n) + \frac{\partial F^*(n)}{\partial n}F(n)\}. \tag{5.4}$$

Choosing the attenuation of the sensing and reference arms to be equal results in maximum MZI visibility for such a structure [102]. In addition, choosing the difference between the sensing and reference arms insertion phases to be an odd multiple of $\frac{\pi}{2}$ results in maximum refractive index sensitivity [102]. The reference arm attenuation e^{-A_0} and insertion phase B_0 are therefore chosen so that in the absence of analyte ($n = n_0$), I have $e^{-A(n)} = e^{-A_0}$, and $B(n_0) = B_0 \pm m\frac{\pi}{2}$ where $m = 1, 3, 5,...$ Using equation (5.2), I find that

$$\frac{\partial P_{out}(n)}{\partial n}\Big|_{n=n_0} = \frac{1}{2}P_{in}e^{-2A_0}(\frac{\partial A}{\partial n}\Big|_{n=n_0} \mp \frac{\partial B}{\partial n}\Big|_{n=n_0}). \tag{5.5}$$

To characterize the sensing capability of the proposed MZI refractive index sensors, I define the following figure of merit (FOM) in terms of the relative change in the output power that occurs for a change in the refractive index [103, 104]

$$FOM \equiv \frac{1}{P_{in}}\frac{\partial P_{out}(n)}{\partial n}\Big|_{n=n_0} = \frac{1}{2}e^{-2A_0}(\frac{\partial A}{\partial n}\Big|_{n=n_0} \mp \frac{\partial B}{\partial n}\Big|_{n=n_0}). \tag{5.6}$$

The FOM can also be written as

$$FOM = T \cdot S, \tag{5.7}$$

where $T \equiv e^{-2A_0}$ is the power transmission through each of the sensor arms in the absence of analyte, and $S \equiv \frac{1}{2}(\frac{\partial A}{\partial n}\big|_{n=n_0} \mp \frac{\partial B}{\partial n}\big|_{n=n_0})$ is a factor associated with the sensitivity of $A(n)$ and $B(n)$ to refractive index variations. T and S will heretofore be referred to as the *transmission coefficient* and *sensitivity coefficient*, respectively, of the MZI sensor.

5.3 MDM Waveguide in the Sensing Arm

I first consider the case where the plasmonic waveguiding structure used in the sensing arm of the MZI sensor is a conventional MDM plasmonic waveguide [102]. The metal and the dielectric are assumed to be silver and water, respectively. I consider a deep subwavelength sensing region with length L_s=200nm. In Fig. 5.2, I show the FOM for such a structure as a function of the width of the MDM waveguide w, calculated using FDFD and Eq. (5.6). I observe that the FOM increases as the width of the waveguide w decreases. As w decreases, the group velocity of the optical mode supported by the waveguide decreases [80]. The sensitivity of the effective index of the mode to variations of the refractive index of the dielectric therefore increases [69]. Thus, the sensitivity coefficient S of the MZI sensor increases as the waveguide width w decreases. On the other hand, the propagation length of the optical mode decreases as w decreases [80]. Thus, the transmission coefficient T of the sensor decreases as the waveguide width w decreases. However, the increase in the sensitivity coefficient S dominates the decrease in the transmission coefficient T of the sensor, so that overall the FOM increases as the waveguide width w of the MDM plasmonic waveguide decreases.

Note that, if one considers the flow conditions of the carrier fluid as well as the size of the target biochemical analyte molecules, the practical lower limit for the MDM waveguide width is $w \sim 20$nm [102]. Thus, the maximum FOM when a conventional MDM plasmonic waveguide is used in the sensing region is ~ 0.7.

Also note that when a translationally invariant waveguide such as the conventional MDM plasmonic waveguide is used in the sensing region of the MZI sensor we have $A = \alpha L_s$ and $B = \beta L_s$, where α and $\beta = 2\frac{\pi}{\lambda_0} n_{eff}$ are the real and imaginary parts, respectively, of the propagation constant of the fundamental MDM waveguide mode. In addition, for the range of parameters considered here, I can neglect the sensitivity $\frac{\partial \alpha}{\partial n}$ so that Eq. (5.6) reduces to [102]

$$FOM = \mp \frac{1}{2} L e^{-2\alpha L} \frac{2\pi}{\lambda_0} \frac{\partial n_{eff,s}}{\partial n}\Big|_{n=n_0}. \tag{5.8}$$

In Fig. 5.2, I also show the FOM calculated with the approximation of Eq. (5.8)

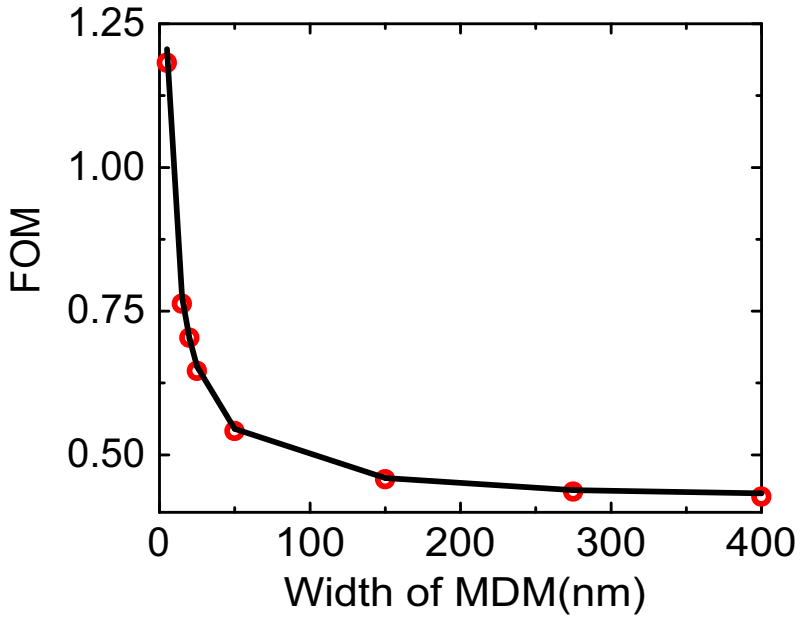

FIGURE 5.2. Figure of merit $FOM \equiv \frac{1}{P_{in}} \frac{\partial P_{out}(n)}{\partial n}$ of a MZI refractive index sensor implemented with MDM plasmonic waveguides as a function of the width w of the waveguides. Results are calculated for a sensing region length $L_S = 200$nm at $f = 194$THz using FDFD (circles), and the analytical approximation of Eq. (5.8) (solid line). The metal and dielectric are assumed to be silver and water, respectively.

and I observe that it is in excellent agreement with the FOM calculated using FDFD.

5.4 Plasmonic Analogue of EIT Waveguide in the Sensing Arm

I now consider the case where the plasmonic waveguiding structure used in the sensing arm of the MZI sensor is a slow-light waveguide based on a plasmonic analogue of EIT (Chapter 4). More specifically, the plasmonic waveguide system used in the sensing region consists of a periodic array of two MDM stub resonators side-coupled to a MDM waveguide (Fig. 5.1(b)). This system for brevity will heretofore be referred to as a plasmonic EIT system. N periods of the structure are included in the sensing region. I first consider a MZI sensor in which a single period of the plasmonic EIT system is included in the sensing region (N=1). The transmission spectra of such a structure feature a transparency peak centered at a frequency which is tunable through the length $L_1 + L_2 + w$ of the composite cavity formed by the two stub resonators (Chapter 4). Here I choose $L_1 + L_2 + w$=400nm, so that the transparency peak is centered at the operating frequency of f=194THz ($\lambda_0 = 1.55\mu$m). In addition, as before, I consider a sensing region with length $L_s = 200$nm. In Figs. 5.3(a) and 5.3(b), I show the transmission coefficient T, and the sensitivity coefficient S, respectively, for such a MZI sensor as a function of the stub resonator length L_1. As L_1 increases, L_2 decreases, since $L_1 + L_2 + w$ is fixed. Thus, the stub lengths difference $\Delta L = L_1 - L_2$ decreases, and therefore the frequency spacing between the stub resonances $\Delta\omega$ decreases. As a result, the transmission coefficient T, which corresponds to the transparency peak, decreases due to the metallic loss (Chapter 4). On the other hand, as ΔL decreases, the slowdown factor increases (Chapter 4). Thus, the sensitivity coefficient S increases

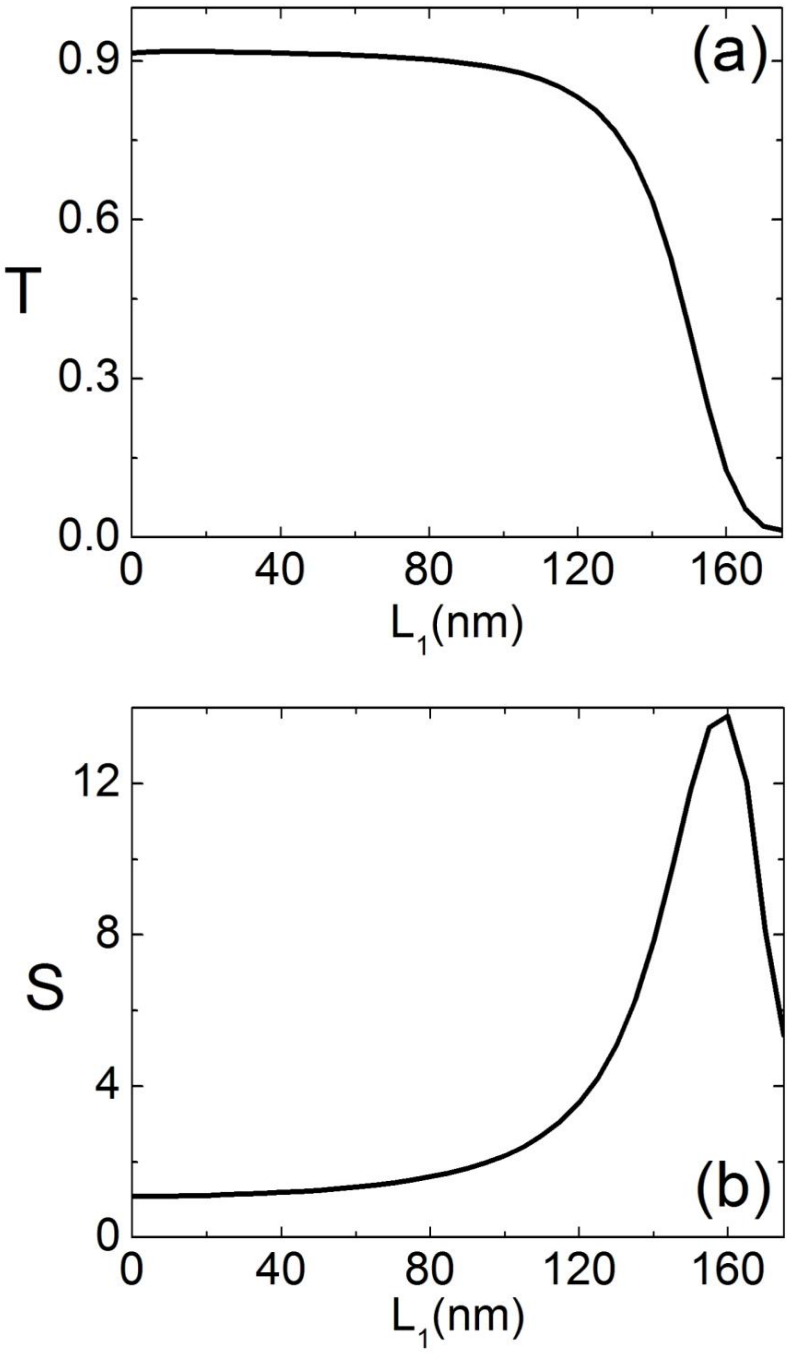

FIGURE 5.3. (a) Transmission coefficient T for a MZI refractive index sensor in which the sensing region consists of a plasmonic waveguide system as in Fig. 5.1(b) with $N = 1$ and $w = 50$nm as a function of the stub resonator length L_1. Results are calculated for a sensing region length $L_S = 200$nm, and width $W_S = L_1 + L_2 + w = 400$nm. All other parameters are as in Fig. 5.2. (b) Sensitivity S as a function of the stub resonator length L_1. All other parameters are as in (a).

for $L_1 < 160$nm. I note that if $L_1 > 160$nm, I have $L_2 < 190$nm so that ΔL and therefore $\Delta\omega$ become very small. In this regime I found out that the slowdown factor actually decreases, so that the sensitivity coefficient S also decreases, as L_1 increases (Fig. 5.3(b)). In Fig. 5.4, I show the FOM calculated using FDFD

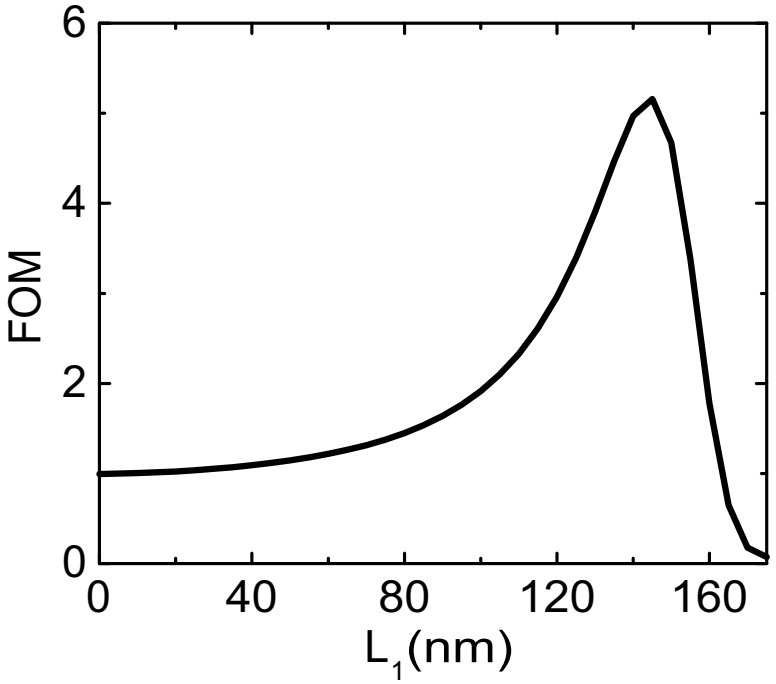

FIGURE 5.4. Figure of merit $FOM \equiv \frac{1}{P_{in}} \frac{\partial P_{out}(n)}{\partial n}$ of a MZI refractive index sensor, in which the sensing region consists of a plasmonic waveguide system as in Fig. 5.1(b), as a function of the stub resonator length L_1. All other parameters are as in Fig. 5.3(a).

and equation (5.6) for the MZI sensor in which a single period of the plasmonic EIT system is included in the sensing region (N=1). The FOM is a product of the transmission coefficient T, and the sensitivity coefficient S [equation (5.8)]. For $L_1 < 160$nm there is a trade-off between T which decreases, and S which increases, as L_1 increases (Figs. 5.3(a), 5.3(b)). For small L_1 the increase in S dominates the decrease in T, so that the FOM increases, as L_1 increases. However, for larger L_1 the decrease in T becomes significant, and the FOM eventually decreases (Fig. 5.4). The maximum FOM of ~ 5.2 is obtained for $L_1 \sim$145nm. I next consider a MZI sensor in which two periods of the plasmonic EIT system are

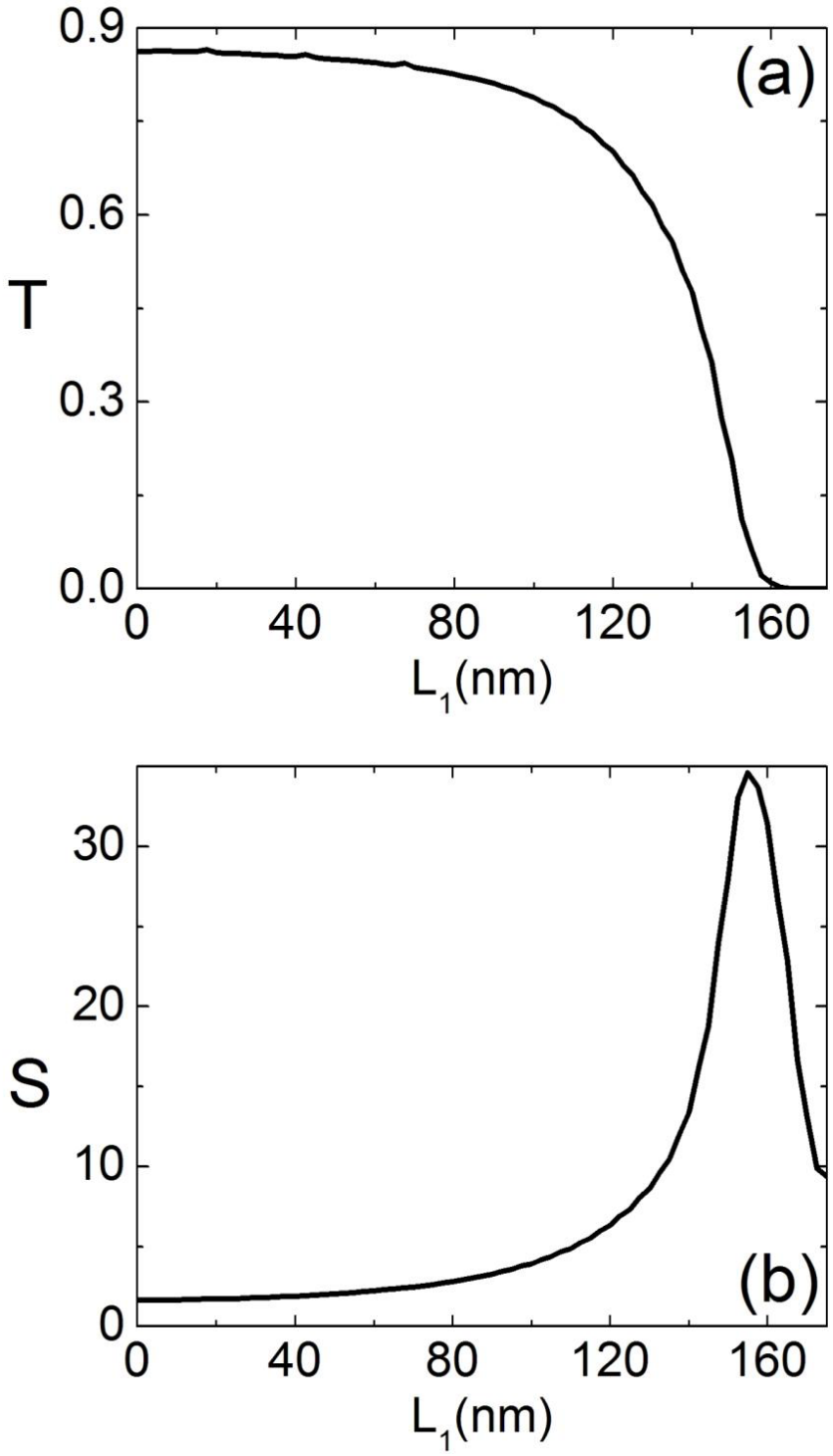

FIGURE 5.5. (a) Transmission coefficient T for a MZI refractive index sensor in which the sensing region consists of a plasmonic waveguide system as in Fig. 5.1(b) with $N = 2$ as a function of the stub resonator length L_1. All other parameters are as in Fig. 5.3(a). (b) Sensitivity S as a function of the stub resonator length L_1. All other parameters are as in (a).

included in the sensing region (N=2). In Figs. 5.5(a), 5.5(b), and 5.6, I show the transmission coefficient T, the sensitivity coefficient S, and the FOM, respectively, for such a MZI sensor as a function of the stub resonator length L_1. I observe that the dependence of T, S, and FOM on L_1 is very similar to the single period case (Figs. 5.3(a), 5.3(b), and 5.4). For a given L_1, increasing the number of periods N of the plasmonic EIT system, increases both the attenuation and the insertion phase of the optical mode propagating through the structure. Thus, the transmission coefficient T decreases, while the sensitivity coefficient S increases, as the number of periods N increases (Figs. 5.3, 5.5). The maximum FOM of ~ 6.9 for the N=2 case is obtained for $L_1 \sim 145$nm (Fig. 5.6). I observe that for deep subwavelength

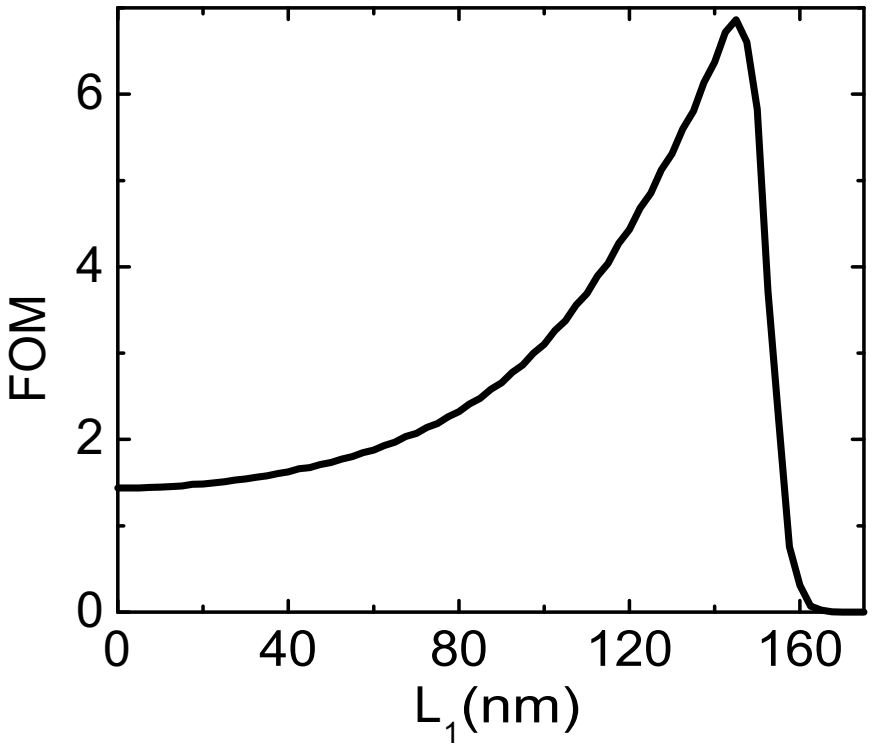

FIGURE 5.6. Figure of merit $FOM \equiv \frac{1}{P_{in}} \frac{\partial P_{out}(n)}{\partial n}$ of a MZI refractive index sensor, in which the sensing region consists of a plasmonic waveguide system as in Fig. 5.1(b) with $N = 2$, as a function of the stub resonator length L_1. All other parameters are as in Fig. 5.4(a).

sensing regions (L_s=200nm), using the plasmonic EIT system in the sensing arm

of the MZI sensor results in significantly larger FOM, compared to a sensor in which a conventional MDM waveguide is used in the sensing arm. As mentioned above, a MZI sensor using the plasmonic EIT system results in a maximum FOM of ~ 5.2 and ~ 6.9 for N=1 and N=2, respectively, while the maximum FOM for a MZI sensor using a conventional MDM waveguide is ~ 0.7. In other words, a MZI sensor using the plasmonic EIT system leads to approximately an order of magnitude enhancement in the FOM, and therefore in the minimum detectable refractive index change, compared to a MZI sensor using a conventional MDM waveguide. I found that further increasing the number of periods N of the plas-

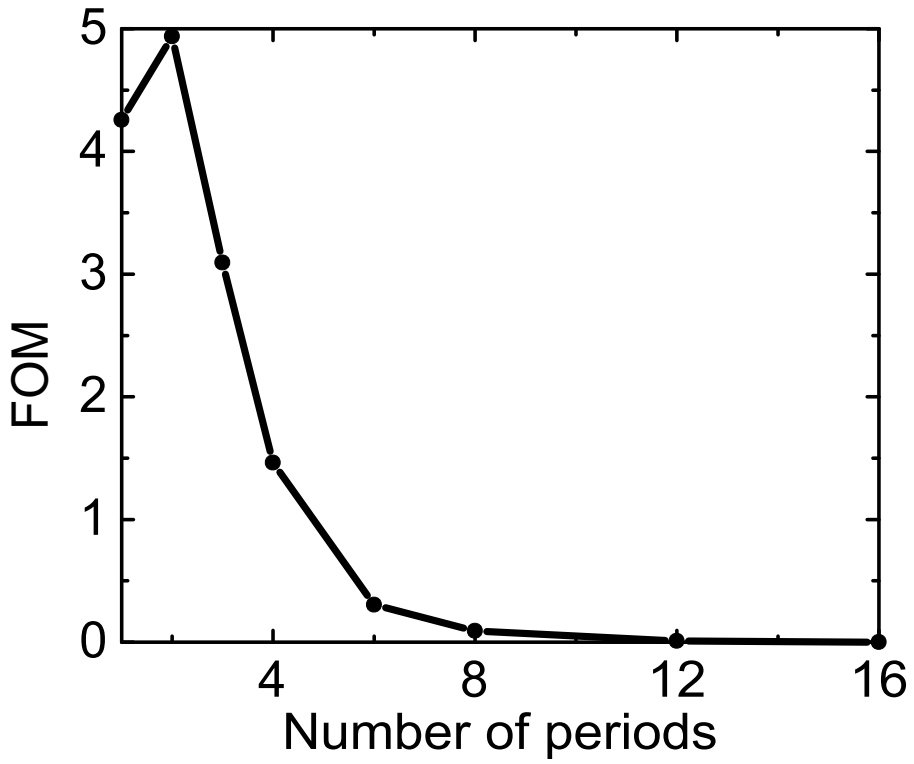

FIGURE 5.7. Figure of merit $FOM \equiv \frac{1}{P_{in}} \frac{\partial P_{out}(n)}{\partial n}$ of a MZI refractive index sensor, in which the sensing region consists of a plasmonic waveguide system as in Fig. 5.1(b), as a function of the number of periods N. All other parameters are as in Fig. 5.4(a).

monic EIT system in the sensing region of the MZI sensor decreases the FOM of the sensor (Fig. 5.7). This is due to the fact that when lossy waveguides are used in

the arms of a MZI sensor the optimum length of the sensing region is equal to the propagation length of the optical mode in the waveguides [102]. For the plasmonic EIT system considered here, when $N>2$ the length of the structure exceeds the propagation length of the supported optical mode, and the corresponding FOM therefore decreases. Finally, in Fig. 5.8, I show the FOM of the MZI sensor based

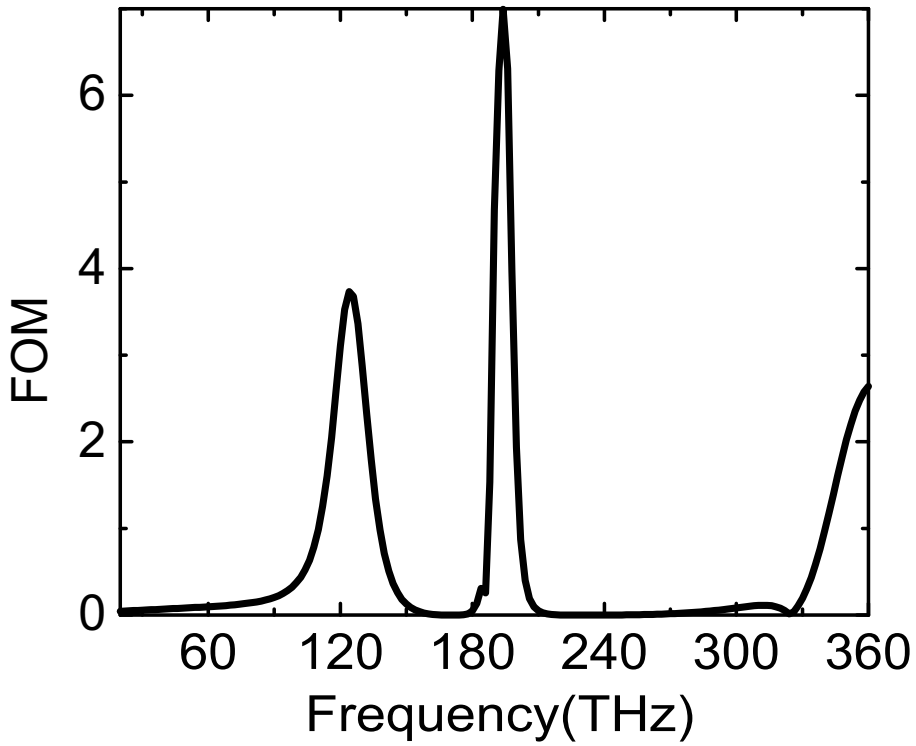

FIGURE 5.8. Figure of merit $FOM \equiv \frac{1}{P_{in}} \frac{\partial P_{out}(n)}{\partial n}$ of a MZI refractive index sensor, in which the sensing region consists of a plasmonic waveguide system as in Fig. 5.1(b), as a function of frequency. Results are shown for $L_1 = 145$nm. All other parameters are as in Fig. 5.6(a).

on the plasmonic EIT system for $N=2$ as a function of frequency. I observe that, as expected, the FOM of the sensor exhibits a peak at $f=194$ THz, which coincides with the transparency peak in the transmission spectra of the plasmonic EIT system. In addition, the FOM also exhibits a peak at $f=124$ THz. I found that this peak in the FOM is also associated with a peak in the transmission spectra of the plasmonic EIT system for $N=2$. The magnetic field profiles associated with

the transmission spectra peaks at f=124 THz and f=194 THz are shown in Figs. 5.9(a), and 5.9(b), respectively.

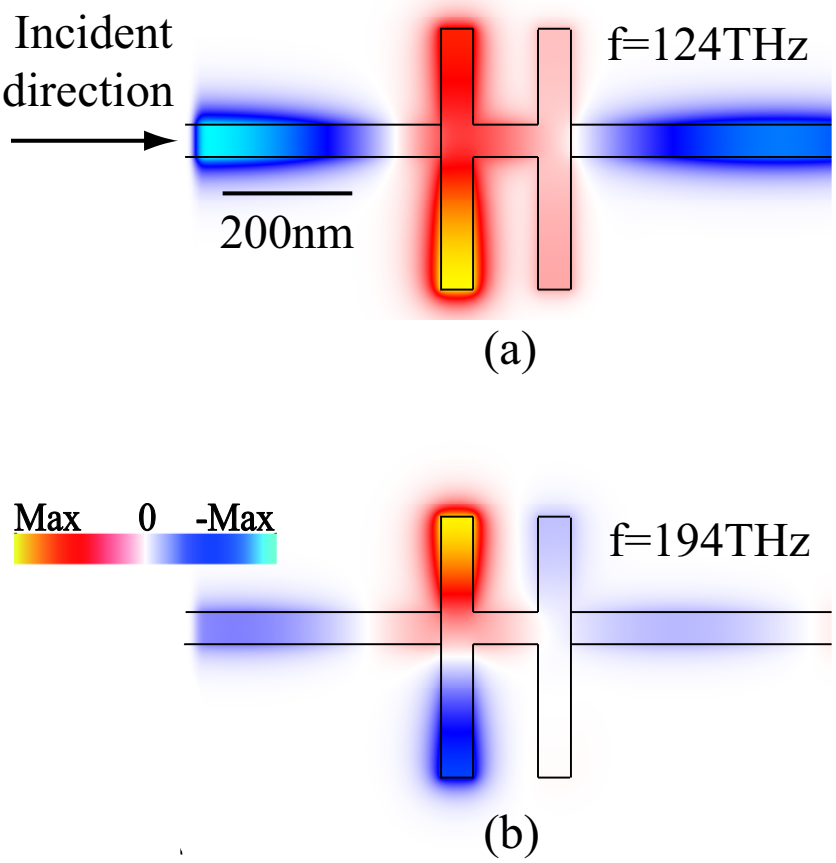

FIGURE 5.9. (a) Magnetic field profile for the structure of Fig. 5.8 at $f = 124$ THz when the fundamental TM mode of the MDM waveguide is incident from the left. (b) Same as in (a) except that $f = 194$ THz.

5.5 Conclusions

In conclusion, I considered Mach-Zehnder interferometer sensors in which the sensing arm consists of a slow-light waveguide based on a plasmonic analogue of EIT. I showed that a MZI sensor using such a waveguide leads to approximately an order

of magnitude enhancement in the refractive index sensitivity, and therefore in the minimum detectable refractive index change, compared to a MZI sensor using a conventional MDM waveguide.

Chapter 6

Compact Slit-based Couplers for Metal-Dielectric-Metal Plasmonic Waveguides

6.1 Introduction to Couplers for Plasmonic Waveguides

As discussed in Chapter 1, plasmonic waveguides have shown the potential to guide subwavelength optical modes, the so-called surface plasmon polaritons, at metal-dielectric interfaces. Several different nanoscale plasmonic waveguiding structures have been proposed, such as metallic nanowires, metallic nanoparticle arrays, V-shaped grooves, and MDM waveguides [9, 10, 13, 105, 106, 107, 108, 109]. Among these, MDM plasmonic waveguides, which are the optical analogue of microwave two-conductor transmission lines [110], are of particular interest because they support modes with deep subwavelength scale over a very wide range of frequencies extending from DC to visible [7]. Thus, MDM waveguides could provide an interface between conventional optics and subwavelength electronic and optoelectronic devices.

For applications involving MDM plasmonic waveguides, it is essential to develop compact structures to couple light efficiently into such waveguides [36]. Several different couplers between MDM and dielectric waveguides have been investigated both theoretically and experimentally[36, 37, 38, 39, 40, 41]. In addition, structures for coupling free space radiation into MDM waveguides have also been investigated. In particular, Preiner *et al.* [42] investigated subwavelength diffraction gratings as coupling structures into MDM waveguide modes. However, in diffraction grating structures several grating periods are required for efficient waveguide mode excitation, so that such structures need to be several microns long when designed to

operate at frequencies around the optical communication wavelength (λ_0 =1.55 μm). In addition, in several experimental investigations of MDM waveguides and devices, a single slit was used to couple light from free space into MDM plasmonic waveguides [15, 43, 44, 45, 46]. While single slit coupling structures are more compact, slit-based coupler designs have not been investigated in detail.

In this chapter, I investigate compact wavelength-scale slit-based structures for coupling free space light into MDM plasmonic waveguides. I show that for a single slit structure the coupling efficiency is limited by a trade-off between the light power coupled into the slit, and the transmission of the slit-MDM waveguide junction. I next consider a two-section slit structure, and show that for such a structure the upper slit section enhances the coupling of the incident light into the lower slit section, by improving the impedance matching between the incident plane wave and the lower slit mode. The optimized two-section slit structure results in ~ 2.3 times enhancement of the coupling into the MDM plasmonic waveguide compared to the optimized single-slit structure. I then consider a symmetric double-slit structure. I show that for such a structure the surface plasmons excited at the metal-air interfaces are partially coupled into the slits, and thus the coupling of the incident light into the slits is greatly enhanced. The optimized double-slit structure results in ~ 3.3 times coupling enhancement compared to the optimized single-slit structure. Finally, I show that, while all incoupling structures are optimized at a single wavelength, the operation wavelength range for high coupling efficiency is broad.

The remainder of this Chapter is organized as follows. In Section 6.2, I first define the transmission cross section of the MDM plasmonic waveguide for a given coupling structure, and describe the simulation method used for the analysis of the couplers. The results obtained for the single slit, two-section slit, and double slit

coupling structures are presented in Sections 6.3, 6.4, and 6.5, respectively. Finally, our conclusions are summarized in Section 6.6.

6.2 Simulation Method

I consider a silver-silica-silver MDM plasmonic waveguide in which the upper metal layer has a finite thickness (Fig. 6.1). The minimum thickness of this metal layer is chosen to be 150nm. For such a thickness, the field profile and wave vector of the fundamental TM mode supported by such a waveguide at optical frequencies are essentially identical to the ones of a MDM plasmonic waveguide with semi-infinite metal layers. I consider compact structures for incoupling a normally incident plane wave from free space into the fundamental mode of the silver-silica-silver MDM plasmonic waveguide. In all cases, the total width of the incoupling structure is limited to less than 1.1μm, which approximately corresponds to one wavelength in silica ($\lambda_s = \lambda_0/n_s$, where n_s =1.44), when operating at the optical communication wavelength (λ_0 =1.55μm).

Due to the symmetry of all coupling structures considered in this paper, the same amount of power couples into the left and right propagating silver-silica-silver MDM waveguide modes. In other words, half of the total incoupled power couples into each of the left and right propagating MDM waveguide modes. For comparison of different incoupling configurations, I define the *transmission cross section* σ_T of the silver-silica-silver MDM waveguide as the total light power coupled into the right propagating fundamental TM mode of the waveguide, normalized by the incident plane wave power flux density [36]. In two dimensions, the transmission cross section is in the unit of length.

I use a two-dimensional FDFD method (Chapter 2) [111, 112] to numerically calculate the transmission in the MDM plasmonic waveguide. This method allows us to directly use experimental data for the frequency-dependent dielectric constant of metals such as silver [36, 51], including both the real and imaginary parts, with no approximation. PML absorbing boundary conditions are used at all boundaries of the simulation domain [56]. I also use the total-field-scattered-field formulation to simulate the response of the structure to a normally incident plane wave input (Chapter 3) [52].

6.3 Single Slit Coupler

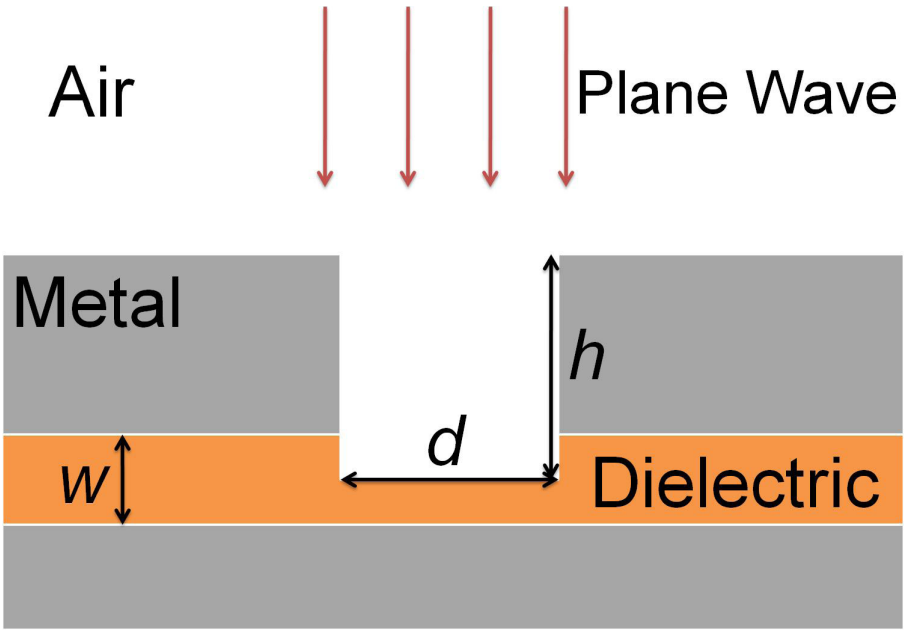

FIGURE 6.1. Schematic of a structure consisting of a single slit for incoupling a normally incident plane wave from free space into the fundamental mode of a MDM plasmonic waveguide.

I first consider a structure consisting of a single slit for incoupling a normally incident plane wave from free space into the fundamental mode of the silver-silica-silver MDM plasmonic waveguide with dielectric core thickness w. The slit extends

half way into the dielectric core of the MDM waveguide (Fig. 6.1). In Fig. 6.2, I

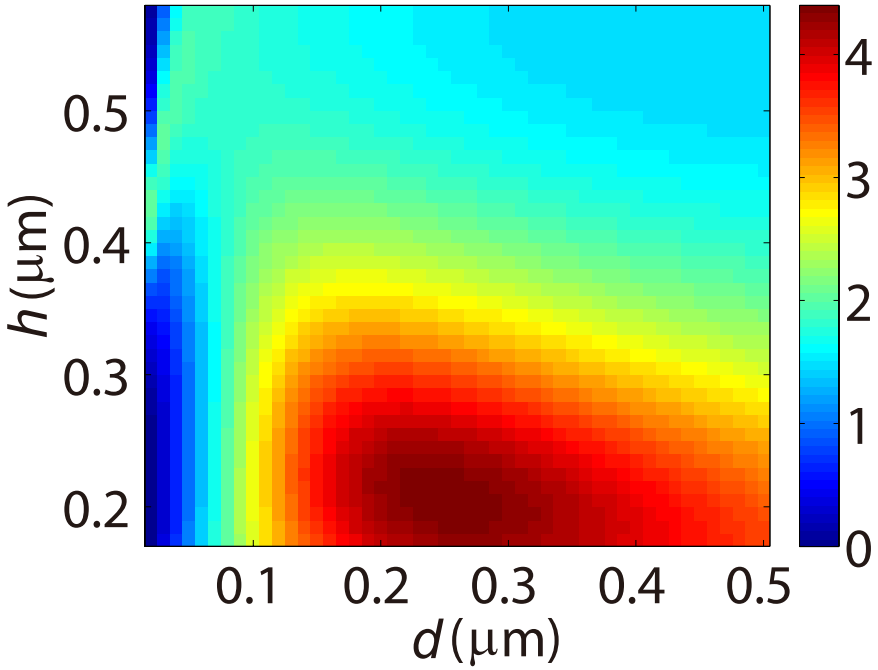

FIGURE 6.2. Transmission cross section σ_T of the MDM plasmonic waveguide in units of w for the structure of Fig. 6.1 as a function of the slit width d and length h calculated using FDFD. Results are shown for a silver-silica-silver structure with w = 50nm at λ_0 =1.55μm.

show the transmission cross section σ_T of the silver-silica-silver MDM waveguide in units of w for the single slit structure of Fig. 6.1 as a function of the width d and length h of the slit. For the range of parameters shown, I observe one transmission peak. The maximum cross section of $\sigma_T \sim 4.67w$ is obtained for such an incoupling structure at d = 250nm and h = 205nm (Fig. 6.2). Both the silver-silica-silver MDM waveguide and the silver-air-silver slit have subwavelength widths, so that only the fundamental TM mode is propagating in them. Thus, I can use single-mode scattering matrix theory to account for the behavior of the system [87]. I use FDFD to numerically extract the transmission cross section σ_{T_1} of a silver-air-silver MDM waveguide with air core thickness d (Fig. 6.3(a)). I also use FDFD to extract the complex magnetic field reflection coefficient r_1 and transmission

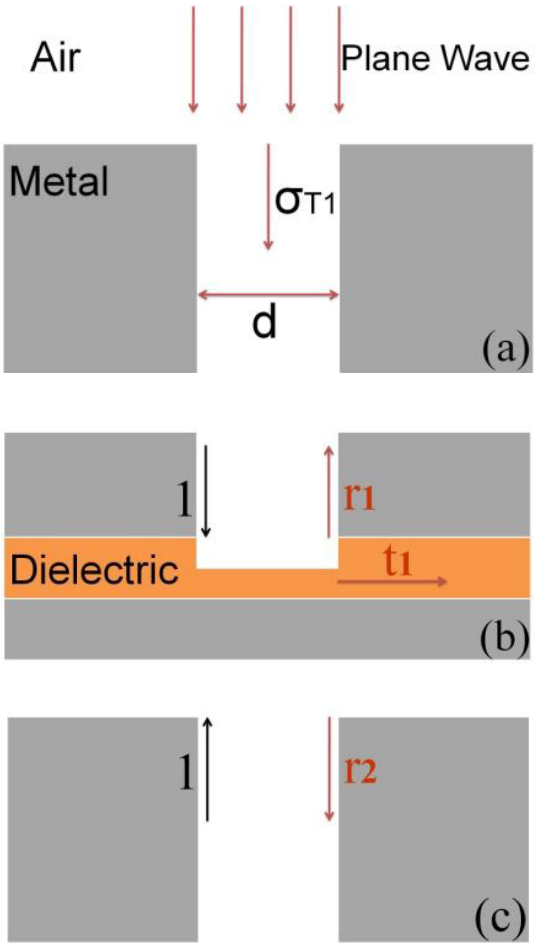

FIGURE 6.3. (a) Schematic defining the transmission cross section σ_{T_1} of a semi-infinite MDM waveguide when a plane wave is normally incident on it. (b) Schematic defining the reflection coefficient r_1, and transmission coefficient t_1 when the fundamental TM mode of a metal-air-metal waveguide is incident at the junction with a metal-dielectric-metal waveguide. (c) Schematic defining the reflection coefficient r_2 of the fundamental TM mode of a MDM waveguide at the waveguide/air interface.

coefficient t_1 of the fundamental mode of a silver-air-silver MDM waveguide at the T-shaped junction with a silver-silica-silver MDM waveguide (Fig. 6.3(b)), as well as the reflection coefficient r_2 at the interface between the silver-air-silver MDM waveguide and air (Fig. 6.3(c)). The transmission cross section σ_T of the silver-silica-silver MDM waveguide for the single slit structure of Fig. 6.1 can then be calculated using scattering matrix theory as [87]:

$$\sigma_T = \sigma_{T_1} \eta_{\mathrm{res}_1} T_{\mathrm{splitter}}, \tag{6.1}$$

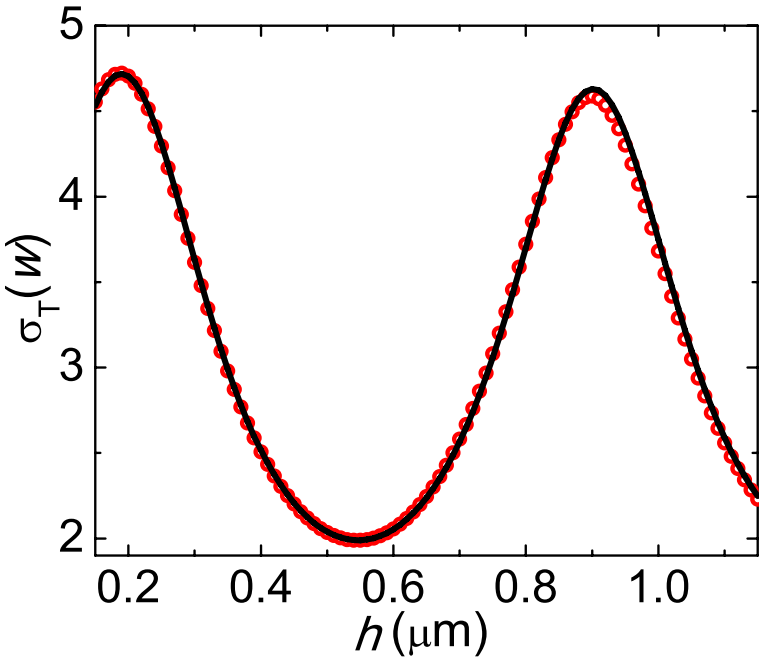

FIGURE 6.4. Transmission cross section σ_T for the structure of Fig. 6.1 as a function of the slit length h calculated using FDFD (red circles) and scattering matrix theory (black solid line). Results are shown for $d = 220$nm. All other parameters are as in Fig. 6.2.

where $T_{\text{splitter}}=|t_1|^2$ is the power transmission coefficient of the T-shaped junction of Fig. 6.3(b), $\eta_{\text{res}_1} = |\frac{\exp(-\gamma_1 h)}{1-r_1 r_2 \exp(-2\gamma_1 h)}|^2$ is the resonance enhancement factor associated with the silver-air-silver slit resonance, and $\gamma_1 = \alpha_1 + i\beta_1$ is the complex wave vector of the fundamental propagating TM mode in a silver-air-silver MDM waveguide with air core thickness d. [Equation (6.1) is proved in Appendix C]. I note that η_{res_1} is a function of the reflection coefficients r_1 and r_2 at both sides of the silver-air-silver slit. I also observe that the resonance enhancement factor η_{res_1} exhibits a maximum when the slit Fabry-Pérot resonance condition $\arg(r_1) + \arg(r_2) - 2\beta_1 h = -2m\pi$ is satisfied, where m is a integer. Thus, for a given silver-air-silver slit width d, the transmission cross section σ_T of the silver-silica-silver MDM waveguide is maximized for slit lengths h which satisfy the above Fabry-Pérot resonance condition.

In Fig. 6.4, I show the transmission cross section σ_T of the silver-silica-silver MDM waveguide for the single slit structure of Fig. 6.1 as a function of the slit length h calculated using FDFD. Results are shown for $d = 250$nm, which is the optimum slit width as mentioned above. I observe that, as the slit length h increases, the transmission cross section σ_T exhibits peaks, corresponding to the Fabry-Pérot resonances in the slit. The maximum transmission cross section σ_T of $\sim 4.67w$ is obtained at the first peak ($h = 205$nm) associated with the first Fabry-Pérot resonance in the slit. In Fig. 6.4, I also show σ_T calculated using scattering matrix theory (Eq. (6.1)). I observe that there is excellent agreement between the scattering matrix theory results and the exact results obtained using FDFD.

For the optimized single slit structure ($d = 250$nm, $h = 205$nm), the transmission cross section σ_{T_1} of the corresponding silver-air-silver MDM waveguide with air core thickness $d = 250$nm (Fig. 6.3(a)) is $\sim 7.71w = 385.5$nm (Table 6.1). In other words, the silver-air-silver subwavelength MDM waveguide collects light from an area significantly larger than its geometric cross-sectional area [36]. In addition, for the optimized single slit structure the power transmission coefficient of the T-shaped junction is T_{splitter} ~0.37, and the resonance enhancement factor is η_{res_1} ~1.64 (Table 6.1). Thus, $\sim 2 \times 37 = 74\%$ of the incident power at the junction is transmitted to the left and right propagating modes of the silver-silica-silver MDM waveguide.

In Fig. 6.5, I show the transmission cross section σ_{T_1} of a silver-air-silver MDM waveguide (Fig. 6.3(a)) as a function of the waveguide air core thickness d. I observe that, as expected, σ_{T_1} increases monotonically as the thickness d increases. In other words, the light power collected by the waveguide increases as the air core thickness of the waveguide increases. On the other hand, the properties of the T-shaped junction (Fig. 6.3(b)) can be described using the concept of characteristic

TABLE 6.1. Transmission cross sections $\sigma_{T_{1/2}}$ and σ_T in units of w, power transmission coefficient of the T-shaped junction T_{splitter}, and resonance enhancement factors $\eta_{\text{res}_{1/2}}$ calculated using scattering matrix theory. Results are shown for the optimized single slit, two-section slit, and double-slit structures of Figs. 6.1, 6.7, and 6.9, respectively.

	Single slit	Two-section slit	Double-slit
$\sigma_{T_{1/2}}(w)$	7.71	12.33	18.49
T_{splitter}	0.37	0.28	0.41
$\eta_{\text{res}_{1/2}}$	1.64	3.11	2.02
$\sigma_T(w)$	4.67	10.75	15.29

impedance and transmission line theory [13, 110, 113]. Based on transmission line theory, the structure is equivalent to the junction of three transmission lines. The load connected to the input transmission line at the junction consists of the series combination of the two output transmission lines. The characteristic impedances of the input and output transmission lines are $Z_1 = \frac{\gamma_1}{j\omega\epsilon_0}d$ and $Z_2 = \frac{\gamma_2}{j\omega\epsilon}w$, respectively, where $\gamma_2 = \alpha_2 + i\beta_2$ is the complex wave vector of the fundamental propagating TM mode in a silver-silica-silver MDM waveguide with dielectric core thickness w, and ϵ is the dielectric permittivity of silica [13, 84]. Thus, the equivalent load impedance is $Z_L = 2Z_2$, and the maximum transmission coefficient T_{splitter} is obtained when the impedance matching condition $Z_1 = Z_L = 2Z_2$ is satisfied. The transmission coefficient T_{splitter} of the T-shaped junction (Fig. 6.3(b)) therefore does not increase monotonically with d. As a result, the coupling efficiency of the single slit structure is limited by a trade-off between the power incident at the slit-MDM waveguide junction, and the transmission coefficient T_{splitter} of the T-shaped junction. More specifically, the width of the optimized single slit is $d = 250$nm, as mentioned above. If the slit width d decreased, the impedance matching between the silver-air-silver MDM input waveguide and the two silver-silica-silver MDM output waveguides would improve, and T_{splitter} therefore would increase. However, if d decreased, the transmission cross section σ_{T_1} of the silver-

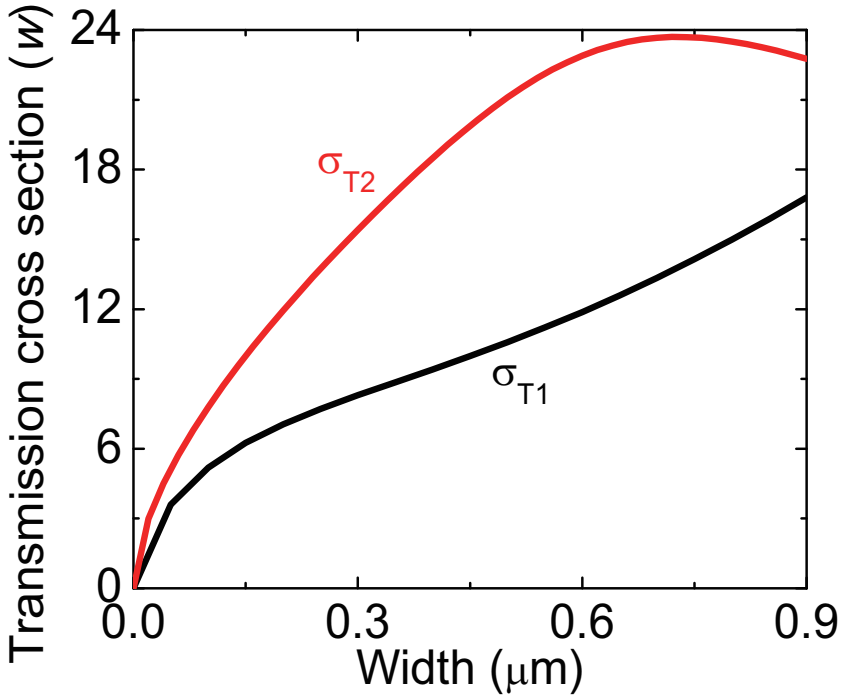

FIGURE 6.5. Transmission cross sections (in units of $w = 50$nm) of a single silver-air-silver MDM waveguide σ_{T_1} (Fig. 6.3(a)), and of a double silver-air-silver MDM waveguide σ_{T_2} (Fig. 6.11(a)), as a function of their total air core thickness (d for the single and $2d$ for the double waveguide). The total width of the double waveguide is $2d + D = 1.1\mu$m.

air-silver MDM waveguide would decrease (Fig. 6.5). In addition, the reflectivity $|r_1|^2$ at the bottom side of the slit, and therefore the resonance enhancement factor η_{res_1} would also decrease. Thus, the power incident at the junction between the slit and the silver-silica-silver MDM waveguide would decrease.

In Fig. 6.6, I show the magnetic field profile for the structure of Fig. 6.1 when the slit dimensions are optimized for maximum transmission cross section σ_T. I observe that, since the transmission cross section of the silver-silica-silver MDM waveguide $\sigma_T \sim 4.67w$ is larger than its geometrical cross-section w, the field in the MDM waveguide is enhanced with respect to the incident plane wave field. I find that the maximum magnetic field amplitude enhancement in the silver-silica-silver waveguide with respect to the incident plane wave is ∼2.4 (Fig. 6.6).

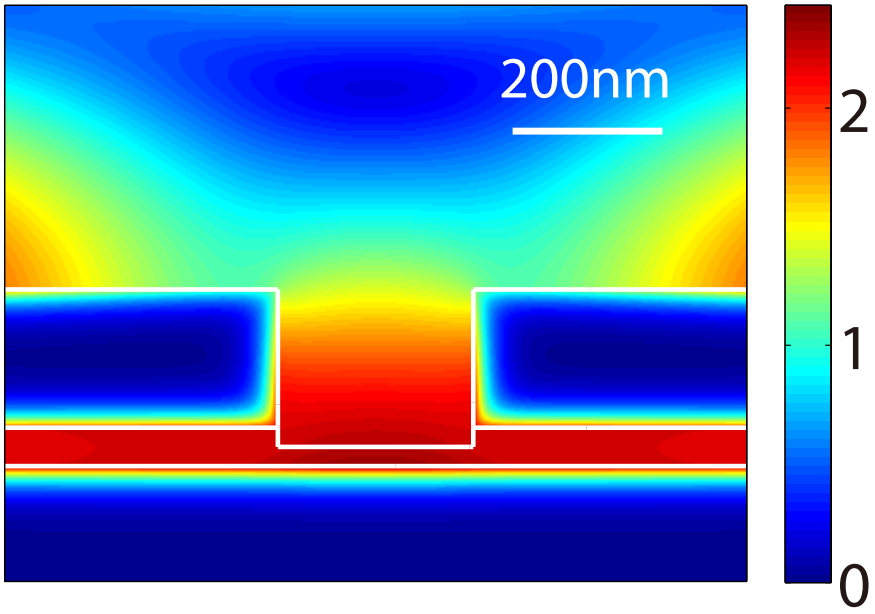

FIGURE 6.6. Transmission cross section σ_T for the structure of Fig. 6.1 as a function of the slit length h calculated using FDFD (red circles) and scattering matrix theory (black solid line). Results are shown for $d = 220$nm. All other parameters are as in Fig. 6.2.

6.4 Two-Section Slit Coupler

To enhance the transmission cross section σ_T of the silver-silica-silver MDM plasmonic waveguide, I next consider a structure consisting of a two-section slit for incoupling light into the waveguide (Fig. 6.7). The lengths h_1, h_2 and widths d_1, d_2 of these slit sections are optimized using a genetic global optimization algorithm in combination with FDFD [36, 114] to maximize the transmission cross section σ_T of the silver-silica-silver MDM waveguide. As before, the width of the incoupling structure is limited to less than 1.1μm. Using this approach, the maximum transmission cross section of the silver-silica-silver MDM waveguide for such a two-section slit structure is found to be $\sigma_T \sim 10.75w$ (Table 6.1) for $d_1 = 410$nm, $d_2 = 1100$nm, $h_1 = 230$nm, and $h_2 = 540$nm. I observe that for such a structure the transmission cross section of the corresponding silver-air-silver MDM waveguide (with air core thickness d_1) is $\sigma_{T_1} \sim 12.33w$ (Table 6.1), which is $\sim$1.6 times larger compared to the optimized single slit coupler. In other words, the upper slit

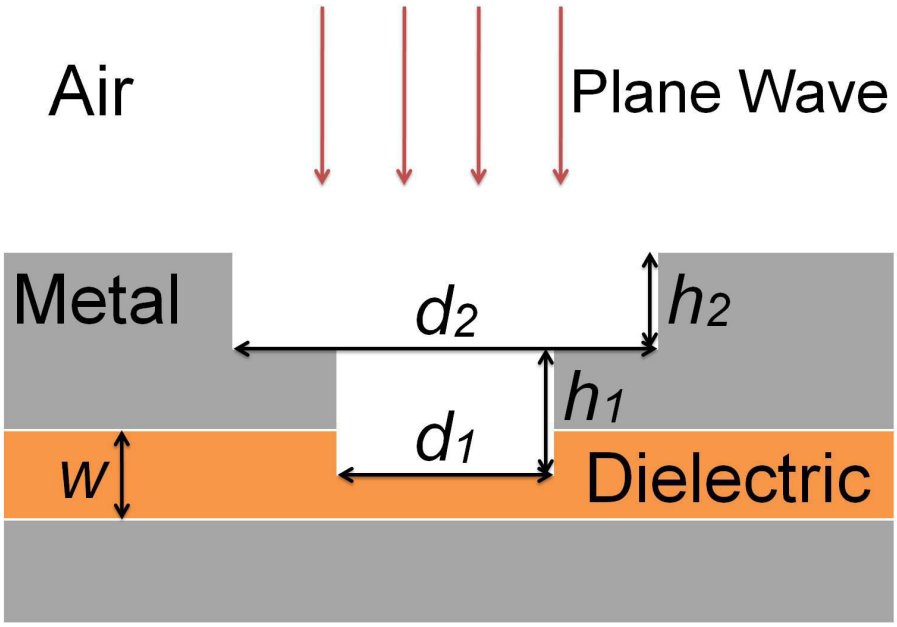

FIGURE 6.7. Schematic of a structure consisting of a two-section slit for incoupling a normally incident plane wave from free space into the fundamental mode of a MDM plasmonic waveguide.

section can enhance the coupling of the incident plane wave into the lower slit section, by improving the impedance matching between the incident plane wave and the lower slit mode [115] . In addition, the resonance enhancement factor of the optimized two-section slit structure is $\eta_{\text{res}_1} \sim 3.11$ (Table 1), which is ∼1.9 times larger compared to the optimized single slit coupler. I found that the increase in the resonance enhancement factor η_{res_1} of this two-section slit structure is due to larger reflectivities $|r_1|^2$ and $|r_2|^2$ at both sides of the lower slit section compared to the optimized single slit coupler. On the other hand, the transmission coefficient of the T-shaped junction for the optimized two-section slit structure of Fig. 6.7 is $T_{\text{splitter}} \sim 0.28$ (Table 6.1), which is ∼1.3 times smaller than the one of the optimized single slit structure. This is due to larger mismatch between the characteristic impedance of the input waveguide Z_1 and the load impedance Z_L=2Z_2 at the T-shaped junction. Thus, overall the use of an optimized two-section slit coupler (Fig. 6.7) results in $1.6 \times 1.9/1.3 \simeq 2.3$ times larger transmission cross section

σ_T of the silver-silica-silver MDM waveguide compared to the single-slit coupler case (Fig. 6.1). In Fig. 6.8, I show the magnetic field profile for the structure of

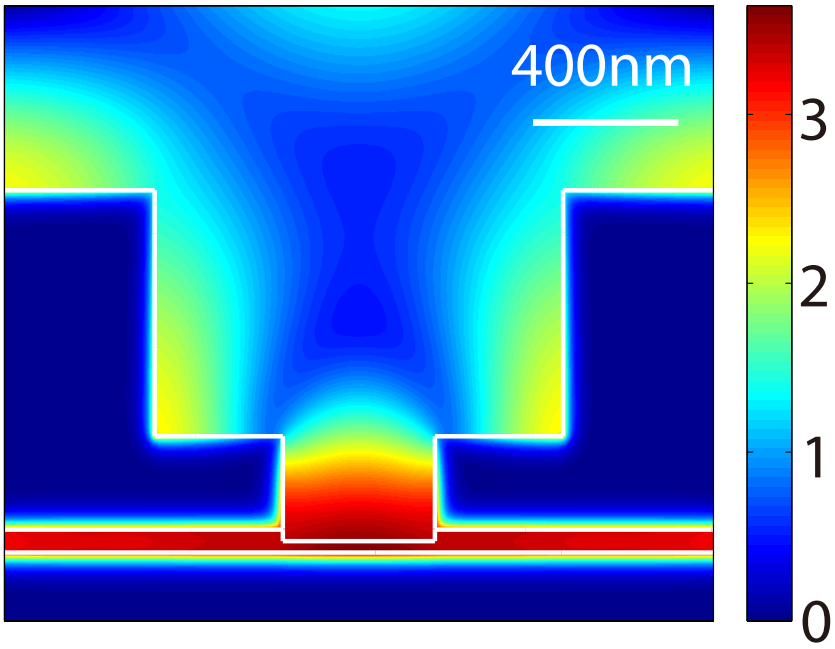

FIGURE 6.8. Profile of the magnetic field amplitude for the optimized structure of Fig. 6.7 with $d_1 = 410$nm, $d_2 = 1100$nm, $h_1 = 230$nm, and $h_2 = 540$nm, normalized with respect to the field amplitude of the incident plane wave. All other parameters are as in Fig. 6.2.

Fig. 6.7 with dimensions optimized for maximum transmission cross section σ_T of the silver-silica-silver MDM waveguide. The field in the narrower lower slit section is stronger than the field in the upper slit section. The maximum magnetic field amplitude enhancement in the silver-silica-silver MDM waveguide with respect to the incident plane wave is ~ 3.6 (Fig. 6.8).

6.5 Double-Slit Coupler

To further enhance the transmission cross section σ_T of the silver-silica-silver MDM plasmonic waveguide, I consider a symmetric double-slit structure for incoupling light into the waveguide (Fig. 6.9). As before, the total width $2d+D$ of the structure

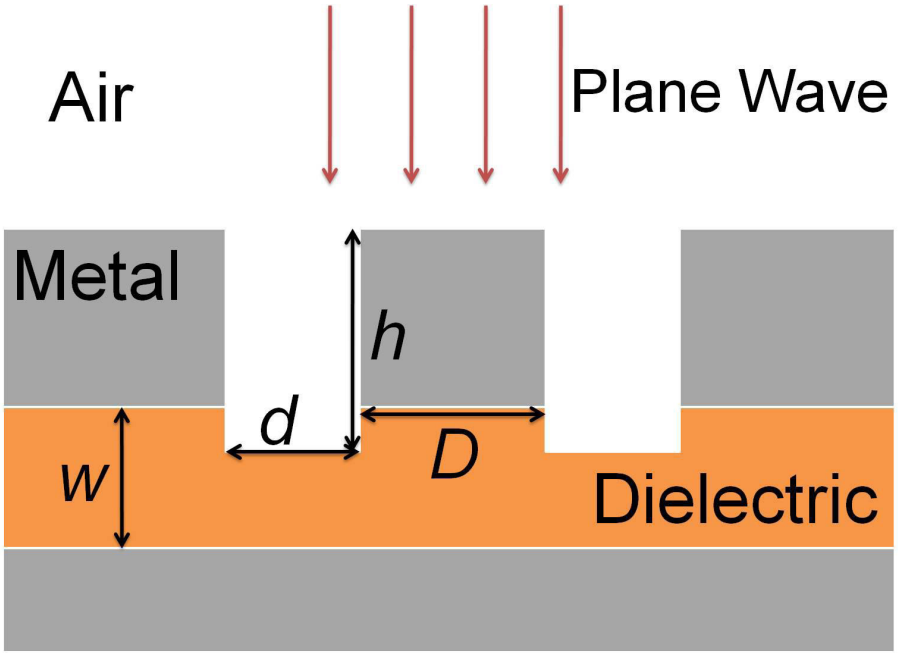

FIGURE 6.9. Schematic of a double-slit structure for incoupling a normally incident plane wave from free space into the fundamental mode of a MDM plasmonic waveguide.

is limited to less than 1.1μm. For such a double-slit coupling structure I found that, if $2d + D \leq 1.1\mu$m, the maximum transmission cross section σ_T is obtained when $2d + D = 1.1\mu$m. In the following I therefore set $2d + D = 1.1\mu m$. In Fig. 6.10, I show the transmission cross section σ_T of the silver-silica-silver MDM waveguide in units of w for the structure of Fig. 6.9 as a function of the width d and length h of the slits. For the range of parameters shown, I observe one transmission peak in the silver-silica-silver MDM waveguide. The maximum transmission cross section of $\sigma_T \sim 15.29w$ is obtained for such an incoupling structure at $d = 200$nm ($D = 700$nm) and $h = 250$nm. I also note that for $d \sim 400$nm ($D \sim 300$nm) the transmission into the silver-silica-silver MDM waveguide is almost zero (Fig. 6.10). I found that this is due to the fact that for a slit distance of $D \sim 300$nm the incident light strongly couples into the silver-silica-silver waveguide resonator between the slits. In addition, there is almost no light coupled into the left and right propagating modes of the silver-silica-silver MDM waveguide, due to destructive

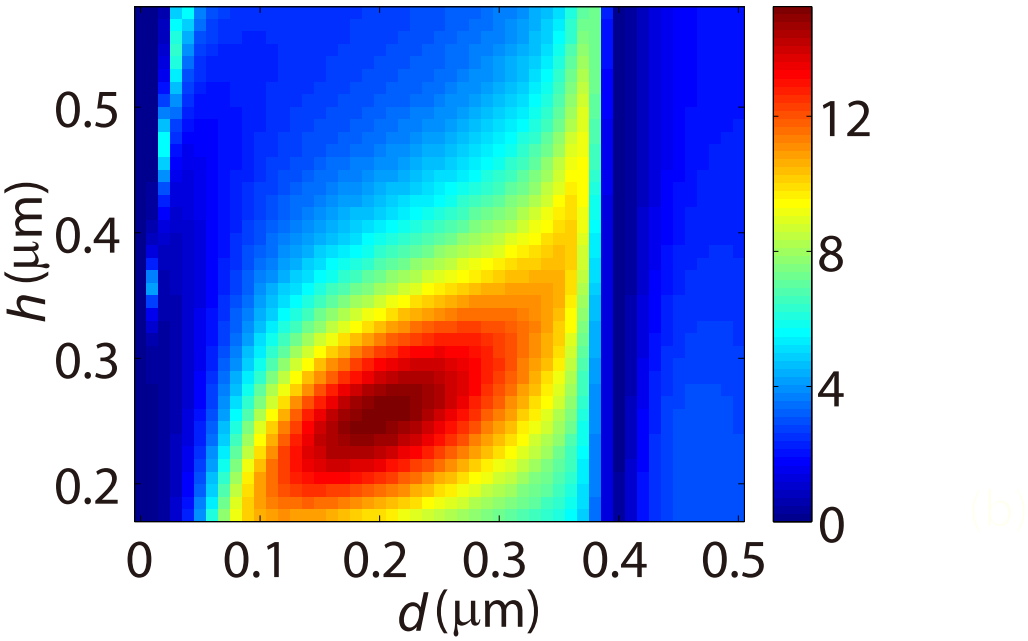

FIGURE 6.10. Transmission cross section σ_T of the MDM plasmonic waveguide in units of w for the structure of Fig. 6.9 as a function of the slit width d and length h calculated using FDFD. The total width of the incoupling structure is $2d + D = 1.1\mu$m. All other parameters are as in Fig. 6.2.

interference between the wave directly coupled through the slit, and the wave coupled through the silver-silica-silver waveguide resonator. I use again single-mode scattering matrix theory to account for the behavior of the system. I use FDFD to numerically extract the transmission cross section σ_{T_2} of a double silver-air-silver MDM waveguide as in Fig. 6.11(a). I also use FDFD to extract the complex magnetic field reflection coefficient r_3 and transmission coefficients t_2, t_3 of the fundamental mode of a silver-silica-silver MDM waveguide at the T-shaped junction with a silver-air-silver MDM waveguide (Fig. 6.11(b)). Note that $t_1 = t_2$ due to reciprocity [110]. Finally, I also extract the reflection coefficient r_4 at the interface between the silver-air-silver MDM waveguide and air, and the transmission coefficient t_4 into the other MDM waveguide, for the double MDM waveguide structure (Fig. 6.11(c)). The transmission cross section σ_T of the silver-silica-silver MDM plasmonic waveguide for the double-slit coupling structure of

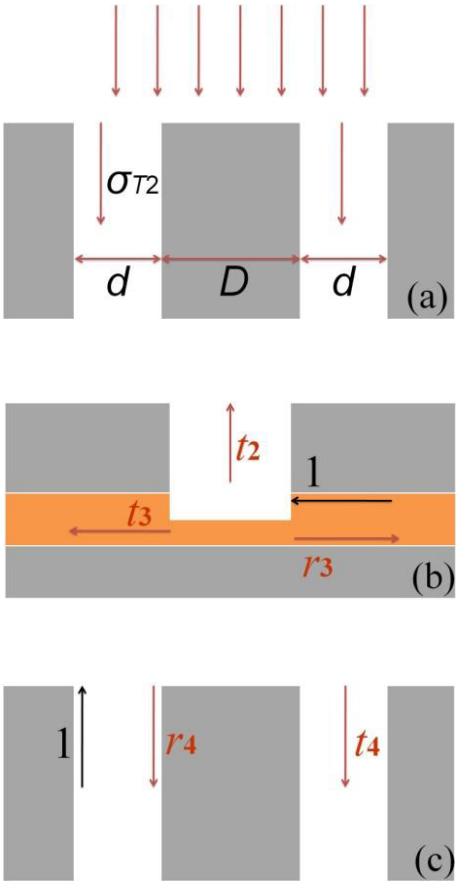

FIGURE 6.11. (a) Schematic defining the transmission cross section σ_{T_2} of two semi-infinite MDM waveguides when a plane wave is normally incident on them. (b) Schematic defining the reflection coefficient r_3, and transmission coefficients t_2, t_3 when the fundamental TM mode of a metal-dielectric-metal waveguide is incident at the junction with a metal-air-metal waveguide. (c) Schematic of a structure consisting of two semi-infinite MDM waveguides defining the reflection coefficient r_4 of the fundamental TM mode of one of the MDM waveguides at the waveguide/air interface, and the transmission coefficient t_4 into the other MDM waveguide.

Fig. 6.9 is then calculated using scattering matrix theory as:

$$\sigma_T = \sigma_{T_2} \eta_{\text{res}_2} T_{\text{splitter}}, \tag{6.2}$$

where $T_{\text{splitter}} = |t_1|^2 = |t_2|^2$ is the power transmission coefficient of the T-shaped junction, $\eta_{\text{res}_2} = |\frac{\exp(-\gamma_1 h)(1+t_3 A)}{1-(r_1+t_1 t_2 A)(r_4+t_4)\exp(-2\gamma_1 h)}|^2$ is the resonance enhancement factor associated with the complex resonator formed by the two silver-air-silver slits and the silver-silica-silver MDM waveguide resonator of length D between them, and $A = \frac{exp(-\gamma_2 D)+r_3 \exp(-2\gamma_2 D)}{1-r_3^2 \exp(-2\gamma_2 D)}$. [Equation (6.2) is proved in Appendix D]. Thus,

I observe that the resonant enhancement factor η_{res_2} for such a complex resonator is similar to that of a Fabry-Pérot resonator with effective reflectivities $r_{\text{eff}_1} = r_1 + t_1 t_2 A$ and $r_{\text{eff}_2} = r_4 + t_4$. In Fig. 6.12, I show the transmission cross

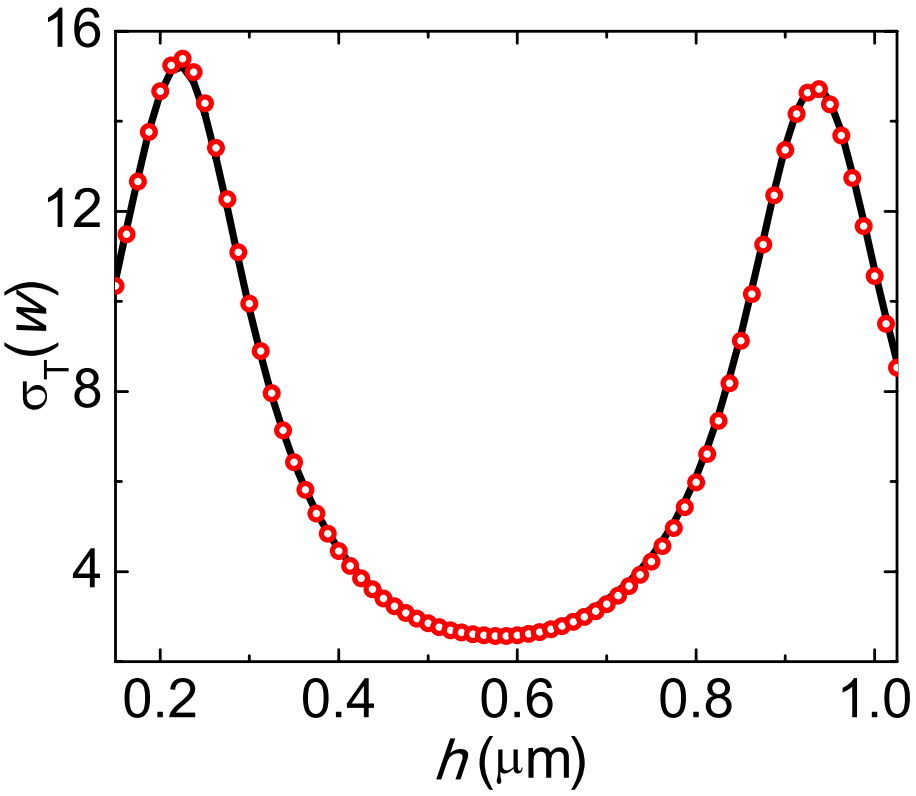

FIGURE 6.12. Transmission cross section σ_T for the structure of Fig. 6.9 as a function of the slit length h calculated using FDFD (red circles) and scattering matrix theory (black solid line). Results are shown for $d = 220$nm. All other parameters are as in Fig. 6.10.

section σ_T for the structure of Fig. 6.9 as a function of the slit length h calculated using FDFD. Results are shown for $d = 200$ nm, which is the optimum slit width as mentioned above. I observe that, as the slit length h increases, the transmission cross section σ_T exhibits peaks, associated with the resonances of the double-slit structure. The maximum transmission cross section σ_T of $\sim 15.29w$ is obtained at the first peak ($h = 250$nm) associated with the first resonant length of the slits. In Fig. 6.12, I also show σ_T calculated using scattering matrix theory (equation

(6.2)). I observe that there is excellent agreement between the scattering matrix theory results and the exact results obtained using FDFD.

I observe that for the optimized double-slit structure the transmission cross section of the corresponding double silver-air-silver MDM waveguide (Fig. 6.3(d)) is $\sigma_{T_2} \sim 18.49w$ (Table 6.1), which is ∼2.4 times larger compared to the transmission cross section $\sigma_{T_1} \sim 7.71w$ of the single silver-air-silver MDM waveguide corresponding to the optimized single slit coupler (Fig. 6.3(a)). In Fig. 6.5, I show the transmission cross sections of a single silver-air-silver MDM waveguide σ_{T_1} (Fig. 6.3(a)), and of a double silver-air-silver MDM waveguide σ_{T_2} (Fig. 6.11(a)) as a function of their total air core thickness (d for the single and $2d$ for the double waveguide). I observe that a double silver-air-silver MDM waveguide collects more light than a single silver-air-silver MDM waveguide with the same total air core thickness. This is due to the fact that, when a plane wave is incident on a semi-infinite MDM waveguide, surface plasmon waves are excited at the air-metal interfaces. In the double MDM waveguide structure (Fig. 6.11(a)), the power of these surface plasmon waves is partially coupled into the MDM waveguides, thus increasing the total light power collected by the structure. In addition, the resonance enhancement factor of the optimized double-slit structure $\eta_{\text{res}_2} \sim 2.02$ (Table 6.1) is slightly larger than the resonance enhancement factor of the optimized single slit coupler ($\eta_{\text{res}_1} \sim 1.64$). Overall, the use of an optimized double-slit coupler (Fig. 6.9) results in ∼ 3.3 times larger transmission cross section σ_T of the silver-silica-silver MDM waveguide compared to the optimized single-slit coupler case (Fig. 6.1). In Fig. 6.13, I show the magnetic field profile for the structure of Fig. 6.9 with dimensions optimized for maximum transmission cross section. The maximum magnetic field amplitude enhancement in the silver-silica-silver waveguide with respect to the incident plane wave is ∼ 4.2. The incoupling structures were

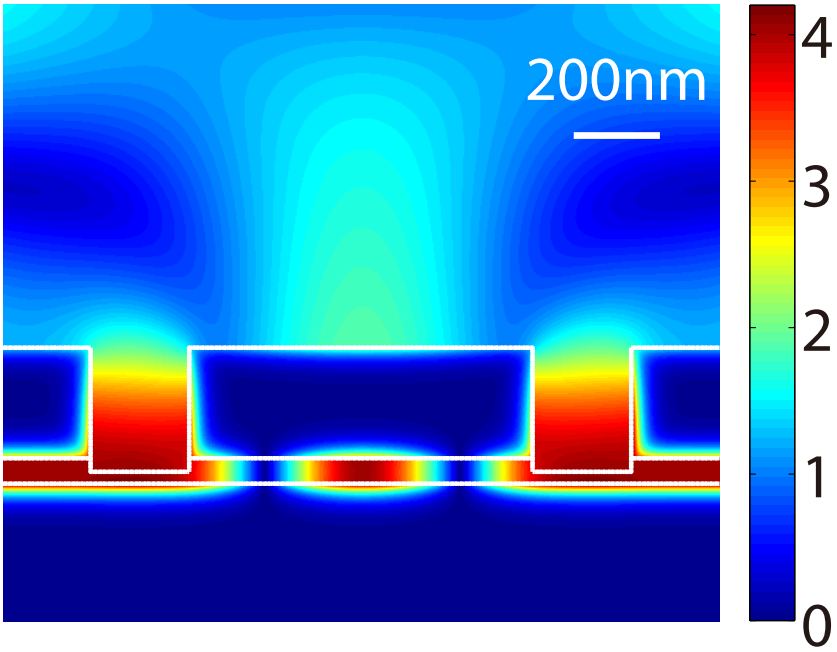

FIGURE 6.13. Profile of the magnetic field amplitude for the structure of Fig. 6.9 for $d = 200$nm and $h = 250$nm, normalized with respect to the field amplitude of the incident plane wave. All other parameters are as in Fig. 6.10.

all optimized at a single wavelength of λ_0 =1.55μm. In Fig. 6.14, I show the transmission cross section σ_T of the silver-silica-silver MDM plasmonic waveguide as a function of frequency for the optimized structures of Fig. 6.1 (single slit), Fig. 6.7 (two-section slit), and Fig. 6.9 (double slit). I observe that the operation frequency range for high transmission is broad. This is due to the fact that in all cases the enhanced transmission is not associated with any strong resonances. In other words, the quality factors Q of the slit coupling structures are low.

In Fig. 6.14, I also show the transmission cross section σ_T for the double-slit structure, if the metal in the MDM waveguide is lossless ($\epsilon_{\text{metal}} = Re(\epsilon_{\text{metal}})$, neglecting the imaginary part of the dielectric permittivity $Im(\epsilon_{\text{metal}})$). I observe that material losses in the metal do not significantly affect the transmission efficiency of the incoupling structures. This is due to the fact that the dimensions of the incoupling structures are much smaller than the propagation lengths of the fundamental TM modes in the silver-silica-silver and the silver-air-silver waveguides.

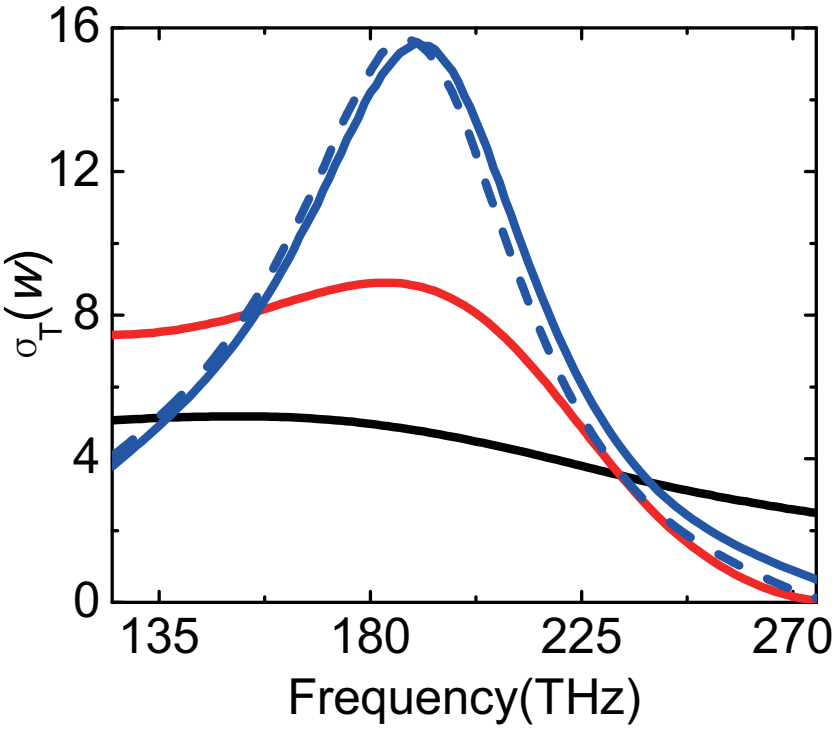

FIGURE 6.14. Transmission cross section σ_T spectra in units of w for the three optimized incoupling structures in Figs. 6.1 (single slit), 6.7 (two-section slit), and 6.9 (double slit). Results are shown for the structure of Fig. 6.1 with $d = 250$nm, $h = 205$nm (black line), for the structure of Fig. 6.7 with $d_1 = 410$nm, $d_2 = 1100$nm, $h_1 = 230$nm, and $h_2 = 540$nm (red line), and for the structure of Fig. 6.9 with $d = 200$nm, $h = 250$nm (blue line). Also shown are the transmission cross section σ_T spectra for the double-slit structure (Fig. 6.9), if the metal in the MDM waveguide is lossless (blue dashed line). All other parameters are as in Fig. 6.2.

I found that neither the coupling of the incident light into the silver-air-silver slits nor the coupling between the slits and the silver-silica-silver MDM plasmonic waveguide are significantly affected by material losses in the metal.

6.6 Conclusions

In this Chapter, I investigated compact slit-based structures for coupling free space light into silver-silica-silver MDM plasmonic waveguides. In all cases, the total width of the incoupling structure was limited to less than 1.1μm, which approximately corresponds to one wavelength in silica $\lambda_s = \lambda_0/n_s$, when operating at

λ_0 =1.55μm. I first considered a coupling structure consisting of a single slit extending half way into the dielectric core of the MDM waveguide. I found that the coupling efficiency of such a single slit structure is limited by a trade-off between the light power coupled into the slit, and the transmission of the slit-MDM waveguide T-shaped junction.

To enhance the coupling into the silver-silica-silver MDM plasmonic waveguide, I next considered a two-section slit structure. I found that for such a structure the upper slit section enhances the coupling of the incident light into the lower slit section, by improving the impedance matching between the incident plane wave and the lower slit mode. In addition, the use of the optimized two-section slit structure increases the reflectivities at both sides of the lower slit section, and therefore the resonance enhancement factor. On the other hand, the transmission of the T-shaped junction for the optimized two-section slit structure is smaller than the one of the optimized single slit structure. Overall, the use of an optimized two-section slit coupler resulted in $\sim$ 2.3 times enhancement of the coupling into the MDM plasmonic waveguide compared to the optimized single-slit coupler.

To further enhance the coupling into the silver-silica-silver MDM plasmonic waveguide, I considered a symmetric double-slit structure. I found that such a structure greatly enhances the coupling of the incident light into the slits. This is due to the fact that the incident light excites surface plasmons at the air-metal interfaces. In the case of a double-slit structure these plasmons are partially coupled into the slits, thus increasing the total light power collected by the structure. In addition, the resonance enhancement factor of the optimized double-slit coupler is slightly larger than the resonance enhancement factor of the optimized single slit coupler. Overall, the use of an optimized double-slit coupler resulted in $\sim$ 3.3 times enhancement of the coupling into the MDM plasmonic waveguide compared to the

optimized single-slit coupler. I also found that, while the incoupling structures were all optimized at a single wavelength, the operation wavelength range for high coupling efficiency is broad. As final remarks, for wavelength-scale slit-based struc-

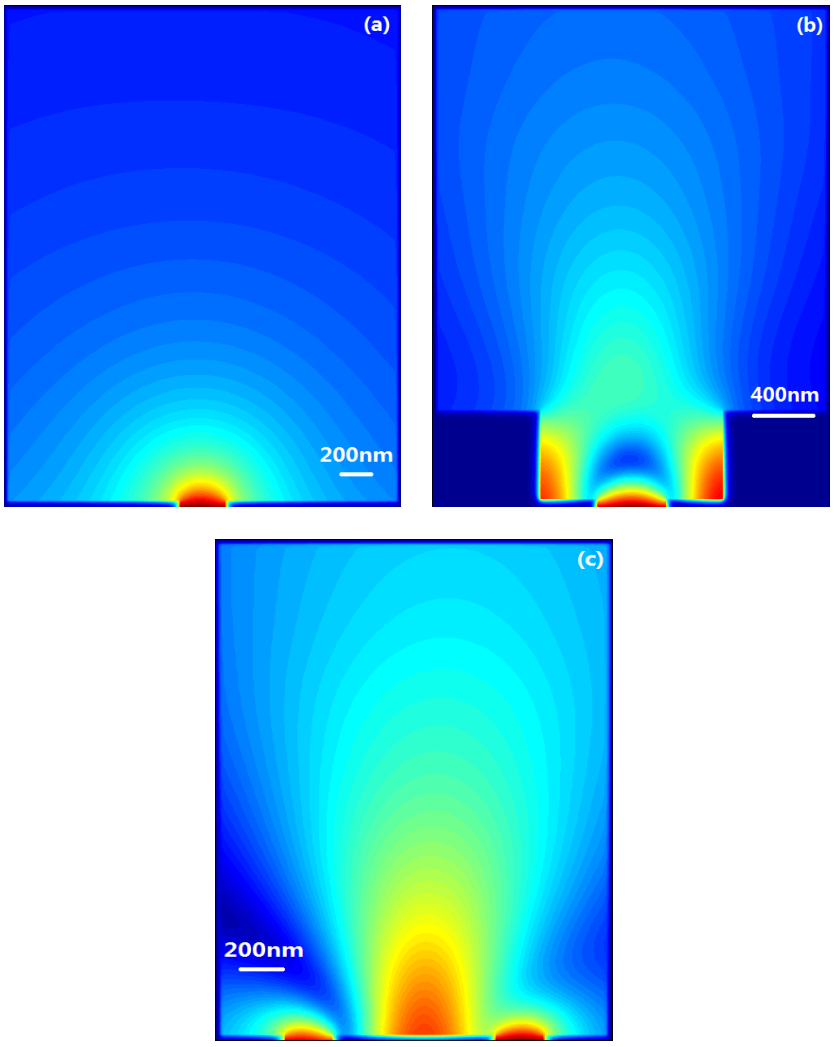

FIGURE 6.15. (a) Radiation pattern of the single slit structure, when this structure is used to couple light from the MDM plasmonic waveguide into free space. (b) Radiation pattern of the two-section slit structure. (c) Radiation pattern of the double-slit structure. In all cases I show the magnetic field amplitude profile above the slits. Results are shown for the three optimized incoupling structures in Figs. 6.1 (single slit), 6.7 (two–section slit), and 6.9 (double slit) for λ_0 =1.55μm. All other parameters are as in Fig. 6.14.

tures the double-slit structure results in optimal coupling performance. I verified that, if three or more slits are used in a wavelength-scale coupler, the performance

is always worse due to destructive interference between the waves coupled through the slits. Moreover, if a reflector is introduced in one of the two silver-silica-silver MDM ouput waveguides, then all the incoupled power will couple into the other silver-silica-silver MDM output waveguide. In addition, the proposed slit-based structures can also be used to couple light from a MDM plasmonic waveguide into free space. I found that, when the single slit structure is used to outcouple light, the radiation pattern of the structure is approximately isotropic [116] (Fig. 6.15(a)). On the other hand, I found that two-section slit and double-slit structures introduce anisotropy in the radiation pattern, with stronger radiation in the normal direction [116] (Fig. 6.15(b) and 6.15(c)). Finally, I note that there are some analogies between the proposed coupling structures and the slot antennas used in the microwave frequency range [117].

Chapter 7
Summary and Suggestions for Future Work

7.1 Summary of Results

I first introduced subwavelength slow-light waveguides for enhanced light-matter interaction, based on a plasmonic analogue of EIT. Such waveguides support a subwavelength slow-light mode, and exhibit a small group velocity dispersion. The waveguiding structure consists of a periodic array of two MDM stub resonators side-coupled to a MDM waveguide. I found that decreasing the frequency spacing between the two resonances increases the slowdown factor and decreases the bandwidth of the slow-light band. I also showed that there is a trade-off between the slowdown factor and the propagation length of the slow-light mode. Unlike previously proposed structures, such waveguides exhibit a small group velocity dispersion and a large slowdown factor over a broad wavelength range, features which are highly desirable for practical applications of slow-light devices. In addition, if these waveguides are combined with gain and tunable refractive index materials, they could enable stopping and storing light in a subwavelength volume.

I next considered MZI sensors in which the sensing arm consists of a slow-light waveguide based on a plasmonic analogue of EIT. I showed that a MZI sensor using such a waveguide leads to approximately an order of magnitude enhancement in the refractive index sensitivity, and therefore in the minimum detectable refractive index change, compared to a MZI sensor using a conventional MDM waveguide.

I also investigated compact slit-based structures for coupling free space light into silver-silica-silver MDM plasmonic waveguides. In all cases, the total width of the incoupling structure was limited to less than 1.1μm, which approximately

corresponds to one wavelength in silica $\lambda_s = \lambda_0/n_s$, when operating at λ_0 =1.55 μm. I first considered a coupling structure consisting of a single slit extending half way into the dielectric core of the MDM waveguide. I found that the coupling efficiency of such a single slit structure is limited by a trade-off between the light power coupled into the slit, and the transmission of the slit-MDM waveguide T-shaped junction.

To enhance the coupling into the silver-silica-silver MDM plasmonic waveguide, I next considered a two-section slit structure. I found that for such a structure the upper slit section enhances the coupling of the incident light into the lower slit section, by improving the impedance matching between the incident plane wave and the lower slit mode. In addition, the use of the optimized two-section slit structure increases the reflectivities at both sides of the lower slit section, and therefore the resonance enhancement factor. On the other hand, the transmission of the T-shaped junction for the optimized two-section slit structure is smaller than the one of the optimized single slit structure. Overall, the use of an optimized two-section slit coupler resulted in $\sim$ 2.3 times enhancement of the coupling into the MDM plasmonic waveguide compared to the optimized single-slit coupler.

To further enhance the coupling into the silver-silica-silver MDM plasmonic waveguide, I considered a symmetric double-slit structure. I found that such a structure greatly enhances the coupling of the incident light into the slits. This is due to the fact that the incident light excites surface plasmons at the air-metal interfaces. In the case of a double-slit structure these plasmons are partially coupled into the slits, thus increasing the total light power collected by the structure. In addition, the resonance enhancement factor of the optimized double-slit coupler is slightly larger than the resonance enhancement factor of the optimized single slit coupler. Overall, the use of an optimized double-slit coupler resulted in $\sim$ 3.3

times enhancement of the coupling into the MDM plasmonic waveguide compared to the optimized single-slit coupler. I also found that, while the incoupling structures were all optimized at a single wavelength, the operation wavelength range for high coupling efficiency is broad.

7.2 Suggestions for Future Work

One of the potential future research directions is to perform shape optimization of plasmonic structures for slowing down light, sensing, and coupling to free space light. In this dissertation, I showed that the introduced slow-light waveguides based on a plasmonic analogue of EIT exhibit a small group velocity dispersion and a large slowdown factor over a broad wavelength range. Further optimizing the shape of the waveguiding structure could for example expand the wavelength range of large slowdown factors. Similarly, I showed that sensors using slow-light waveguides lead to large enhancements in the refractive index sensitivity compared to sensors using conventional MDM waveguides. And I also showed that the use of a double-slit coupler results in large enhancement of the coupling into a MDM plasmonic waveguide compared to a single-slit coupler. While the sensor and coupler structures that I introduced exhibit superior performance compared to previously introduced structures, using shape optimization could further enhance their performance. In addition, it would be interesting to identify the optimum structure geometry for specific device applications, and fundamental limits for their performance.

It would also be interesting to investigate alternative plasmonic sensor and coupler geometries. Coupled waveguide-cavity systems which are widely implemented in dielectric waveguide sensors could also be considered for plasmonic sensors. In

addition, an extension of the proposed slit-based couplers which are highly compact in one dimension, could be highly compact aperture-based coupling structures with wavelength-scale length and width. Moreover, the coupling structures considered here are polarization dependent. However, it should be possible to design circular aperture structures to provide polarization-independent coupling.

References

[1] M. T. Bohr, "Interconnect Scaling–The Real Limiter to High Performance ULSI," Tech. Dig. IEDM. **95**, 241–244 (1995).

[2] K. Banerjee, A. Amerasekera, G. Dixit, and C. Hu, "The effect of interconnect scaling and low-k dielectric on the thermal characteristics of the IC metal," Tech. Dig. IEDM. **96**, 65–68 (1996).

[3] H. Raether, *Surface Plasmons on Smooth and Rough Surfaces and on Gratings,* Ch. 2 (Springer, 1988).

[4] X. Shi and L. Hesselink,"Mechanisms for enhancing power throughput from planar nano-apertures for near field optical data storage," Jpn. J. Appl. Phys. **41**, 1632–1635 (2002).

[5] A. J. Huber, F. Keilmann, J. Wittborn, J. Aizpurua, and R. Hillenbrand,"Terahertz near field nanoscopy of mobile carriers in single semiconductor nanodevices," Nano Lett. **8**, 3766–3770 (2008).

[6] T. H. Taminiau, R. J. Moerland, F. B. Segerink, L. Kuipers, and N. F. van Hulst,"$\lambda/4$ resonance of an optical monopole antenna probed by single molecule fluorescence," Nano Lett. **7**, 28–33 (2007).

[7] E. N. Economou, "Surface plasmons in thin films," Phys. Rev. **182,** 539–554 (1969).

[8] M. Quinten, A. Leitner, J. R. Krenn, and F. R. Aussenegg, "Electromagnetic energy transport via linear chains of silver nanoparticles," Opt. Lett. **23,** 1331–1333 (1998).

[9] S. A. Maier, P. G. Kik, H. A. Atwater, S. Meltzer, E. Harel, B. E. Koel, and A. A. G. Requicha, "Local detection of electromagnetic energy transport below the diffraction limit in metal nanoparticle plasmon waveguides," Nat. Mater. **2,** 229–232 (2003).

[10] S. I. Bozhevolnyi, V. S. Volkov, E. Devaux, J. Y. Laluet, and T. W. Ebbesen, "Channel plasmon subwavelength waveguide components including interferometers and ring resonators," Nature **440**, 508–511 (2006).

[11] M. Yan and M. Qiu, "Guided plasmon polariton at 2D metal corners," J. Opt. Soc. Am. B. **24,** 2333–2342 (2007).

[12] A. D. Boardman, G. C. Aers, and R. Teshima, "Retarded edge modes of a parabolic wedge," Phys. Rev. B. **24,** 5703–5712 (1981).

[13] G. Veronis and S. Fan, "Bends and splitters in subwavelength metal-dielectric-metal plasmonic waveguides," Appl. Phys. Lett. **87,** 131102 (2005).

[14] J. S. White, G. Veronis, Z. Yu, E. S. Barnard, A. Chandran, S. Fan, and M. L. Brongersma, "Extraordinary optical absorption through subwavelength slits," Opt. Lett. **34,** 686–688 (2009).

[15] S. I. Bozhevolnyi, *Plasmonic Nanoguides and Circuits*, (World Scientific, 2009).

[16] C. Min, J. Li, G. Veronis, J. Y. Lee, S. Fan, and P. Peumans, "Enhancement of optical absorption in thin-film organic solar cells through the excitation of plasmonic modes in metallic gratings," Appl. Phys. Lett. **96,** 133302 (2010).

[17] T. Kume, S. Hayashi, and K. Yamamoto, "Enhancement of photoelectric conversion efficiency in copper phthalocyanine solar cell: white light excitation of surface plasmon polaritons," Jpn. J. Appl. Phys. **34,** 6448–6451 (1995).

[18] L. Cao, D. N. Barsic, A. R. Guichard, and M. L. Brongersma, "Plasmon-assisted local temperature control to pattern individual semiconductor nanowires and carbon nanotubes," Nano Lett. **7,** 3523–3527 (2007).

[19] L. R. Hirsch, R. J. Stafford, J. A. Bankson, S. R. Sershen, B. Rivera, R. E. Price, J. D. Hazle, N. J. Halas, and J. L. West, "Nanoshell-mediated near-infrared thermal therapy of tumours under magnetic resonance guidance," Proc. Natl. Acad. Sci. USA **100,** 13549–13554 (2003).

[20] A. O. Govorov, W. Zhang, T. Skeini, H. Richardson, J. Lee, and N. A. Kotov, "Gold nanoparticles ensembles as heaters and actuators: melting and collective plasmon resonances," Nanoscale Res. Lett. **1,** 84–90 (2006).

[21] A. Nahata, R. A. Linke, T. Ishi, and K. Ohashi, "Enhanced nonlinear optical conversion from a periodically nanostructured metal film," Opt. Lett. **28,** 423–425 (2003).

[22] A. Ymeti, J. Greve, P. V. Lambeck, T. Wink, S. W. F. M. van Hovell, T. A. M. Beumer, R. R. Wijn, R. G. Heideman, V. Subramaniam, and J. S. Kanger, "Fast, ultrasensitive virus detection using a Young interferometer sensor," Nano Lett. **7,** 394–397 (2007).

[23] V. M. Shalaev, "Optical negative-index metamaterials," Nature Photon. **1,** 41–48 (2007).

[24] A. Hryciw, Y. C. Jun, and M. L. Brongersma, "Plasmonics: Electrifying plasmonics on silicon," Nat. Mater. **9,** 3–4 (2010).

[25] W. L. Barnes, A. Dereux, and T. W. Ebbesen, "Surface plasmon subwavelength optics," Nature **424**, 824–830 (2003).

[26] R. Zia, J. A. Schuller, A. Chandran, and M. L. Brongersma, "Plasmonics: the next chip-scale technology," Materials Today **9**, 20–27 (2006).

[27] E. Ozbay, "Plasmonics: Merging photonics and electronics at nanoscale dimensions," Science **311**, 189–193 (2006).

[28] S. A. Maier and H. A. Atwater, "Plasmonics: localization and guiding of electromagnetic energy in metal/dielectric structures," J. Appl. Phys. **98**, 011101 (2005).

[29] P. Tassin, L. Zhang, T. Koschny, E. N. Economou, and C. M. Soukoulis, "Low loss metamaterials based on classical electromagnetically induced transparency," Phys. Rev. Lett. **102**, 053901 (2009).

[30] S. Fan, M. F. Yanik, Z. Wang, S. Sandhu, and M. L. Povinelli, "Advances in theory of photonic crystals," J. Lightw. Technol. **24**, 4493–4501 (2006).

[31] S. Zhang, D. A. Genov, Y. Wang, M. Liu, and X. Zhang, "Plasmon-induced transparency in metamaterials," Phys. Rev. Lett. **101**, 047401 (2008).

[32] N. Papasimakis, V. A. Fedotov, and N. I. Zheludev, "Metamaterial analog of electromagnetically induced transparency," Phys. Rev. Lett. **101**, 253903 (2008).

[33] N. Liu, L. Langguth, T. Weiss, J. Ktel, M. Fleischhauer, T. Pfau, and H. Giessen, "Plasmonic analogue of electromagnetically induced transparency at the Drude damping limit," Nature Mat. **8**, 758–762 (2009).

[34] M. F. Yanik, W. J. Suh, Z. Wang, and S. Fan, "Stopping Light in a Waveguide with an All-Optical Analog of Electromagnetically Induced Transparency," Phys. Rev. Lett. **93**, 233903 (2004).

[35] Q. Xu, S. Sandhu, M. Povinelli, J. Shakya, S. Fan, and M. Lipson, "Experimental Realization of an On- Chip All-Optical Analogue to Electromagnetically Induced Transparency," Phys. Rev. Lett. **96**, 123901 (2006).

[36] G. Veronis and S. Fan, "Theoretical investigation of compact couplers between dielectric slab waveguides and two-dimensional metal-dielectric-metal plasmonic waveguides," Opt. Express **15,** 1211–1221 (2007).

[37] E. Feigenbaum and M. Orenstein, "Modeling of complementary void plasmon waveguiding," J. Lightwave Technol. **25,** 2547–2562 (2007).

[38] R. A. Wahsheh, Z. L. Lu, and M. A. G. Abushagur, "Nanoplasmonic couplers and splitters," Opt. Express **17,** 19033–19041 (2009).

[39] R. X. Yang, R. A. Wahsheh, Z. L. Lu, and M. A. G. Abushagur, "Efficient light coupling between dielectric slot waveguide and plasmonic slot waveguide," Opt. Lett **35,** 649–651 (2010).

[40] J. Tian, S. Yu, W. Yan, and M. Qiu, "Broadband high-efficiency surface plasmon polariton couplers with silicon-metal interface," Appl. Phys. Lett. **95,** 013504 (2009).

[41] C. Delacour, S. Blaize, P. Grosse, J. M. Fedeli, A. Bruyant, R. S. Montiel, G. Lerondel, and A. Chelnokov, "Efficient Directional Coupling between Silicon and Copper Plasmonic Nanoslot Waveguides: toward Metal-Oxide-Silicon Nanophotonics," Nano Lett. **10,** 2922–2926 (2010).

[42] M. J. Preiner, K. T. Shimizu, J. S. White, and N. A. Melosh, "Efficient optical coupling into metal-insulator-metal plasmon modes with subwavelength diffraction gratings," Appl. Phys. Lett. **92,** 113109 (2008).

[43] J. A. Dionne, H. J. Lezec, and H. A. Atwater, "Metal-dielectric slot-waveguide structures for the propagation of surface plasmon polaritons at 1.55 μm," Nano Lett. **6,** 1928–1932 (2006).

[44] H. J. Lezec, J. A. Dionne, and H. A. Atwater, "Negative refraction at visible frequencies," Science **316,** 430–432 (2007).

[45] P. Neutens, P. V. Dorpe, I. D. Vlaminck, L. Lagae, and G. Borghs, "Electrical detection of confined gap plasmons in metal-insulator-metal waveguides," Nature Photonics **19,** 283–286 (2009).

[46] K. Diest, J. A. Dionne, M. Spain, and H. A. Atwater, "Tunable Color Filters Based on Metal-Insulator-Metal Resonators," Nano Lett. **9,** 2579–2583 (2009).

[47] S. A. Maier, *Plasmonics: Fundamentals and Applications* (Springer, New York, 2007).

[48] L. Novotny, B. Hecht, and D. W. Pohl,"Interference of locally excited surface plasmons," J. Appl. Phys. **81**, 1798–1806 (1997).

[49] E. Prodan, P. Nordlander, and N. J. Halas, "Effects of dielectric screening on the optical properties of metallic nanoshells," Chem. Phys. Lett. **368**, 94–101 (2003).

[50] C. F. Bohren, D. R. Huffman, *Absorption and Scattering of Light by Small Particles*, (Wiley, New York, 1983).

[51] E. D. Palik, *Handbook of Optical Constants of Solids*, (Academic, New York, 1985).

[52] A. Taflove, *Computational Electrodynamics*, (Artech House, Boston, 1995).

[53] A. D. Rakic, A. B. Djurisic, J. M. Elazar, and M. L. Majewski,"Optical properties of metallic films for vertical cavity optoelectronic devices," Appl. Opt. **37**, 5271–5283 (1998).

[54] A. Vial, A. S. Grimault, D. Macias, D. Barchiesi, and M. L. De la Chapelle, "Improved analytical fit of gold dispersion: application to the modeling of extinction spectra with a finite-difference time-domain method," Phys. Rev. B. **71**, 85416 (2005).

[55] J. D. Jackson, *Classical Electrodynamics*, (Wiley, New York, 1999).

[56] J. Jin, *The Finite Element Method in Electromagnetics*, (Wiley, New York, 2002).

[57] J. L. Young and R. O. Nelson, "A summary and systematic analysis of FDTD algorithms for linearly dispersive media," IEEE Antennas Propag. Mag. **43**, 61–77 (2001).

[58] M. N. O. Sadiku, *Numerical Techniques in Electromagnetics*, (CRC Press, Boca Raton, 2001).

[59] Y. Huang, C. Min, and G. Veronis, "Subwavelength slow-light waveguides based on a plasmonic analogue of electromagnetically induced transparency," Appl. Phys. Lett. **99,** 143117 (2011).

[60] U. S. Inan and R. A. Marshall, *Numerical Electromagnetics: The FDTD Method*, (Cambridge University Press, 2011).

[61] J. B. Khurgin, "Slow light in various media: a tutorial," Adv. Opt. Phot. **2**, 287 (2010).

[62] J. R. Pierce, *Traveling Wave Tubes*, (Van Nostrand, 1950).

[63] S. L. McCall and E. L. Hahn, "Self-induced transparency by pulsed coherent light," Phys. Rev. Lett. **18**, 908–911 (1967).

[64] D. Grischkowsky, and E. L. Hahn, "Adiabatic following and slow optical pulse propagation in rubidium vapor," Phys. Rev. A. **7**, 2096 (1973).

[65] S. E. Harris, "Electromagnetically induced transparency," Phys. Today. **50**, 36–42 (1997).

[66] L. V. Hau, S. E. Harris, Z. Dutton, and C. H. Behroozi, "Light speed reduction to 17 metres per second in an ultracold atomic gas," Nature **397**, 594–598 (1999).

[67] M. O. Scully and M. S. Zubairy, *Quantum Optics*, (Cambridge U. Press, Cambridge, UK, 1997).

[68] M. D. Lukin and A. Imamoglu, "Controlling photons using electromagnetically induced transparency," Nature **413**, 273–276 (2001).

[69] M. Soljacic, S. G. Johnson, S. Fan, M. Ibanescu, E. Ippen and J. D. Joannopoulos, "Photonic crystal slow light enhancement of nonlinear phase sensitivity," J. Opt. Soc. Am. B **19**, 2052–2059 (2002).

[70] T. F. Krauss, "Why do we need slow light?" Nature Photonics **2**, 448 (2008).

[71] R. W. Boyd and D. J. Gauthier, "Controlling the velocity of light pulses," Science **326**, 1074–1077 (2009).

[72] Z. Dutton, N. S. Ginsberg, C. Slowe, and L. V. Hau,"The Art of Taming Light: Ultra-slow and Stopped Light," Europhysics News **35**, 33–39 (2004).

[73] M. D. Lukin, A. Imamoglu, C. Slowe, and L. V. Hau,"Nonlinear optics and quantum entanglement of ultra-slow single photons," Phys. Rev. Lett. **84**, 1419 (2000).

[74] A. Karalis, E. Lidorikis, M. Ibanescu, J. Joannopoulos, and M. Soljacic, "Surface-Plasmon-Assisted Guiding of Broadband Slow and Subwavelength Light in Air," Phys. Rev. Lett. **95**, 063901 (2005).

[75] M. Sandtke and L. Kuipers, "Slow guided surface plasmons at telecom frequencies," Nature Photonics **1**, 573 (2007).

[76] Z. Kang, W. Lin, and G. P. Wang, "Dual-channel broadband slow surface plasmon polaritons in metal gap waveguide superlattices," J. Opt. Soc. Am. B **26**, 1944–1948 (2009).

[77] Q. Gan, Y. J. Ding, and F. J. Bartoli, "Ultra-wide Band Slow Light System Based on THz Plasmonic Graded Metal Grating Structures," Phys. Rev. Lett. **102,** 056801 (2009).

[78] A. Kocabas, S. S. Senlik, and A. Aydinli, "Slowing Down Surface Plasmons on a Moire Surface," Phys. Rev. Lett. **102**, 063901 (2009).

[79] E. Feigenbaum and M. Orenstein, "Backward propagating slow light in inverted plasmonic taper," Opt. Express **17**, 2465–2469 (2009).

[80] L. Yang, C. Min, and G. Veronis, "Guided subwavelength slow-light mode supported by a plasmonic waveguide system," Opt. Lett. **35**, 4184–4186 (2010).

[81] Y. Matsuzaki, T. Okamoto, M. Haraguchi, M. Fukui, and M. Nakagaki, "Characteristics of gap plasmon waveguide with stub structures," Opt. Express **16**, 16314–16325 (2008).

[82] X. S. Lin and X. G. Huang, "Tooth-shaped plasmonic waveguide filters with nanometeric sizes," Opt. Lett. **33**, 2874–2876 (2008).

[83] J. Liu, G. Fang, H. Zhao, Y. Zhang, and S. Liu, "Surface plasmon reflector based on serial stub structure," Opt. Express **17**, 20134–20139 (2009).

[84] C. Min and G. Veronis, "Absorption switches in metal-dielectric-metal plasmonic waveguides," Opt. Express **17**, 10757–10766 (2009).

[85] R. D. Kekatpure, E. S. Barnard, W. Cai, and M. L. Brongersma, "Phase-coupled plasmon-induced transparency," Phys. Rev. Lett. **104**, 243902 (2010).

[86] Z. Han and S. I. Bozhevolnyi, "Plasmon-induced transparency with detuned ultracompact Fabry-Perot resonators in integrated plasmonic devices," Opt. Express **19**, 3251–3257 (2011).

[87] S. E. Kocabas, G. Veronis, D. A. B. Miller, and S. Fan, "Transmission line and equivalent circuit models for plasmonic waveguide components," IEEE J. Sel. Topics Quantum Electron. **14**, 1462–1472 (2008).

[88] T. Vo-Dinh, *Biomedical Photonics Handbook*, (CRC Press LLC, 2003).

[89] C. Genet, and T. W. Ebbesen, "Light in tiny holes," Nature **445,** 39–46 (2007).

[90] J. Weiner, "The physics of light transmission through subwavelength apertures and aperture arrays," Reports on Progress in Physics **72,** 064401 (2009).

[91] X. D. Fan, I. M. White, S. I. Shopova, H. Y. Zhu, J. D. Suter, and Y. Z. Sun, "Sensitive optical biosensors for unlabeled targets: A review," Analytica Chimica Acta **620,** 8–26 (2008).

[92] H. K. Hunt and A. M. Armani, "Label-free biological and chemical sensors," Nanoscale **2,** 1544–1559 (2010).

[93] F. Vollmer and S. Arnold, "Whispering-gallery-mode biosensing: label-free detection down to single molecules," Nature Methods **5,** 591–596 (2008).

[94] Y. Z. Sun and X. D. Fan, "Optical ring resonators for biochemical and chemical sensing," Analytical and Bioanalytical Chemistry **399,** 205–211 (2011).

[95] T. Yoshie, L. L. Tang, and S. Y. Su, "Optical microcavity: Sensing down to single molecules and atoms," Sensors **399,** 1972–1991 (2011).

[96] K. De Vos, J. Girones, T. Claes, Y. De Koninck, S. Popelka, E. Schacht, R. Baets, and P. Bienstman, "Multiplexed antibody detection with an array of silicon-on-insulator microring resonators," IEEE Photonics Journal **1,** 225–235 (2009).

[97] P. Debackere, S. Scheerlinck, P. Bienstman, and R. Baets, "Surface plasmon interferometer in silicon-on-insulator: novel concept for an integrated biosensor," Opt. Express **14,** 7063–7072 (2006).

[98] P. Debackere, R. Baets, and P. Bienstman, "Bulk sensing experiments using a surface-plasmon interferometer," Opt. Lett. **34,** 2858–2860 (2009).

[99] M. R. Lee and P. M. Fauchet, "Nanoscale microcavity sensor for single particle detection," Opt. Lett. **32,** 3284–3286 (2007).

[100] C. A. Barrios, M. J. Banuls, V. Gonzalez-Pedro, K. B. Gylfason, B. Sanchez, A. Griol, A. Maquieira, H.Sohlstrom, M. Holgado, and R. Casquel, "Label-free optical biosensing with slot-waveguides," Opt. Lett. **33,** 708–710 (2008).

[101] C. A. Barrios, B. Sanchez, K. B. Gylfason, A. Griol, H. Sohlstrom, M. Holgado, and R. Casquel, "Slot-waveguide biochemical sensor," Opt. Lett. **32,** 3080–3082 (2007).

[102] P. Berini, "Bulk and surface sensitivities of surface plasmon waveguides," New J. Phys. **10,** 105010 (2008).

[103] J. Feng, V. S. Siu, A. Roelke, V. Mehta, S. Y. Rhieu, G. T. R. Palmore, and D. Pacifici, "Nanoscale plasmonic interferometers for multispectral, high-throughput biochemical sensing," Nano Lett. **12,** 602–609 (2012).

[104] K. M. Mayer, and J. Hafner, "Localized surface plasmon resonance sensors," Chem. Rev. **111,** 3828–3857 (2011).

[105] J. R. Krenn, B. Lamprecht, H. Ditlbacher, G. Schider, M. Salerno, A. Leitner, and F. R. Aussenegg, "Non-diffraction-limited light transport by gold nanowires," Europhys. Lett. **60,** 663–669 (2002).

[106] R. Zia, M. D. Selker, P. B. Catrysse, and M. L. Brongersma, "Geometries and materials for subwavelength surface plasmon modes," J. Opt. Soc. Am. A **21**, 2442–2446 (2004).

[107] A. Hosseini and Y. Massoud, "Nanoscale surface plasmon based resonator using rectangular geometry," Appl. Phys. Lett. **90**, 181102 (2007).

[108] Y. Matsuzaki, T. Okamoto, M. Haraguchi, M. Fukui, and M. Nakagaki, "Characteristics of gap plasmon waveguide with stub structures," Opt. Express **16**, 16314–16325 (2008).

[109] X. S. Lin and X. G. Huang, "Tooth-shaped plasmonic waveguide filters with nanometric sizes," Opt. Lett. **33**, 2874–2876 (2008).

[110] D. M. Pozar, *Microwave Engineering*, (Wiley, New York, 1998).

[111] S. D. Wu and E. N. Glytsis, "Finite-number-of-periods holographic gratings with finite-width incident beams: analysis using the finite-difference frequency-domain method," J. Opt. Soc. Am. **65,** 2018–2029 (2002).

[112] G. Veronis, R. W. Dutton, and S. Fan, "Method for sensitivity analysis of photonic crystal devices," Opt. Lett **29,** 2288–2290 (2004).

[113] S. Ramo, J. R. Whinnery, and T. Van Duzer, *Fields and Waves in Communication Electronics*, (Wiley, New York, 1994).

[114] K. Krishnakumar, "Micro-genetic algorithms for stationary and non-stationary function optimization," Proc. SPIE **1196,** 289–296 (1989).

[115] C. Min, L. Yang, and G. Veronis, "Microcavity enhanced optical absorption in subwavelength slits," Opt. Express **19,** 26850–26858 (2011).

[116] L. Verslegers, Z. Yu, P. B. Catrysse, and S. Fan, "Temporal coupled-mode theory for resonant apertures," J. Opt. Soc. Am. B **27,** 1947–1956 (2010).

[117] C. A. Balanis, *Antenna Theory: Analysis and Design*, 3rd ed. (Wiley, New York, 1983).

Appendix A: Proof of Eq.(4.1)

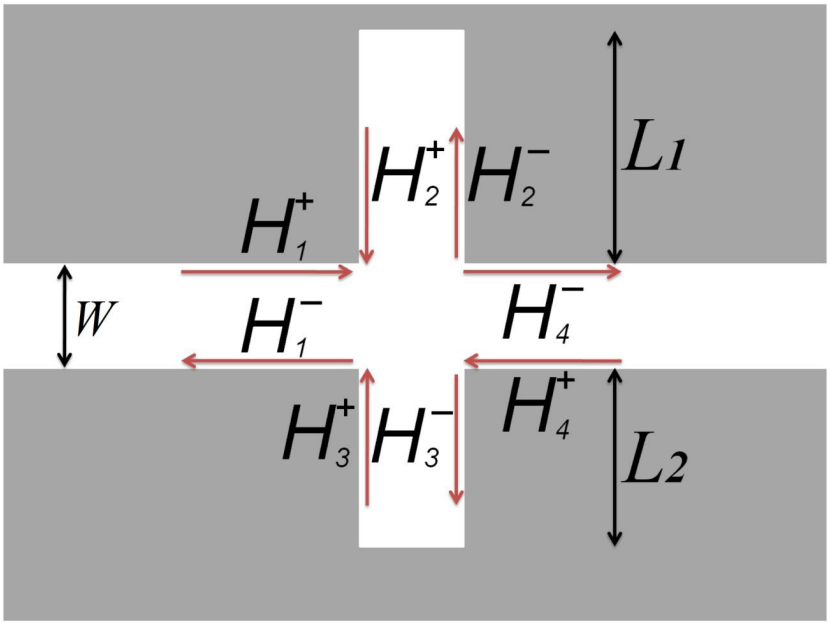

FIGURE A.1. Schematic defining the amplitudes and phases of the fundamental TM modes of the MDM waveguide that arrive at each port of a MDM plasmonic waveguide side-coupled to two MDM stub resonators, H^+, and the amplitudes and phases of the modes that propagate away from each port, H^-.

I consider a waveguide crossing as in Fig. A.1. The scattering matrix relates the amplitudes and phases of the modes that arrive at each port, H^+, to the amplitudes and phases of the modes that propagate away from each port, H^-:

$$\begin{bmatrix} H_1^- \\ H_2^- \\ H_3^- \\ H_4^- \end{bmatrix} = \begin{bmatrix} S_{11} & S_{12} & S_{13} & S_{14} \\ S_{21} & S_{22} & S_{23} & S_{24} \\ S_{31} & S_{32} & S_{33} & S_{34} \\ S_{41} & S_{42} & S_{43} & S_{44} \end{bmatrix} \begin{bmatrix} H_1^+ \\ H_2^+ \\ H_3^+ \\ H_4^+ \end{bmatrix}. \tag{A.1}$$

I consider the complex magnetic field reflection coefficient r_1, and transmission coefficients t_1, t_2, t_3 when the fundamental TM mode of the MDM waveguide is incident at a waveguide crossing (Fig. 4.2(a)). I have

$$S_{11} = \frac{H_1^-}{H_1^+}|_{H_2^+=H_3^+=H_4^+=0},$$

$$S_{22} = \frac{H_2^-}{H_2^+}|_{H_1^+=H_3^+=H_4^+=0},$$
$$S_{33} = \frac{H_3^-}{H_3^+}|_{H_1^+=H_2^+=H_4^+=0},$$
$$S_{44} = \frac{H_4^-}{H_4^+}|_{H_1^+=H_2^+=H_3^+=0},$$

and because of symmetry, I obtain

$$S_{11} = S_{22} = S_{33} = S_{44} = r_1. \tag{A.2}$$

When H_2^+=H_3^+=H_4^+=0, I have

$$H_2^- = S_{21}H_1^+,\ H_3^- = S_{31}H_1^+,\ H_4^- = S_{41}H_1^+.$$

When H_1^+=H_3^+=H_4^+=0, I have

$$H_1^- = S_{12}H_2^+,\ H_3^- = S_{32}H_2^+,\ H_4^- = S_{42}H_2^+.$$

When H_1^+=H_2^+=H_4^+=0, I have

$$H_1^- = S_{13}H_3^+,\ H_2^- = S_{23}H_3^+,\ H_4^- = S_{43}H_3^+.$$

When H_1^+=H_2^+=H_3^+=0, I have

$$H_1^- = S_{14}H_4^+,\ H_2^- = S_{24}H_4^+,\ H_3^- = S_{34}H_4^+.$$

Because of symmetry, I have

$$S_{14} = S_{41} = S_{23} = S_{32} = t_1, \tag{A.3}$$

and

$$S_{11} = S_{21} = S_{13} = S_{31} = S_{24} = S_{42} = S_{34} = S_{43} = t_2. \tag{A.4}$$

Inserting equations (A.2), (A.3) and (A.4) in (A.1) gives

$$\begin{bmatrix} H_1^- \\ H_2^- \\ H_3^- \\ H_4^- \end{bmatrix} = \begin{bmatrix} r_1 & t_2 & t_2 & t_1 \\ t_2 & r_1 & t_1 & t_2 \\ t_2 & t_1 & r_1 & t_2 \\ t_1 & t_2 & t_2 & r_1 \end{bmatrix} \begin{bmatrix} H_1^+ \\ H_2^+ \\ H_3^+ \\ H_4^+ \end{bmatrix}. \tag{A.5}$$

Considering the reflection at the boundary of a short-circuited MDM waveguide (Fig. 4.2(b)), I have

$$H_2^- = s_1 H_2^+, \tag{A.6}$$

$$H_3^- = s_2 H_3^+. \tag{A.7}$$

Here, $s_i = r_2^{-1} \exp(2\gamma_{\mathrm{MDM}} L_i)$, $i = 1, 2$, r_2 is the magnetic field reflection coefficient of the fundamental TM mode of the MDM waveguide at the boundary of a short-circuited MDM waveguide (Fig. 4.2(b)), and $\gamma_{\mathrm{MDM}} = \alpha_{\mathrm{MDM}} + i\beta_{\mathrm{MDM}}$ is the complex wave vector of the fundamental propagating TM mode in a MDM waveguide of width w. Substituting equations (A.6) and (A.7) into (A.5) gives

$$H_1^- = r_1 H_1^+ + t_2 H_2^+ + t_2 H_3^+ + t_1 H_4^+, \tag{A.8}$$

$$s_1 H_2^+ = t_2 H_1^+ + r_1 H_2^+ + t_1 H_3^+ + t_2 H_4^+, \tag{A.9}$$

$$s_2 H_3^+ = t_2 H_1^+ + t_1 H_2^+ + r_1 H_3^+ + t_2 H_4^+, \tag{A.10}$$

$$H_4^- = t_1 H_1^+ + t_2 H_2^+ + t_2 H_3^+ + r_1 H_4^+. \tag{A.11}$$

Using equations (A.9) and (A.10), I obtain

$$H_3^+ = (\frac{t_1 - r_1 + s_1}{t_1 - r_1 + s_2}) H_2^+. \tag{A.12}$$

Substituting equation (A.12) into (A.8) gives

$$H_1^- = r_1 H_1^+ + t_2 (1 + \frac{t_1 - r_1 + s_1}{t_1 - r_1 + s_2}) H_2^+ + t_1 H_4^+. \tag{A.13}$$

Substituting equation (A.12) into equation (A.9), one gets

$$0 = t_2 H_1^+ + (r_1 - s_1 + r_1 \frac{t_1 - r_1 + s_1}{t_1 - r_1 + s_2}) H_2^+ + t_2 H_4^+. \tag{A.14}$$

Using equations (A.13) and (A.14) and eliminating H_2^+, I obtain

$$(\frac{t_1}{A} - \frac{t_2}{B})H_4^+ = (\frac{t_2}{B} - \frac{r_1}{A})H_1^+ + \frac{1}{A}H_1^-, \tag{A.15}$$

where $A = t_2(1 + \frac{t_1 - r_1 + s_1}{t_1 - r_1 + s_2})$, and $B = r_1 - s_1 + r_1\frac{t_1 - r_1 + s_1}{t_1 - r_1 + s_2}$.

Furthermore, using equations (A.8) and (A.11), gives

$$(t_1 - r_1)H_1^+ + H_1^- = (t_1 - r_1)H_4^+ + H_4^-. \tag{A.16}$$

Combining equations (A.15) and (A.16), I obtain the system

$$\begin{bmatrix} t_1 - r_1 & 1 \\ \frac{t_1}{A} - \frac{t_2}{B} & 0 \end{bmatrix} \begin{bmatrix} H_4^+ \\ H_4^- \end{bmatrix} = \begin{bmatrix} t_1 - r_1 & 1 \\ \frac{t_2}{B} - \frac{r_1}{A} & \frac{1}{A} \end{bmatrix} \begin{bmatrix} H_1^+ \\ H_1^- \end{bmatrix}. \tag{A.17}$$

Using equation (A.17), I finally obtain

$$\begin{bmatrix} H_4^+ \\ H_4^- \end{bmatrix} = M \begin{bmatrix} H_1^+ \\ H_1^- \end{bmatrix}, \tag{A.18}$$

where

$$M = \begin{bmatrix} M_{11} & M_{12} \\ M_{21} & M_{22} \end{bmatrix} = \begin{bmatrix} t_1 - r_1 & 1 \\ \frac{t_1}{A} - \frac{t_2}{B} & 0 \end{bmatrix}^{-1} \begin{bmatrix} t_1 - r_1 & 1 \\ \frac{t_2}{B} - \frac{r_1}{A} & \frac{1}{A} \end{bmatrix}. \tag{A.19}$$

By definition, the power transmission coefficient $T = \left|\frac{H_4^-}{H_1^+}|_{H_4^+=0}\right|^2 = \left|\frac{H_1^-}{H_4^+}|_{H_1^+=0}\right|^2$ due to symmetry. Therefore, the power transmission spectra T of the two-cavity system can then be calculated using scattering matrix theory as

$$T = \left|\frac{1}{M_{12}}\right|^2 = \left|M_{21} - \frac{M_{11}M_{22}}{M_{12}}\right|^2 = \left|t_1 - \frac{t_2^2(2t_1 - 2r_1 + s_1 + s_2)}{t_1^2 - (r_1 - s_1)(r_1 - s_2)}\right|^2. \tag{A.20}$$

Appendix B: Proof of Eq.(4.2)

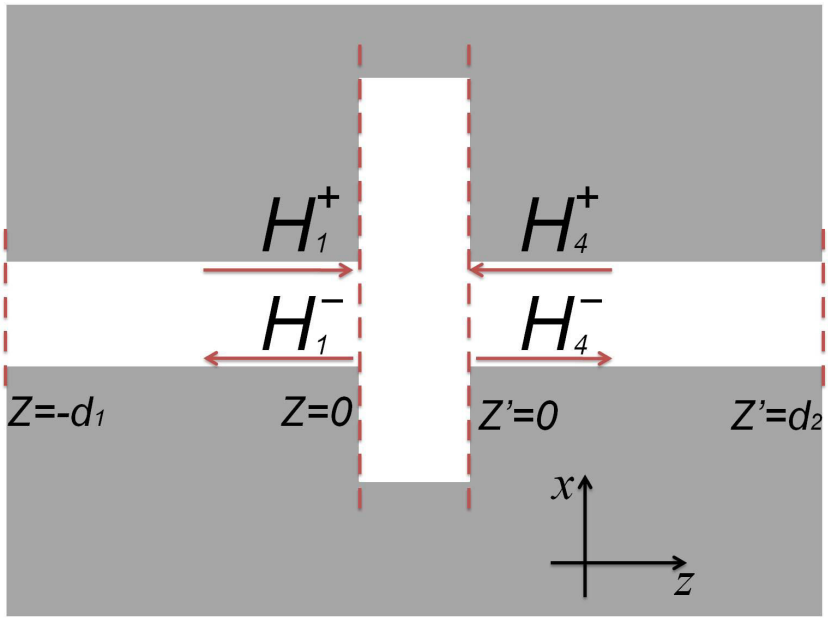

FIGURE B.1. Schematic showing a period of the plasmonic waveguide system of Fig. 4.5.

In Fig. B.1, I show a single period of the plasmonic waveguide system of Fig. 4.5. The magnetic field for $-d_1 < z < 0$ is given by

$$H_y(x,z) = [H_1^+ \exp(-\gamma_{\mathrm{MDM}} z) + H_1^- \exp(\gamma_{\mathrm{MDM}} z)]\phi(x). \tag{B.1}$$

Using Maxwell's equation $\nabla \times \mathbf{H} - j\omega\epsilon\mathbf{E} = 0$ we obtain

$$\begin{aligned} E_x(x,z) &= \frac{-1}{j\omega\epsilon}\frac{\partial H_y(x,z)}{\partial z} \\ &= \frac{-\gamma_{\mathrm{MDM}}}{j\omega\epsilon}[-H_1^+ \exp(-\gamma_{\mathrm{MDM}} z) + H_1^- \exp(\gamma_{\mathrm{MDM}} z)]\phi(x), \end{aligned} \tag{B.2}$$

where γ_{MDM} and $\phi(x)$ are the complex wave vector and the field profile of the fundamental TM mode in the plasmonic waveguide, respectively. Setting $H_1^* = H_y|_{z=-d_1}$ and $E_1^* = E_x|_{z=-d_1}$, I have

$$H_1^* = [H_1^+ \exp(\gamma_{\mathrm{MDM}} d_1) + H_1^- \exp(-\gamma_{\mathrm{MDM}} d_1)]\phi(x), \tag{B.3}$$

$$E_1^* = \frac{\gamma_{\mathrm{MDM}}}{j\omega\epsilon}[H_1^+ \exp(\gamma_{\mathrm{MDM}} d_1) - H_1^- \exp(-\gamma_{\mathrm{MDM}} d_1)]\phi(x). \tag{B.4}$$

Combining equations (B.3) and (B.4), I obtain

$$\begin{bmatrix} H_1^* \\ \frac{E_1^*}{Z_0} \end{bmatrix} = T_i \begin{bmatrix} H_1^+ \\ H_1^- \end{bmatrix} \phi(x), \tag{B.5}$$

where

$$T_i = \begin{bmatrix} 1 & 1 \\ \frac{\gamma_{\mathrm{MDM}}}{j\omega\epsilon Z_0} & \frac{-\gamma_{\mathrm{MDM}}}{j\omega\epsilon Z_0} \end{bmatrix} \begin{bmatrix} \exp(\gamma_{\mathrm{MDM}} d_1) & 0 \\ 0 & \exp(-\gamma_{\mathrm{MDM}} d_1) \end{bmatrix}, \tag{B.6}$$

and $Z_0 = (\frac{\mu_0}{\epsilon_0})^{-\frac{1}{2}}$.

Similarly, the magnetic field for $0 < z^{'} < d_2$ is given by

$$H_y(x, z^{'}) = [H_4^+ \exp(\gamma_{\mathrm{MDM}} z^{'}) + H_4^- \exp(-\gamma_{\mathrm{MDM}} z^{'})]\phi(x). \tag{B.7}$$

Using Maxwell's equations again, I obtain

$$\begin{aligned} E_x(x, z^{'}) &= \frac{-1}{j\omega\epsilon} \frac{\partial H_y(x, z^{'})}{\partial z'} \\ &= \frac{-\gamma_{\mathrm{MDM}}}{j\omega\epsilon}[H_4^+ \exp(\gamma_{\mathrm{MDM}} z^{'}) - H_4^- \exp(-\gamma_{\mathrm{MDM}} z^{'})]\phi(x). \end{aligned} \tag{B.8}$$

Setting $H_4^* = H_y|_{z'=d_2}$ and $E_4^* = E_x|_{z'=d_2}$, I have

$$H_4^* = [H_4^+ \exp(\gamma_{\mathrm{MDM}} d_2) + H_4^- \exp(-\gamma_{\mathrm{MDM}} d_2)]\phi(x), \tag{B.9}$$

$$E_4^* = \frac{\gamma_{\mathrm{MDM}}}{j\omega\epsilon}[-H_4^+ \exp(\gamma_{\mathrm{MDM}} d_2) + H_4^- \exp(-\gamma_{\mathrm{MDM}} d_2)]\phi(x). \tag{B.10}$$

Combining equations (B.9) and (B.10), I obtain

$$\begin{bmatrix} H_4^* \\ \frac{E_4^*}{Z_0} \end{bmatrix} = T_o \begin{bmatrix} H_4^+ \\ H_4^- \end{bmatrix} \phi(x), \tag{B.11}$$

where

$$T_o = \begin{bmatrix} 1 & 1 \\ \frac{-\gamma_{\mathrm{MDM}}}{j\omega\epsilon Z_0} & \frac{\gamma_{\mathrm{MDM}}}{j\omega\epsilon Z_0} \end{bmatrix} \begin{bmatrix} \exp(\gamma_{\mathrm{MDM}} d_2) & 0 \\ 0 & \exp(-\gamma_{\mathrm{MDM}} d_2) \end{bmatrix}. \tag{B.12}$$

Then, using equation (A.18), I obtain

$$\begin{bmatrix} H_4^* \\ \frac{E_4^*}{Z_0} \end{bmatrix} = T_o M T_i^{-1} \begin{bmatrix} H_1^* \\ \frac{E_1^*}{Z_0} \end{bmatrix}. \tag{B.13}$$

Here, $T_o M T_i^{-1}$ is the transfer matrix for a single period of the EIT-like system of Fig. 4.5.

On the other hand, by Bloch theorem I have

$$\begin{bmatrix} H_4^* \\ \frac{E_4^*}{Z_0} \end{bmatrix} = \exp(\gamma d) \begin{bmatrix} H_1^* \\ \frac{E_1^*}{Z_0} \end{bmatrix}, \tag{B.14}$$

where $\gamma = \alpha + i\beta$ is the Bloch wave vector. In fact, both $\exp(\gamma d)$ and $\exp(-\gamma d)$ are eigen-values of the transfer matrix. Thus, for the two eigen-values of the transfer matrix, I have

$$\exp(\gamma d) + \exp(-\gamma d) = tr(T_o M T_i^{-1}). \tag{B.15}$$

By substituting equations (A.19), (B.6), and (B.12) into (B.15), I finally obtain

$$\cosh(\gamma d) = \frac{A}{2} \exp[-\gamma_{\mathrm{MDM}}(d-w)] + \frac{B}{2} \exp[\gamma_{\mathrm{MDM}}(d-w)], \tag{B.16}$$

where $A = (t_1 - r_1)\frac{t_1 + r_1 - 2C}{t_1 - C}$, and $B = (t_1 - C)^{-1}$.

Appendix C: Proof of Eq.(6.1)

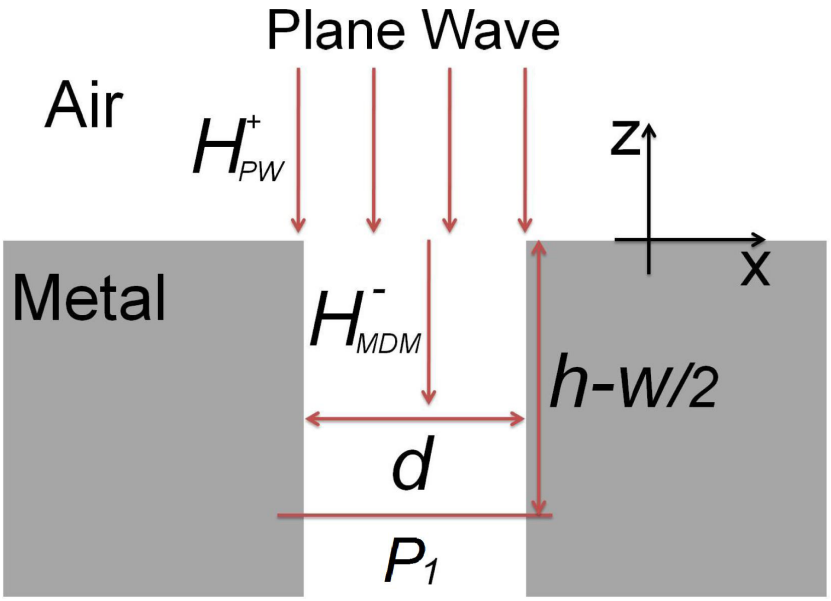

FIGURE C.1. Schematic showing a plane wave which is normally incident from free space on a semi-infinite MDM plasmonic waveguide.

I consider a plane wave which is normally incident from free space on a semi-infinite MDM waveguide (Fig. C.1). For z > 0, the field components of the TM-polarized incident plane wave are

$$H_y^{PW}(x,z) = H_{PW}^{+}\exp(-jk_0 z), \tag{C.1}$$

$$E_x^{PW}(x,z) = \frac{-1}{j\omega\epsilon_0}\frac{\partial H_y^{PW}(x,z)}{\partial z} = E_{PW}^{+}\exp(-jk_0 z), \tag{C.2}$$

where $k_0 = \omega\sqrt{\epsilon_0\mu_0}$, and $E_{PW}^{+} = H_{PW}^{+}\sqrt{\frac{\mu_0}{\epsilon_0}}$.

For z < 0 I have

$$H_y^{M}(x,z) = H_{MDM}^{-}\exp(-\gamma_1 z)\phi(x), \tag{C.3}$$

$$E_x^{M}(x,z) = \frac{-1}{j\omega\epsilon_0}\frac{\partial H_y^{M}}{\partial z} = E_{MDM}^{-}\exp(-\gamma_1 z)\phi(x), \tag{C.4}$$

where $E^-_{MDM} = \frac{\gamma_1}{j\omega\epsilon} H^-_{MDM}$, and γ_1 and $\phi(x)$ are the complex wave vector and field profile of the fundamental TM mode in the plasmonic waveguide, respectively.

The power density of the incident plane wave is given by the Poynting vector

$$\left|\mathbf{S}_{PW}\right| = \left|\frac{1}{2} Re(\mathbf{E}\times\mathbf{H}^*)\right| = \frac{1}{2}|H^+_{PW}|^2\sqrt{\frac{\mu_0}{\epsilon_0}}, \tag{C.5}$$

while the power coupled into the MDM waveguide at $z = 0$ is

$$\begin{aligned} P_{MDM} &= \int_{-\infty}^{\infty} \frac{1}{2} Re(\mathbf{E}\times\mathbf{H}^*)dx \\ &= \frac{1}{2} Re(E^-_{MDM}\times H^{-*}_{MDM}) \int_{-\infty}^{\infty} \phi(x)\phi(x)^* dx. \end{aligned} \tag{C.6}$$

Substituting equation (C.4) into the above equation leads to

$$P_{MDM} = \frac{1}{2} Re(\frac{\gamma_1}{j\omega\epsilon_0})|H^-_{MDM}|^2 \int_{-\infty}^{\infty} |\phi(x)|^2 dx. \tag{C.7}$$

Therefore, the transmission cross section σ_{T1} of a semi-finite MDM waveguide, defined as the total light power coupled into the right propagating fundamental TM mode of the waveguide, normalized by the incident plane wave power flux density, is

$$\sigma_{T1} = \frac{P_{MDM}}{\left|\mathbf{S}_{PW}\right|} = \frac{Re(\frac{\gamma_1}{j\omega\epsilon_0})|H^-_{MDM}|^2 \int_{-\infty}^{\infty} |\phi(x)|^2 dx}{|H^+_{PW}|^2\sqrt{\frac{\mu_0}{\epsilon_0}}}. \tag{C.8}$$

Using equation (C.8), I obtain the transmission coefficient $A \equiv \frac{|H^-_{MDM}|}{|H^+_{PW}|}$ when a plane wave is normally incident on a semi-infinite MDM waveguide

$$A = \frac{|H^-_{MDM}|}{|H^+_{PW}|} = [\sigma_{T1} \frac{\sqrt{\frac{\mu_0}{\epsilon_0}}}{Re(\frac{\gamma_1}{j\omega\epsilon_0}) \int_{-\infty}^{\infty} |\phi(x)|^2 dx}]^{\frac{1}{2}}. \tag{C.9}$$

I now consider a plane wave which is normally incident on a single slit coupler as in Fig. C.2. Based on scattering matrix theory, this system can be described by the following three equations

$$H^-_L = AH^+_{PW} + r_2 H^+_L, \tag{C.10}$$

$$H_L^+ = S_1 H_L^-, \tag{C.11}$$

$$H_u^- = t_1^{'} H_{L'}^-, \tag{C.12}$$

where A is the transmission coefficient when a plane wave is normally incident on a semi-infinite MDM waveguide (Eq. (C.9)), $S_1 = r_1 \exp(-2\gamma_1 h)$, $H_{L'}^- = H_L \exp(-\gamma_1 h)$, and γ_1 is the complex wave vector of the fundamental propagating TM mode in a silver-air-silver MDM waveguide. The reflection coefficients r_1, r_2 are defined in Fig. 6.3. Using equations (C.10) and (C.12), I obtain

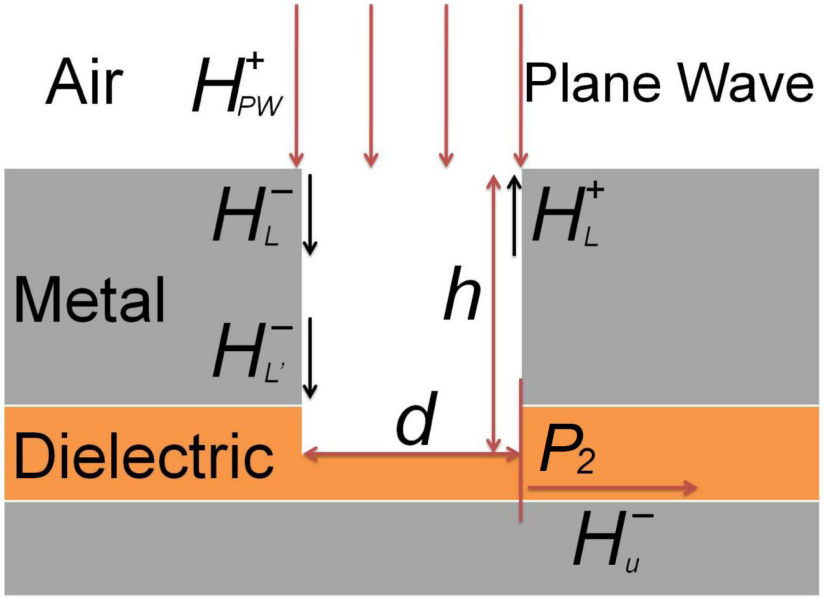

FIGURE C.2. Schematic showing a single slit for incoupling a normally incident plane wave from free space into the fundamental mode of a MDM plasmonic waveguide.

$$|\frac{H_u^-}{H_{PW}^+}| = |\frac{A t_1^{'} \exp(-\gamma_1 h)}{1 - r_1 r_2 \exp(-2\gamma_1 h)}|. \tag{C.13}$$

Using an approach similar to the one which was used to derive equation (C.8), I obtain the transmission cross section σ_T of the horizontal MDM waveguide

$$\sigma_T = \frac{Re(\frac{\gamma_2}{j\omega\epsilon})|H_u^-|^2 \int_{-\infty}^{\infty} |\phi_2(x)|^2 dx}{|H_{PW}^+|^2 \sqrt{\frac{\mu_0}{\epsilon_0}}}, \tag{C.14}$$

where γ_2 and $\phi_2(x)$ are the complex wave vector and field profile of the fundamental TM mode in the horizontal plasmonic waveguide, respectively. Substituting equation (C.13) into equation (C.14) leads to

$$\sigma_T = |\frac{At_1' \exp(-\gamma_1 h)}{1 - r_1 r_2 \exp(-2\gamma_1 h)}|^2 \frac{Re(\frac{\gamma_2}{j\omega\epsilon}) \int_{-\infty}^{\infty} |\phi_2(x)|^2 dx}{\sqrt{\frac{\mu_0}{\epsilon_0}}}. \tag{C.15}$$

Substituting equation (C.9) into (C.15), I obtain

$$\sigma_T = \sigma_{T1} \frac{Re(\frac{\gamma_2}{j\omega\epsilon}) \int_{-\infty}^{\infty} |\phi_2(x)|^2 dx}{Re(\frac{\gamma_1}{j\omega\epsilon_0}) \int_{-\infty}^{\infty} |\phi_1(x)|^2 dx} |\frac{t_1' \exp(-\gamma_1 h)}{1 - r_1 r_2 \exp(-2\gamma_1 h)}|^2. \tag{C.16}$$

Since $|t_1'| = |\frac{H_u^-}{H_{L'}^+}|$, I obtain

$$\sigma_T = \sigma_{T1} \frac{Re(\frac{\gamma_2}{j\omega\epsilon})|H_u^-|^2 \int_{-\infty}^{\infty} |\phi_2(x)|^2 dx}{Re(\frac{\gamma_1}{j\omega\epsilon_0})|H_{L'}^-|^2 \int_{-\infty}^{\infty} |\phi(x)|^2 dx} |\frac{\exp(-\gamma_1 h)}{1 - r_1 r_2 \exp(-2\gamma_1 h)}|^2. \tag{C.17}$$

Using equation (C.7), I obtain

$$\sigma_T = \sigma_{T1} \frac{P_2}{P_1} |\frac{\exp(-\gamma_1 h)}{1 - r_1 r_2 \exp(-2\gamma_1 h)}|^2, \tag{C.18}$$

where P_1 and P_2 are power fluxes defined in figures C.1 and C.2. Finally, using the fact that $T_{\text{splitter}} = \frac{P_2}{P_1}$ and defining $\eta_{\text{res1}} = |\frac{\exp(-\gamma_1 h)}{1 - r_1 r_2 \exp(-2\gamma_1 h)}|^2$, I obtain

$$\sigma_T = \sigma_{T1} \eta_{\text{res1}} T_{\text{splitter}}. \tag{C.19}$$

Appendix D: Proof of Eq.(6.2)

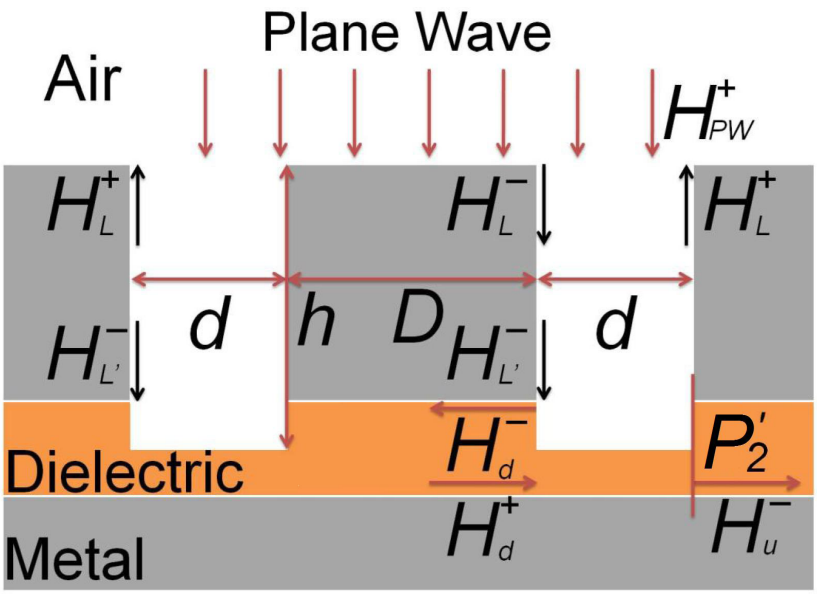

FIGURE D.1. Schematic showing a double-slit structure for incoupling a normally incident plane wave from free space into the fundamental mode of a MDM plasmonic waveguide.

I consider a plane wave which is normally incident on a symmetric double slit coupler as in Fig. D.1. Such a system can be described by the following equations

$$H_L^- = AH_{PW}^+ + r_4 H_L^+ + t_4 H_L^+, \tag{D.1}$$

$$H_L^+ = r_1 e^{-2\gamma_1 h} H_L^- + t_2 e^{-\gamma_1 h} H_d^+, \tag{D.2}$$

$$H_d^- = t_1 H_{L'}^- + r_3 H_d^+, \tag{D.3}$$

$$H_d^+ = t_1 e^{-\gamma_2 D} H_{L'}^- + r_3 e^{-2\gamma_2 D} H_d^-, \tag{D.4}$$

$$H_u^- = t_3 H_d^+ + t_1 H_{L'}^-. \tag{D.5}$$

Eliminating H_d^- from equations (D.3) and (D.4), I obtain

$$H_d^+ = \frac{t_1 e^{-\gamma_2 D}(1 + r_3 e^{-\gamma_2 D})}{1 - r_3^2 e^{-2\gamma_2 D}} H_{L'}^-. \tag{D.6}$$

Substituting this equation into equations (D.2) and (D.5), I get

$$H_L^+ = r_1 e^{-2\gamma_1 h} H_L^- + t_1 t_2 \frac{e^{-\gamma_1 h} e^{-\gamma_2 D}(1 + r_3 e^{-\gamma_2 D})}{1 - r_3^2 e^{-2\gamma_2 D}} H_{L'}^-, \tag{D.7}$$

$$H_u^- = t_1 [1 + t_3 \frac{e^{-\gamma_2 D}(1 + r_3 e^{-\gamma_2 D})}{1 - r_3^2 e^{-2\gamma_2 D}}] H_{L'}^-. \tag{D.8}$$

Substituting equation (D.7) into (D.1), I obtain

$$H_L^- = (r_4 + t_4)[r_1 e^{-2\gamma_1 h} H_L^- + t_1 t_2 \frac{e^{-\gamma_1 h - \gamma_2 D}(1 + r_3 e^{-\gamma_2 D})}{1 - r_3^2 e^{-2\gamma_2 D}} H_{L'}^-] + A H_{PW}^+. \tag{D.9}$$

Substituting $H_{L'}^- = H_L^- e^{-\gamma_1 h}$ in equations (D.8) and (D.9) results in

$$H_u^- = t_1 e^{-\gamma_1 h} [1 + t_3 \frac{e^{-\gamma_2 D}(1 + r_3 e^{-\gamma_2 D})}{1 - r_3^2 e^{-2\gamma_2 D}}] H_L^-, \tag{D.10}$$

$$H_L^- = (r_4 + t_4)[r_1 e^{-2\gamma_1 h} H_L^- + t_1 t_2 \frac{e^{-2\gamma_1 h - \gamma_2 D}(1 + r_3 e^{-\gamma_2 D})}{1 - r_3^2 e^{-2\gamma D}} H_L^-] + A H_{PW}^+. \tag{D.11}$$

Solving for H_L^-, I obtain

$$H_L^- = \frac{A H_{PW}^+}{1 - (r_4 + t_4)[r_1 e^{-2\gamma_1 h} + t_1 t_2 \frac{e^{-2\gamma_1 h - \gamma_2 D}(1 + r_3 e^{-\gamma_2 D})}{1 - r_3^2 e^{-2\gamma_2 D}}]}. \tag{D.12}$$

Using equations (D.10) and (D.12), I obtain

$$\frac{H_u^-}{H_{PW}^+} = \frac{A t_1 e^{-\gamma_1 h} [1 + t_3 \frac{e^{-\gamma_2 D}(1 + r_3 e^{-\gamma_2 D})}{1 - r_3^2 e^{-2\gamma_2 D}}]}{1 - (r_4 + t_4)[r_1 e^{-2\gamma_1 h} + t_1 t_2 \frac{e^{-2\gamma_1 h - \gamma_2 D}(1 + r_3 e^{-\gamma_2 D})}{1 - r_3^2 e^{-2\gamma_2 D}}]}. \tag{D.13}$$

Using equation (D.13) and an approach similar to the one which was used to obtain equation (C.19) from (C.14), I obtain

$$\sigma_T = \sigma_{T2} \eta_{\text{res2}} T_{\text{splitter}}, \tag{D.14}$$

where $\eta_{\text{res2}} = |\frac{\frac{e^{-\gamma_1 h}[1+t_3\frac{e^{-\gamma_2 D}(1+r_3 e^{-\gamma_2 D})}{1-r_3^2 e^{-2\gamma_2 D}}]}{1-(r_4+t_4)[r_1 e^{-2\gamma_1 h}+t_1 t_2\frac{e^{-2\gamma_1 h-\gamma_2 D}(1+r_3 e^{-\gamma_2 D})}{1-r_3^2 e^{-2\gamma_2 D}}]}|^2$, $T_{\text{splitter}} = \frac{P_2'}{P_1'}$, and P_1', P_2' are power fluxes defined in Figs. D.1 and D.2.

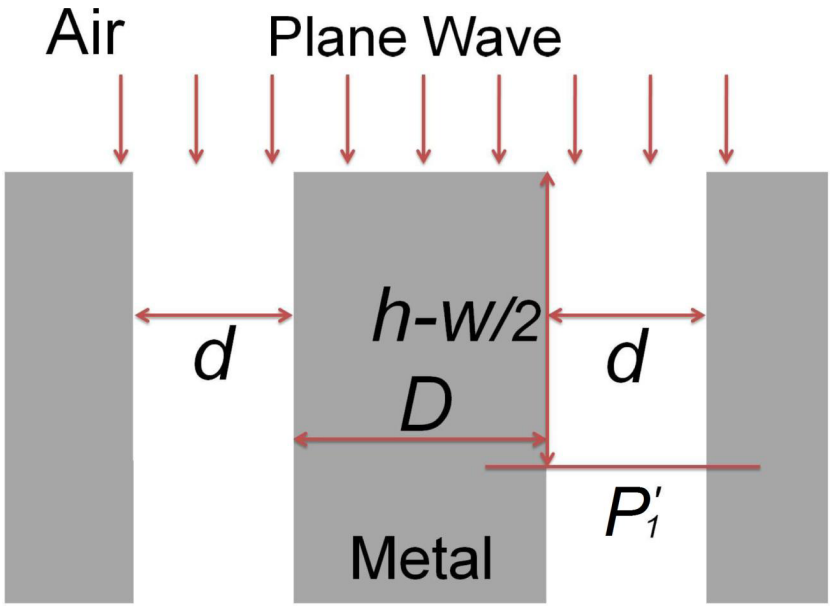

FIGURE D.2. Schematic showing a plane wave which is normally incident from free space on two semi-finite MDM plasmonic waveguides.

Finally, we discuss how to calculate t_1, t_2. In order to extract $t_1 t_2$, I focus on a symmetric junction between the silver-silica-silver waveguide and the silver-air-silver waveguide as in Fig. D.3. Based on the scattering matrix theory, I can write

$$\begin{bmatrix} H_1^- \\ H_2^- \\ H_3^- \end{bmatrix} = \begin{bmatrix} r_1 & t_2 & t_2 \\ t_1 & r_3 & t_1 \\ t_1 & t_3 & r_3 \end{bmatrix} \begin{bmatrix} H_1^+ \\ H_2^+ \\ H_3^+ \end{bmatrix}, \tag{D.15}$$

where r_1, r_3, t_1, and t_2 are defined in Fig. 6.11. Since the two MDM waveguides have different field profiles, to extract $t_1 t_2$ I terminate the simulation domain at the plane of both output ports with perfect electric conductor boundary conditions (Fig. D.3). Such terminations result in zero tangential electric fields, and therefore, give +1 for the reflection coefficient of the transverse magnetic field H_y. Thus, I get $H_2^+ = H_2^- e^{-2\gamma_2 L}$ and $H_3^+ = H_3^- e^{-2\gamma_2 L}$.

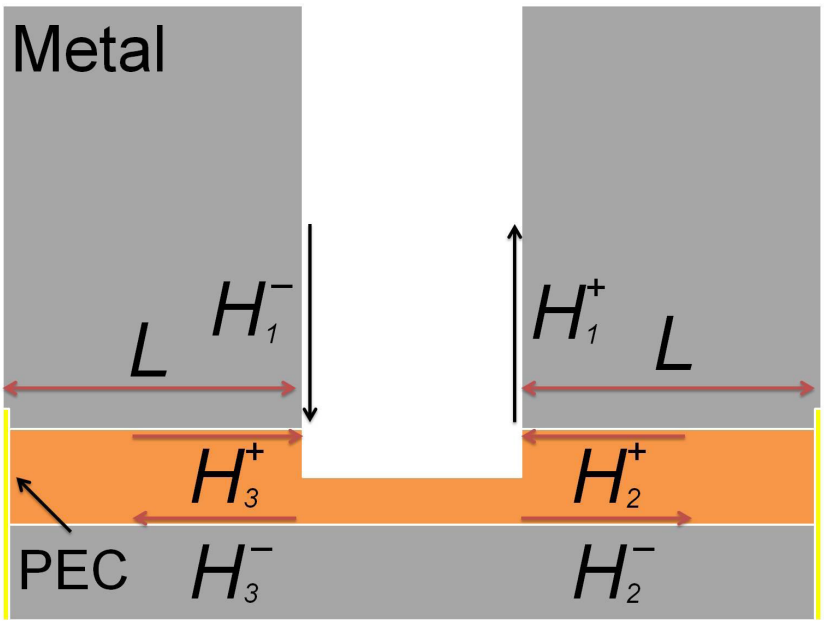

FIGURE D.3. Schematic related to the calculation of t_1 and t_2.

Substituting these equations in (D.15) gives

$$\begin{bmatrix} H_1^- \\ H_2^- \\ H_3^- \end{bmatrix} = \begin{bmatrix} r_1 & t_2 & t_2 \\ t_1 & r_3 & t_1 \\ t_1 & t_3 & r_3 \end{bmatrix} \begin{bmatrix} H_1^+ \\ H_2^- e^{-2\gamma_2 L} \\ H_3^- e^{-2\gamma_2 L} \end{bmatrix}. \tag{D.16}$$

Expanding the matrix one gets

$$H_1^- = r_1 H_1^+ + t_2(H_2^- + H_3^-)e^{-2\gamma_2 L}, \tag{D.17}$$

$$H_2^- = t_1 H_1^+ + r_3 H_2^- e^{-2\gamma_2 L} + t_3 H_3^- e^{-2\gamma_2 L}, \tag{D.18}$$

$$H_3^- = t_1 H_1^+ + t_3 H_2^- e^{-2\gamma_2 L} + r_3 H_3^- e^{-2\gamma_2 L}. \tag{D.19}$$

Using equation (D.16), I obtain

$$R \equiv \frac{H_1^-}{H_1^+} = r_1 + t_2\left(\frac{H_2^-}{H_1^+} + \frac{H_3^-}{H_1^+}\right)e^{-2\gamma_2 L}. \tag{D.20}$$

Note that H_2^-=H_3^- due to symmetry. Using equations (D.18) and (D.19), I obtain

$$\frac{H_2^-}{H_1^+} = \frac{H_3^-}{H_1^+} = \frac{t_1 + \frac{t_1 t_3 e^{-2\gamma_2 L}}{1 - r_3 e^{-2\gamma_2 L}}}{1 - r_3 e^{-2\gamma_2 L} - \frac{t_3^2 e^{-4\gamma_2 L}}{1 - r_3 e^{-2\gamma_2 L}}}. \tag{D.21}$$

Substituting equation (D.21) into equation (D.20), I obtain

$$R = \frac{H_1^-}{H_1^+} = r_1 + 2t_1t_2[\frac{1 - r_3e^{-2\gamma_2 L} + t_3e^{-2\gamma_2 L}}{(1 - r_3e^{-2\gamma_2 L})^2 - t_3^2 r_3 e^{-4\gamma_2 L}}]e^{-2\gamma_2 L}. \tag{D.22}$$

Solving equation (D.22) for t_1t_2 finally gives

$$t_1t_2 = \frac{R - r_1}{2[\frac{1-r_3e^{-2\gamma_2 L}+t_3e^{-2\gamma_2 L}}{(1-r_3e^{-2\gamma_2 L})^2-t_3^2 r_3 e^{-4\gamma_2 L}}]e^{-2\gamma_2 L}}. \tag{D.23}$$

Appendix E: Letter of Permission

AMERICAN INSTITUTE OF PHYSICS LICENSE

TERMS AND CONDITIONS

All payments must be made in full to CCC. For payment instructions, please see information listed at the bottom of this form.

License Number	3020870367165
Order Date	Nov 02, 2012
Publisher	American Institute of Physics
Publication	Applied Physics Letters
Article Title	Subwavelength slow-light waveguides based on a plasmonic analogue of electromagnetically induced transparency
Author	Yin Huang, Changjun Min, Georgios Veronis
Online Publication Date	Oct 7, 2011
Volume number	99
Issue number	14
Type of Use	Thesis/Dissertation
Requestor type	Author (original article)
Format	Electronic
Portion	Excerpt (> 800 words)
Will you be translating?	No
Title of your dissertation	Plasmonic Devices for Manipulating Light at the Nanoscale: Slow-light Waveguides

	and Compact Couplers
Expected completion date	Nov 2012
Estimated size (number of pages)	136
Total	0.00 USD

Terms and Conditions

American Institute of Physics – Terms and Conditions: Permissions Uses

American Institute of Physics ("AIP") hereby grants to you the non-exclusive right and license to use and/or distribute the Material according to the use specified in your order, on a one-time basis, for the specified term, with a maximum distribution equal to the number that you have ordered. Any links or other content accompanying the Material are not the subject of this license.

1. You agree to include the following copyright and permission notice with the reproduction of the Material: "Reprinted with permission from [FULL CITATION]. Copyright [PUBLICATION YEAR], American Institute of Physics." For an article, the copyright and permission notice must be printed on the first page of the article or book chapter. For photographs, covers, or tables, the copyright and permission notice may appear with the Material, in a footnote, or in the reference list.

2. If you have licensed reuse of a figure, photograph, cover, or table, it is your responsibility to ensure that the material is original to AIP and does not contain the copyright of another entity, and that the copyright notice of the figure, photograph, cover, or table does not indicate that it was reprinted by AIP, with permission, from another source. Under no circumstances does AIP, purport or intend to grant permission to reuse material to which it does not hold copyright.

3. You may not alter or modify the Material in any manner. You may translate the Material into another language only if you have licensed translation rights.

You may not use the Material for promotional purposes. AIP reserves all rights not specifically granted herein.

4. The foregoing license shall not take effect unless and until AIP or its agent, Copyright Clearance Center, receives the Payment in accordance with Copyright Clearance Center Billing and Payment Terms and Conditions, which are incorporated herein by reference.

5. AIP or the Copyright Clearance Center may, within two business days of granting this license, revoke the license for any reason whatsoever, with a full refund payable to you. Should you violate the terms of this license at any time, AIP, American Institute of Physics, or Copyright Clearance Center may revoke the license with no refund to you. Notice of such revocation will be made using the contact information provided by you. Failure to receive such notice will not nullify the revocation.

6. AIP makes no representations or warranties with respect to the Material. You agree to indemnify and hold harmless AIP, American Institute of Physics, and their officers, directors, employees or agents from and against any and all claims arising out of your use of the Material other than as specifically authorized herein.

7. The permission granted herein is personal to you and is not transferable or assignable without the prior written permission of AIP. This license may not be amended except in a writing signed by the party to be charged.

8. If purchase orders, acknowledgments or check endorsements are issued on any forms containing terms and conditions which are inconsistent with these provisions, such inconsistent terms and conditions shall be of no force and effect. This document, including the CCC Billing and Payment Terms and Conditions, shall be the entire agreement between the parties relating to the subject matter hereof.

This Agreement shall be governed by and construed in accordance with the laws of the State of New York. Both parties hereby submit to the jurisdiction of the courts of New York County for purposes of resolving any disputes that may arise hereunder.

If you would like to pay for this license now, please remit this license along with your payment made payable to "COPYRIGHT CLEARANCE CENTER" otherwise you will be invoiced within 48 hours of the license date. Payment should be in the form of a check or money order referencing your account number and this invoice number RLNK500889503.

Once you receive your invoice for this order, you may pay your invoice by credit card. Please follow instructions provided at that time.

Make Payment To:

Copyright Clearance Center

Dept 001

P.O. Box 843006

Boston, MA 02284-3006

For suggestions or comments regarding this order, contact RightsLink Customer Support: customercare@copyright.com or +1-877-622-5543 (toll free in the US) or +1-978-646-2777.

Gratis licenses (referencing 0.00 USD in the Total field) are free. Please retain this printable license for your reference. No payment is required.

Vita

Yin Huang was born in October 1984, in Changsha, Hunan, China. He finished his undergraduate studies at North China University of Technology in July 2007. He earned a Master of Science degree in physics from Beijing Jiaotong University in July 2009. In August 2009 he came to Louisiana State University to pursue graduate studies in electrical engineering. He is currently a candidate for the degree of Doctor of Philosophy in electrical engineering, which will be awarded in December 2012.